MOVPE of Semipolar r-plane AlGaN-based Semiconductors toward Highly Efficient Solid-state UVC Emitters

Ryota AKAIKE

2023

MOVPE of Semipolar r-plane AlGaN-based Semiconductors toward Highly Efficient Solid-state UVC Emitters

Ryota AKAIKE

Electronic Science and Engineering
Kyoto University

2023

Abstract

Ultraviolet C (UVC) lights are UV lights of which wavelength is 100 nm–280 nm. One kind of UVC lights can be used for sterilization. For example, the UVC light of ∼265 nm has been known to inactivate bacteria and viruses because it can be strongly absorbed by DNA. Recently, the 222-nm far-UVC light has been found to be a germicidal radiation without harming human skins or eyes. Hg lamps, excimer lamps and excimer lasers have long been used as UVC emitters, although they have some disadvantages such as their largeness and harmful constituents. AlGaN-based UV emitters are promising because of their harmless constituents, tunability of emission wavelength, and compactness. However, their external quantum efficiencies (EQEs) are still low. One of the reasons for the low EQEs is low internal quantum efficiencies (IQEs), which are the efficiencies in quantum wells (QWs).

The IQEs are determined by two recombination processes, radiative recombination process and non-radiative recombination process. When we focus on radiative recombination process, the use of semipolar planes instead of conventional *c*-plane is one of the solutions to resolve low IQEs. AlGaN has spontaneous polarization along *c*-axis and this value differs in AlN molar fraction. In addition, there is also piezoelectric polarization in QWs when QWs are not completely relaxed. As a result, electric fields are induced in conventional *c*-plane QWs roughly by the difference in sum of above-mentioned two polarizations of QWs and barriers. Electric fields in QWs separate electrons and holes because they have the opposite sign of electric charge and their overlap of wave functions becomes low. By contrast, when we incline the growth plane from *c*-plane to nonpolar planes, spontaneous polarization along the growth direction becomes lower, and piezoelectric polarization is reversed at a certain angle and approaches zero. Consequently, internal electric fields in QWs of semipolar planes are lower than that of *c*-plane and therefore the use of semipolar planes is expected to enhance radiative recombination process.

Fabrication of epitaxial AlN films with high quality on foreign substrates, such as sapphire substrates, is difficult. The use of AlN substrates will over-

come this issue. Our group has succeeded in fabricating semipolar AlN films and AlGaN/AlN QWs with smooth surfaces on semipolar AlN substrates. To fabricate LEDs, however, AlGaN films are currently necessary because of high resistivity of n-type AlN. In general, optimal growth conditions of AlN, GaN, and AlGaN are different. Quest for good growth condition of AlGaN is needed.

In this study, we concentrate on the establishment of growth conditions of semipolar r-plane AlGaN films with smooth surfaces. We also investigate optical characteristics of semipolar r-plane AlGaN-based QWs. Finally, we demonstrate semipolar r-plane UVC LEDs for the first time in the world.

In Chapter 2, advantages of r-plane LEDs over c-plane LEDs are theoretically investigated in terms of IQEs, LEEs, and CIEs. IQEs are determined by the balance between radiative recombination and non-radiative recombination. Therefore, overlap of electrons and holes, and critical thickness are calculated. In both cases, superiority of semipolar r-plane to c-plane is confirmed. In terms of LEE, r-QWs are found to show superiority to c-QWs especially in the far-UVC region by the calculation of optical transition matrix elements. CIEs of LEDs on various planes are calculated by a commercial device simulator. The CIE decreased as a growth plane was inclined from c-plane, but r-plane (43° from c-plane) LEDs have enough high CIEs. However, when a growth plane was inclined to $(11\bar{2}2)$ plane (58° from c-plane), CIEs drastically decreased. The reason for the drastic decrease in CIEs are found to be a reduction of electric polarization. Considering the balance of IQE, LEE, and CIE, r-plane is the most favorable plane for UVC LEDs.

In Chapter 3, growth conditions of semipolar r-plane AlGaN films with low pit density by metalorganic vapor phase epitaxy (MOVPE) method are established. Then, the mechanism of change in pit density is discussed. Pit density is determined by the balance between pit formation and pit elimination. Low NH_3 flow rate, high growth temperature, and low AlN molar fraction conditions are favorable in terms of pit formation. However, in terms of pit elimination, shorter migration length of adatoms is favorable, i.e. high NH_3 flow rate, high pressure, low growth temperature, and high AlN molar fraction. As a result, optimal growth conditions exist. Relaxation degrees of the fabricated r-AlGaN films are also investigated. r-AlGaN films are easily relaxed along the $[1\bar{1}01]$ direction, which is expected in the theoretical calculation of relaxation process. However, they are hardly relaxed along the $[11\bar{2}0]$ direction compared with the $[1\bar{1}01]$ direction. This might be related to nearly no relaxation observed on c-AlGaN films. Dislocations originating from the stress relaxation are confined in the vicinity of the interface between AlGaN and AlN. Therefore, the effect by misfit dislocations on QWs fabricated on r-plane AlGaN films is small.

In Chapter 4, optical characteristics of fabricated *c*- and *r*-QWs are investigated by photoluminescence (PL) measurement. *r*-QWs showed much higher PL intensity than *c*-QWs especially in the far-UVC region. In fact, the IQE and LEE of *r*-QW emitting at ∼225 nm were 3.4 and 3–4 times higher than those of *c*-QW. Then, time resolved PL (TRPL) measurement is performed at RT. The analyses of TRPL decay curves reveal that the reason for the higher IQE of the *r*-QW is shorter radiative lifetime of the *r*-QW and possibly reduced non-radiative recombination centers in the *r*-QW. AlGaN/AlGaN QWs are also fabricated. AlN molar fraction of AlGaN on *r*-plane is found to be smaller than that on *c*-plane because the wavelength of *r*-QW was longer than *c*-QW grown side by side and because no difference in thicknesses between *c*- and *r*-QWs was observed.

In Chapter 5, *r*-plane UVC LEDs are demonstrated. Firstly, doping conditions are investigated based on *r*-AlGaN growth conditions established in Chap. 3. Then, *r*-plane LEDs emitting at 270 nm in the UVC region are successfully demonstrated.

In Chapter 6, the obtained results are summarized and some future works are discussed.

Acknowledgements

I would like to thank many people for supporting me in various aspects during my research life in Kawakami laboratory at Kyoto University. Here, I express my gratitude.

First of all, I would like to express my most sincere gratitude to Professor Yoichi Kawakami of Electronic Science and Engineering, Kyoto University for his continuous supervision, invaluable advice, and suggestions. He not only provided me with the opportunity to conduct this research, but also gave me moral support throughout my research life. I would like to thank Professor Susumu Noda. He was my advisor teacher during my undergraduate life and showed me how interesting researches on light are. I would like to thank Professor Tsunenobu Kimoto for the useful discussions. His careful attention to me makes me feel relaxed during the International Seminar Dojo. Suggestions and advice from different research fields by Professor Susumu Noda and Professor Tsunenobu Kimoto made this Ph.D. thesis better. I would like to express my deep gratitude to Associate Professor Mitsuru Funato. When I got stuck in my research, he always gave me helpful suggestions, which illuminated the way. In addition, he corrected a lot of presentation data and writings. I would like to express my gratitude to Assistant Professor Ryota Ishii. He taught me how to use optical equipment and gave me a lot of knowledge.

I would like to express my gratitude to Dr. Takuya Ozaki currently at Nichia Corporation for the supervision during my B4 and M1 life. He corrected my writings, powerpoint materials, and bachelor thesis. I also would like to express my gratitude to Dr. Shuhei Ichikawa currently at Osaka University. He was not my direct supervisor, but gave me useful discussions as a member of the same DUV group in Kawakami laboratory. Both of them also made me feel relaxed by inviting me for lunch and dinner. I would like to express my gratitude to Dr. Ken Kataoka currently at Ushio Inc. He introduced the MOVPE equipment used in this study and taught me how to use it. When I asked him some questions by e-mail, he willingly answered them in detail. I would like to express my gratitude to Project Assistant

Professor Yoshinobu Matsuda, and Dr. Katsuhiro Kishimoto currently at Nichia Corporation for their helpful discussions.

I would like to express my gratitude to JFE Mineral Company Ltd. for providing us semipolar r-plane AlN substrates. Thanks to a lot of invaluable r-AlN substrates, we have been able to investigate many growth conditions.

I would like to sincerely thank all the other members including the secretaries and graduates in Kawakami laboratory for their kindness, fruitful discussions, and supports; Ms. Miki Watanabe, Ms. Keiko Furuyama, Ms. Tamaki Suwa, Ms. Hiromi Nishimura, Ms. Mina Irikawa, Dr. Wu Pei-tsen, Ms. Meng Qingfang, Mr. Ryosuke Ishido, Mr. Kyosuke Kumamoto, Mr. Masahiro Tsukamoto, Mr Yoshihisa Nakashima, Mr. Takahiro Ohara, Mr. Ryohei Kido, Mr. Takeya Matsumura, Mr. Atsushi Nishikubo, Mr. Koji Uemoto, Mr. Yuki Nagase, Mr. Minehiro Hayakawa, Ms. Yoko Kawaguchi, Mr. Yuji Koyama, Mr. Hirotsugu Kobayashi, Mr. Tatsuya Tachibanaki, Mr. Masahiro Nakakami, Mr. Kazuto Yamazaki Mr. Takahiro Shigeoka, Mr. Kenta Tsubouchi, Mr. Keita Maehara, Mr. Yuki Kono, Mr. Yoshitaka Goto, Mr. Masaya Shigematsu, Mr. Atsuhiro Sugimoto, Mr. Masaki Morioka, Mr. Zhu Zhiwei, Dr. Anna Kafer, Mr. Yuya Ishizaki, Mr. Souta Funato, Mr. Ban Ronglyu, Mr. Naoki Gyoja, Mr. Kunio Matsumoto, Mr. Zhang Zhaozong, Mr. Ryunosuke Umemoto, Mr. Kimito Kamiya, Mr. Eiji Kikuchi, Mr. Shiki Tanaka, Mr. Takato Fukui, Mr. Taro Sakaguchi, Mr. Nagato Sumita, Mr. Haru Higashinakagawa, Mr. Haruyoshi Miyawaki, Mr. Atsuhisa Izumi, Mr Yuzuki Inoue, Mr. Kodai Takemura, Mr. Shogo Fukushige, and Mr. Tsukasa Watanabe. Mr. Zhang Zhaozong and Mr. Atsuhisa Izumi corrected many errors in this Ph.D. thesis.

This work was supported in part by the Japan Society for the Promotion of Science (JSPS) through the Grant-in-Aid for Research Fellow (21J15559) and WISE program, MEXT.

Finally, I sincerely wish to thank my parents, my sister, and all of my relatives for their understandings, supports, and encouragements.

February, 2023
Ryota AKAIKE

Contents

Chapter 1

Introduction

1.1 Ultraviolet C (UVC) Light

Our life is surrounded by many types of lights. In order to obtain information from the world through our eyes, we need visible lights such as sunlight, lights from incandescent lamps, fluorescent lamps, and light emitting diodes (LEDs). Not only visible lights but also infrared or ultraviolet (UV) lights are indispensable for our modern life. For example, infrared lights are used for optical communications, and UV lights are used for photolithography. They support the modern information society. The interest of this thesis is UV lights.

UV lights are classified by their spectral ranges in many ways. One classification is UVA (315 nm–400 nm), UVB (280 nm–315 nm), and UVC (100 nm–280 nm) according to ISO [2][1]. The term of deep UV (DUV), which is originally used by Dr. Lin of IBM [3], is also used to refer to the UV light whose range is typically 200 nm–300 nm.

DUV lights have many applications such as sterilization, air and water purification, and medical research [4]. In particular, the UVC light of ∼265 nm has been known for its effectiveness to sterilization because it can be strongly absorbed by DNA [1]. Figure 1.1 shows UV absorption spectra by DNA, some kinds of protozoa and viruses [1]. They are in good agreement with each other around ∼265 nm, which means that absorption of UVC light by DNA leads to sterilization. Therefore, applications for water and air purification are expected. According to United Nations Children's Fund (UNICEF), 2 billion people cannot have access to safe drinking water [5]. The 6th goal of the Sustainable Development Goals (SDGs) is "Ensure availability

[1]Many different spectral ranges are often used for the UVA, UVB, and UVC classification.

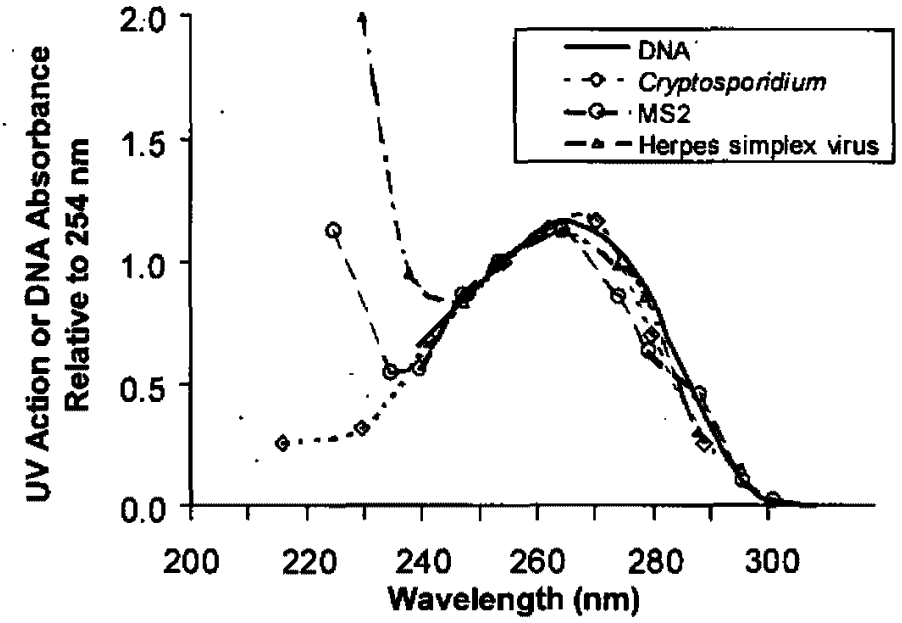

Figure 1.1: Absorption spectra of UV light by DNA and some kinds of protozoa and viruses [1].

and sustainable management of water and sanitation for all" [6], which should be achieved by 2030 and was adopted by the United Nations (UN) in 2015. The demand for water purification is obviously increasing. In addition, there is more and more demand for air purification since coronavirus disease 2019 (COVID-19) pandemic occurred.

Recently, the 222-nm far-UVC light has been found to be a germicidal radiation [7–11] without harming human skins or eyes [12–15] while the 265 nm UVC light is harmful to human bodies in principle. It is considered that the mechanism of safety is the absorption by proteins in the cytoplasm [12, 15], and the safeness of the 222-nm far-UVC light is confirmed for at least rabbits which are even not covered by stratum corneum [15]. Krypton chloride (KrCl) excimer lamps are currently used as 222-nm far-UVC sources. However, the lifetime of the lamps is about 3000 hours and the overall power efficiency of the equipment is 0.53 % [16][2]. Higher efficiencies of far-UVC devices are desired for more widespread use around the world. The COVID-19 pandemic is still ongoing, and spread of UVC and far-UVC devices is

[2]We calculated the whole power efficiency from the data of i-BT type devices [16] (center illuminance: 0.014 mW/cm^2, illumination area: 0.57 m^2, power consumption: 15 W). Note that the calculated efficiency includes the efficiencies of devices other than the lamps.

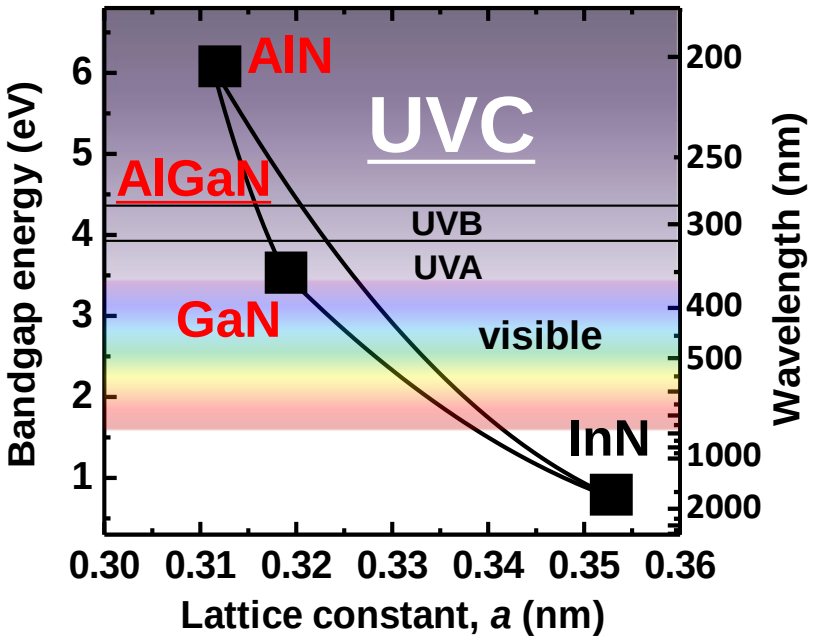

Figure 1.2: Bandgap energies of group III nitrides as functions of the a lattice constant.

expected to be a solution to end this pandemic.

1.2 AlGaN-based UVC LEDs

Hg lamps, excimer lamps, and excimer lasers have long been used as UVC emitters. However, they have some disadvantages such as their largeness and harmful constituents. III-nitride-semiconductor-based UV emitters are promising because of their harmless constituents, tunability of emission wavelength, and compactness. Since the successful fabrication of high-quality epitaxial gallium nitride (GaN) layers [17, 18] and the establishment of p-type conduction [19, 20], III-nitride semiconductors have been widely used. Aluminum nitride (AlN) has larger bandgap (6.10 eV at 0 K [21]) than GaN (3.51 eV at 0 K [21]), and the bandgap can be tuned by fabricating their alloy, aluminum gallium nitride (AlGaN) with various AlN molar fractions, as shown in Fig. 1.2. As a result, UV LEDs with various wavelengths can be fabricated.

Next, we focus on efficiencies. The external quantum efficiencies (EQEs), which is the ratio of photon number extracted from LEDs to the injected

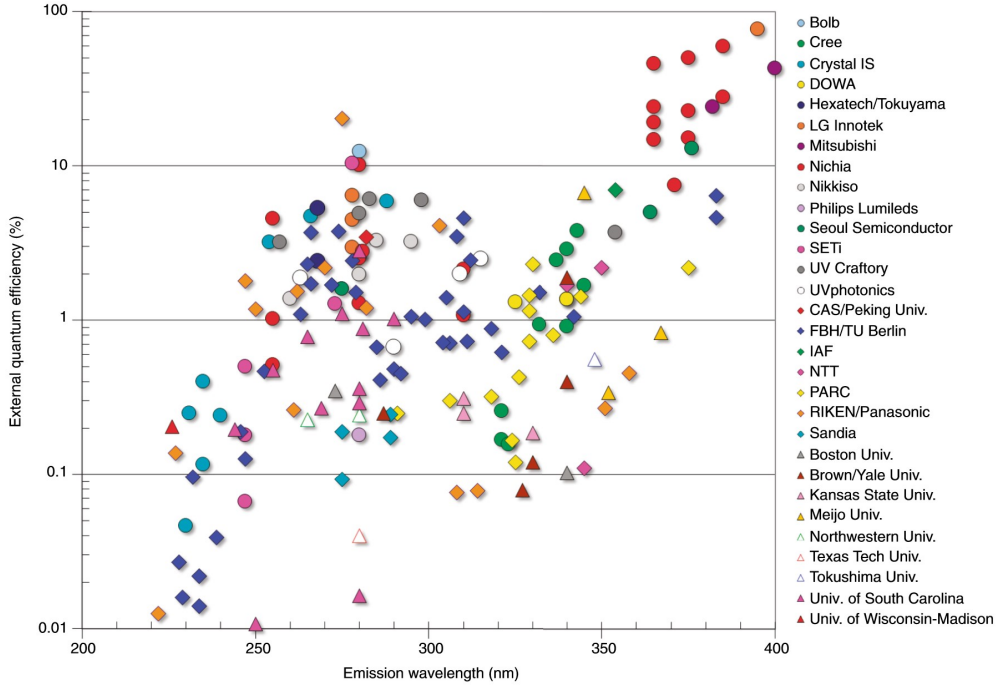

Figure 1.3: Reported EQEs of AlGaN-based UV LEDs [22].

carrier number, are described as the product of three factors,

$$\eta_{\mathrm{EQE}} = \eta_{\mathrm{IQE}} \times \eta_{\mathrm{CIE}} \times \eta_{\mathrm{LEE}}. \tag{1.1}$$

η_{IQE} is the internal quantum efficiency, which is the ratio of the number of radiatively recombined carriers to that of recombined all carriers in quantum wells (QWs). η_{CIE} is the current injection efficiency, which is the ratio of consumed current in QWs to applied current. η_{LEE} is the light extracted efficiency, which is the ratio of extracted photon number outside LEDs to generated photon number in QWs. For high EQEs, all of these three factors have to be high.

Figure 1.3 shows EQEs of AlGaN-based UV LEDs [22]. The reported maximum EQE in the UVC region is 20.3 % (wavelength: 275 nm) [23] [3], which is low compared with blue LEDs ($>$ 80 % [25]). At shorter wavelengths the EQEs become much lower and especially lower than 1 % at wavelengths shorter than 230 nm (in the far-UVC region). One of the reasons for this low

[3]The reported maximum wall plug efficiency (WPE), which is the ratio of extracted light power to applied electric power, of AlGaN-based UVC LEDs is 15.7 % (wavelength: 275 nm) [24].

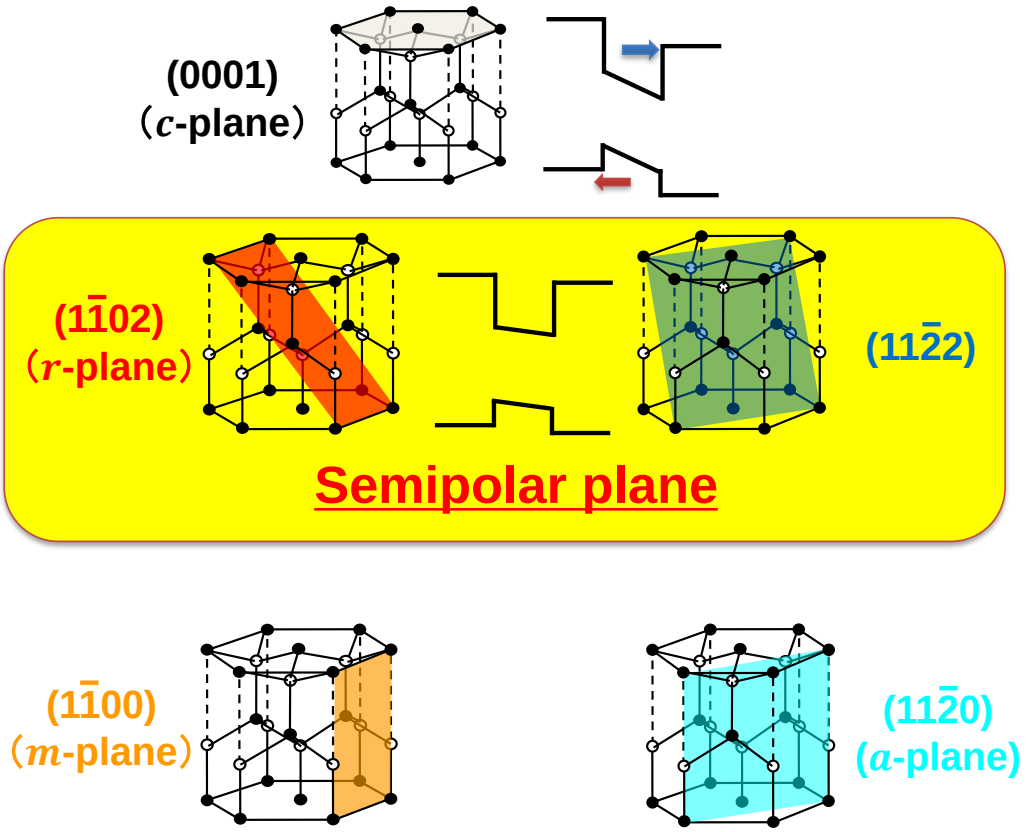

Figure 1.4: Examples of semipolar planes.

EQEs is considered to be low IQEs. In fact, the IQEs of c-AlGaN/AlN QWs become lower as the emission wavelength becomes shorter [26, 27].

1.3 Semipolar Plane

The IQEs are determined by two recombination processes and described as[4]

$$\eta_{\mathrm{IQE}} = \frac{\tau_{\mathrm{rad}}^{-1}}{\tau_{\mathrm{rad}}^{-1} + \tau_{\mathrm{nonrad}}^{-1}}, \tag{1.2}$$

where τ_{rad}^{-1} is a radiative recombination rate and $\tau_{\mathrm{nonrad}}^{-1}$ is a non-radiative recombination rate. (τ_{rad} is a radiative recombination lifetime and τ_{nonrad} is a non-radiative recombination lifetime.) There are two routes to achieve

[4]Monomolecular recombination process and temporally and spatially constant recombination rate are assumed.

high IQEs; one is enhancement of τ_{rad}^{-1}, and the other is suppression of $\tau_{\mathrm{nonrad}}^{-1}$. When we focus on τ_{rad}^{-1}, the use of semipolar planes (example: Fig. 1.4) is one of the solutions to resolve low IQEs. AlGaN has spontaneous polarization along the *c*-axis and this value differs by AlN molar fractions. In addition, there is also piezoelectric polarization in QWs when QWs are not completely relaxed. As a result, electric fields are induced in conventional *c*-plane QWs roughly by the difference in sum of above-mentioned two polarizations of QWs and barriers. Electric fields in QWs separates electrons and holes because they have the opposite sign of electric charge and the overlap of their wave functions becomes low. By contrast, when we incline the growth plane from *c*-plane to nonpolar planes, spontaneous polarization along the growth direction becomes lower, and piezoelectric polarization is reversed at a certain angle and approaches zero. Consequently, internal electric fields in QWs of semipolar planes are lower than that of *c*-plane and therefore the use of semipolar planes is expected to enhance τ_{rad}^{-1}.

1.4 Current Status of Semipolar AlGaN and UVC LEDs

There are some studies on semipolar Al(Ga)N, for example, *r*-AlN on *r*-ZnO substrates [28], $(11\bar{2}2)$ Al(Ga)N on *m*-sapphire substrates [29–54], and $(10\bar{1}3)$ Al(Ga)N on *m*-sapphire substrates [42–44, 49, 55]. Most studies show the difficulty of fabricating semipolar Al(Ga)N on foreign substrates. Typically, FWHMs of XRD rocking curves (XRC) are over 1000 arcsec at least along one direction [29–31, 34–39, 41, 48, 53, 54, 56, 57], basal-plane stacking fault (BSF) densities are higher than 10^5 cm^{-1} [30, 32, 34], and RMS of surface roughness is over 1 nm [29–31, 34–36, 38–41, 44, 46–50, 53, 54]. Some studies have recently reported that semipolar AlN films with XRC FWHMs less than 1000 arcsec were fabricated by *ex situ* high temperature ($\sim$1700 °C) thermal annealing of AlN films prepared by MOVPE ($(11\bar{2}2)$ planes) [43, 56, 57] or prepared by sputtering [50], and ammonia free high temperature MOVPE ($(10\bar{1}3)$ planes) [55]. However, they require an additional process or special equipment. In addition, the EQEs of recently fabricated semipolar UV LEDs on such high-quality templates are still low ($\leq$0.026 %) [52].

The use of AlN substrates will overcome these issues. Our group has succeeded in fabricating semipolar AlN films and AlGaN/AlN QWs with smooth surfaces on semipolar AlN substrates [58–60]. $Al_{0.69}Ga_{0.31}N/Al_{0.90}Ga_{0.10}N$ QWs with good structures on $(20\bar{2}1)$ AlN substrates were also reported by another group [61]. To fabricate LEDs, AlGaN films are currently neces-

sary because of high resistivity of n-type AlN [4, 62, 63]. In general, optimal growth conditions of AlN, GaN, and AlGaN are different. Quest for good growth condition of AlGaN is needed.

1.5 Thesis Outline

Considering the background described in the previous sections, the goal of this Ph.D. thesis was set to be the fabrication of highly efficient UVC LEDs using a semipolar plane. In Chapter 2, some advantages of semipolar planes are described from theoretical perspectives. Especially, the $(1\bar{1}02)$ r-plane will be found to be one of the most optimal planes taking into consideration all elements of EQEs, which are IQEs, LEEs, and CIEs. In Chapter 3, growth conditions of semipolar r-AlGaN films with smooth surfaces are established. In Chapter 4, r-plane QWs are evaluated with photoluminescence (PL) measurements. In Chapter 5, r-plane UVC LEDs are demonstrated. In Chapter 6, conclusions and future works are described.

Chapter 2

Advantages of Semipolar r-plane UVC LEDs

2.1 Introduction

In this chapter we show some advantages of the semipolar r-plane from a theoretical point of view. As shown in Eq.(1.1), EQEs are product of IQEs, LEEs, and CIEs. In Sec. 2.2, electric fields and overlap of electron and hole wavefunctions are calculated, which are related to radiative recombination (and IQEs). In Sec. 2.3, advantages of r-plane and calculation results of critical thickness are described, which are related to non-radiative recombination (and IQEs). In Sec. 2.4, optical polarization is described, which is related to LEEs. In Sec. 2.5, CIEs are calculated and superiority of r-plane will be described.

2.2 Electric Field in QWs and Overlap of Electrons and Holes

Formula for Calculation of Electric Field in QWs

In the previous report [59], electric fields in multi QWs (MQWs) on semipolar planes are calculated by the following formula,

$$E_{\mathrm{int}}^{\mathrm{well}} = \frac{P'_{z',\mathrm{bar}} - P'_{z',\mathrm{well}}}{\varepsilon'^{\mathrm{P}}_{z',\mathrm{well}} + \varepsilon'^{\mathrm{P}}_{z',\mathrm{bar}}(L_{\mathrm{w}}/L_{\mathrm{b}})}, \tag{2.1}$$

$$E_{\mathrm{int}}^{\mathrm{bar}} = -\frac{L_{\mathrm{w}}}{L_{\mathrm{b}}} E_{\mathrm{int}}^{\mathrm{well}}, \tag{2.2}$$

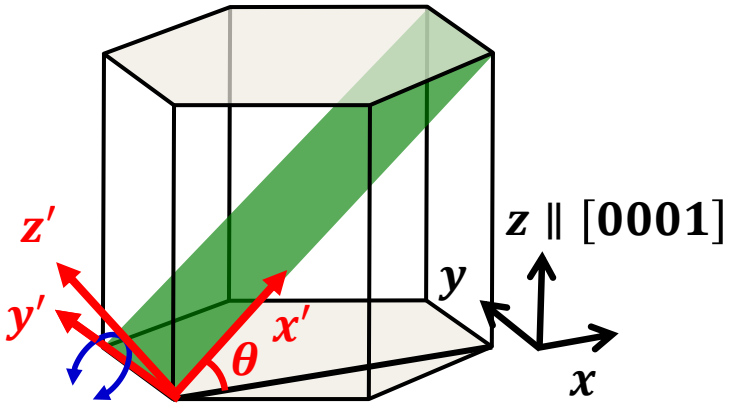

Figure 2.1: Definition of the (x, y, z) and (x', y', z') coordinate systems. θ is an off-angle of a growth plane from the c-plane.

where $E_{\mathrm{int}}^{\mathrm{well}}$ and $E_{\mathrm{int}}^{\mathrm{bar}}$ are electric fields along the z' axis in QWs and barriers, L_{w} and L_{b} are well width and barrier width, and $P'_{z'}$ and $\varepsilon_{z'}^{\prime\,\mathrm{P}}$ are effective polarization and permittivity expressed as

$$P'_{z'} = P_{z'} - \frac{\varepsilon^{\mathrm{P}}_{x'z'}}{\varepsilon^{\mathrm{P}}_{x'x'}} P'_{x'}, \tag{2.3}$$

$$\varepsilon_{z'}^{\prime\,\mathrm{P}} = \varepsilon^{\mathrm{P}}_{z'z'} - \frac{(\varepsilon^{\mathrm{P}}_{x'z'})^2}{\varepsilon^{\mathrm{P}}_{x'x'}}. \tag{2.4}$$

Here, the (x, y, z) and (x', y', z') coordinate systems are defined as shown in Fig. 2.1. Equation (2.1) is derived assuming $D_{z'} = 0$ (and the periodic boundary condition of electric potential), where D is the electric flux density. However, the in-plane electric field is not always zero under this assumption, which is a strange result. We used an alternative assumption that in-plane electric fields are zero for calculations of electric fields [1]. Under this assumption, the electric field along the z' axis is written as

$$E_i^{z'} = \sum_j \frac{\beta_j (P_j^{z'} - P_i^{z'})}{\varepsilon^{\mathrm{P}}_{z'z',\,i} \sum_j \beta_j}, \tag{2.5}$$

$$\beta_j = L_j / \varepsilon^{\mathrm{P}}_{z'z',\,j}, \tag{2.6}$$

[1] This is justified by two reasons. The first is that Fermi level is constant on in-plane surfaces under thermodynamic equilibrium states. The second is in-plane uniformity of donor and acceptor density, which leads to a uniform difference between Fermi level and conduction band minimum (and valence band maximum). Therefore, uniform electric voltage is derived, i.e. $E_{x'} = E_{y'} = 0$.

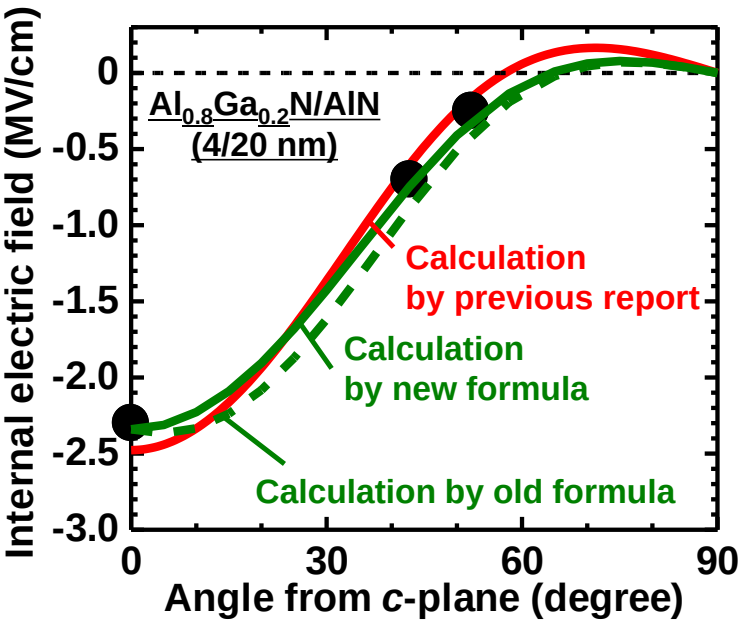

Figure 2.2: Angle dependences from c-plane of electric fields along the z' axis in $Al_{0.8}Ga_{0.2}N/AlN$ (4/20 nm) MQWs calculated by Eq. (2.1) and Eq. (2.5). The calculated result by the previous report is taken from [59].

where i, j represents each layer.

The difference in electric fields calculated by Eq. (2.1) and Eq. (2.5) is compared in Fig 2.2. We could not reproduce the calculation result of the previous study [59], but the newly calculated electric fields of c-QWs are in good agreement with the experimental result. In addition, the calculated electric fields in semipolar QWs by the newly developed formula (Eq.(2.5)) are in better agreement with the experimental results. Therefore, electric fields are calculated by Eq. (2.1) in this study.

Electric field and Overlap of Electron and Hole of $Al_{0.8}Ga_{0.2}N/AlN$ MQWs

Overlap integrals of electrons and holes are calculated by solving Schrödinger equations where the Hamiltonian of valence bands is based on $\boldsymbol{k} \cdot \boldsymbol{p}$ perturbation method [64]. The calculation method used in this study is basically the same as in previous reports [59, 64, 65], but there are some differences. Ratio of band offsets of conduction band (ΔE_c) and valence band of heavy holes (HH) (ΔE_v^{HH}) under an unstrained condition, ΔE_c:ΔE_v^{HH} was set to 7:3 in this study. Schrödinger equations are solved under the periodic bound-

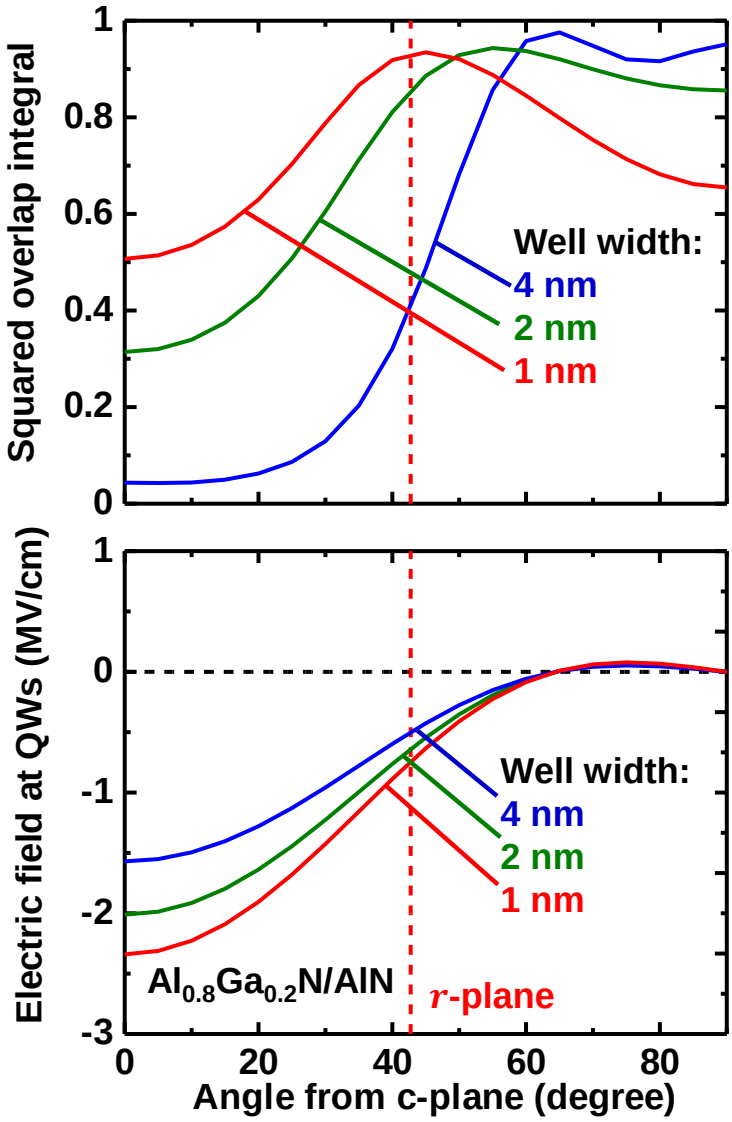

Figure 2.3: Calculated electric fields at QWs and squared overlap integrals of electrons and holes of $Al_{0.8}Ga_{0.2}N/AlN$ MQWs. The barrier width was set to 5 nm.

ary condition. Only ground states of electrons and holes are used for the subsequent calculations of various physical quantities in this Ph.D. thesis.

Figure 2.3 shows angle dependences from c-plane of squared overlap integrals of electrons and holes. The calculated structure is $Al_{0.8}Ga_{0.2}N$/AlN MQWs. The well width was set to 4 nm, 2 nm, and 1 nm and the barrier width was set to 5 nm. When the well width is 4 nm, the squared overlap integral of conventional c-QWs is less than 0.1. By contrast, that of r-QWs is over 0.35. In particular, when the well width is 2 nm or less, those of r-QWs are above 0.8, while those of c-QWs are less than 0.55. These high overlaps are one of the advantages of using r-plane. Interestingly, when the well width is 1 nm, r-QWs have almost the highest overlap compared to all planes. Larger angles from c-plane lead to larger overlaps by a reduction of electric fields. In addition, when the well width is small, penetration of wavefunctions decreases overlaps at much larger angles from c-plane. These are the reason why the r-plane has almost the highest overlap of all planes when the well width is 1 nm. In practice, the well width should be determined also taking into account critical thickness, CIEs, and LEEs.

2.3 Critical Thickness

2.3.1 Advantages of r-plane Compared to c-plane

Figure 2.4 shows off-angle and off-direction dependences of the critical layer thicknesses for various slip systems in $Al_{0.7}Ga_{0.3}N$/AlN heterostructures [66]. The critical thickness of just c-plane is about 20 nm, but critical thicknesses decrease drastically to about 4 nm when the off angle is changed very slightly (0.029° and 0.017° towards $\langle 1\bar{1}00\rangle$ and $\langle 11\bar{2}0\rangle$ directions, respectively [66]). These subtle off angles can exist in practical c-plane substrates. Critical thicknesses have maximum values at moderate off angles as shown in Fig. 2.4. This is a superiority of semipolar planes over (practical) c-plane.

2.3.2 Calculation of Critical Thickness of r-MQWs

We consider situations where AlGaN films are grown on ideal bulk AlN, followed by AlGaN/AlGaN MQWs as shown in Fig. 2.5. In order not to induce misfit dislocations on MQWs, MQWs should not be grown beyond their critical thickness. The dislocation densities of the r-AlN substrates used in this study are as high as about 10^7–10^8 cm^{-2}. Therefore, Matthews–Blakeslee's force balanced model [67], where misfit densities are generated by bending pre-existing dislocations, is used for calculations of critical thickness instead

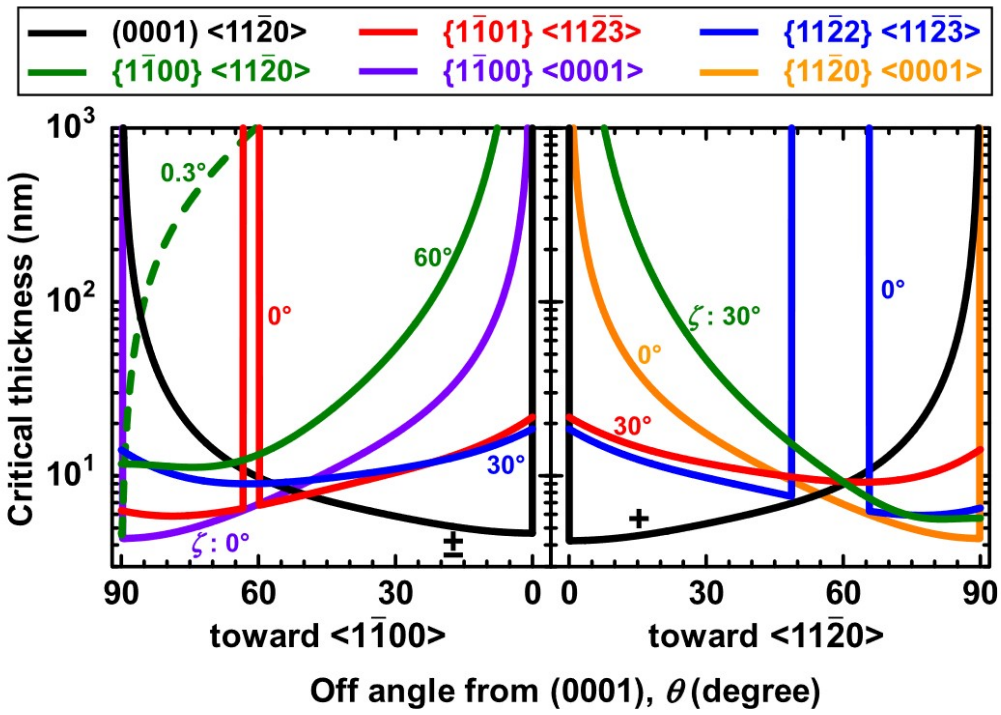

Figure 2.4: Off-angle and off-direction dependences of the critical thicknesses for various slip systems in $Al_{0.7}Ga_{0.3}N$/AlN heterostructures [66].

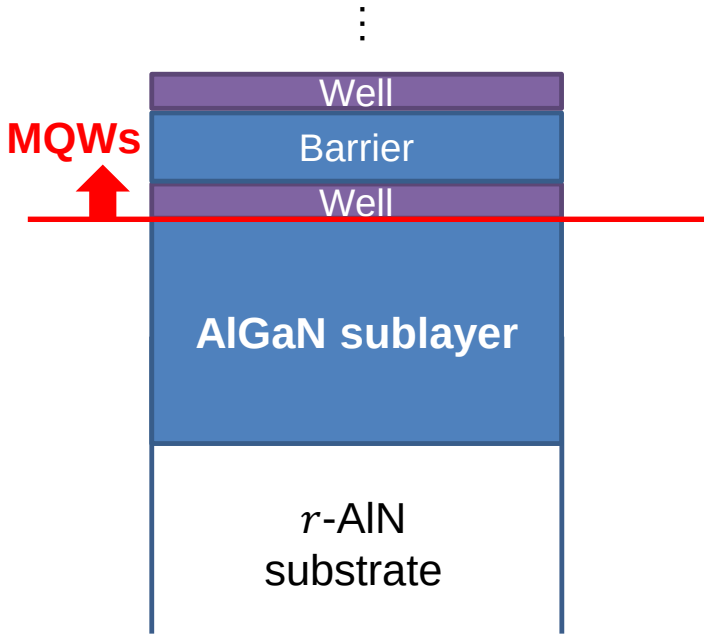

Figure 2.5: Situation for calculation of critical thickness of r-plane MQWs.

of People–Bean's energy balanced model [68], where misfit dislocations are newly generated when films are grown beyond their critical thicknesses. The slip plane was assumed to be the (0001) plane considering Fig. 2.4. The relaxation degrees of AlGaN sublayers were assumed not to change during the growth of subsequent MQW layers.

Relaxation of the sublayer has a strong effect on critical thicknesses. Figure 2.6 shows critical thickness of a single AlGaN film on an $Al_{0.75}Ga_{0.25}N$ film. Here, the situation is considered where the $Al_{0.75}Ga_{0.25}N$ film is grown on ideal AlN with different relaxation degrees. The definitions of coordinate systems are shown in Fig. 2.1. "90 % relaxed" shown in Fig. 2.6 means $r_{x'} = r_{y'} = 0.9$, where $r_{x'}$ and $r_{y'}$ are relaxation degrees toward x' and y' directions, and will be defined in detail in Sec. 3.6.1. Critical thickness depends on relaxation degrees of the sublayer as shown in Fig. 2.6. As relaxation proceeds, the critical thickness increases because the difference in lattice constants between the single r-AlGaN film and the AlGaN sublayer becomes small.

Critical thicknesses of r-MQWs were calculated by considering the entire layer as a single layer where AlN molar fraction of the single layer is equal to the average AlN molar fraction of the entire layer [69]. Table. 2.1 shows calculated maximum QW numbers without introducing misfit dislocations

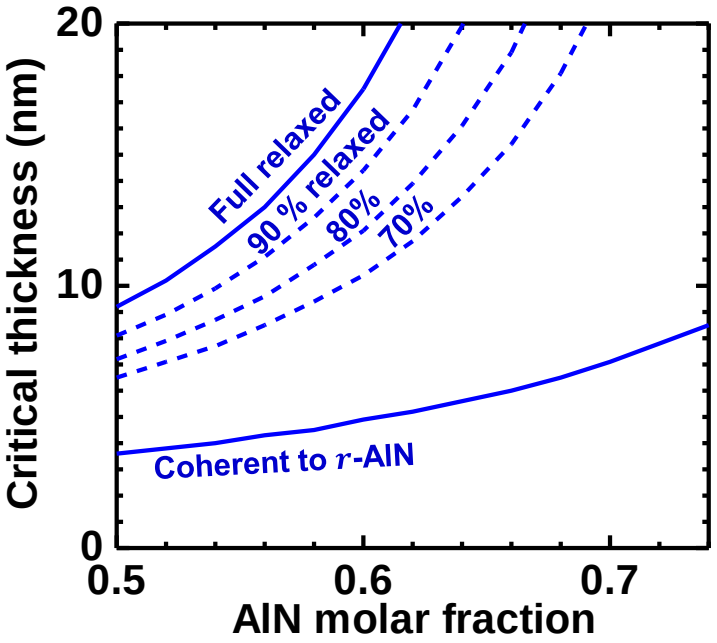

Figure 2.6: Calculated critical thicknesses of a single r-plane AlGaN film on $Al_{0.75}Ga_{0.25}N$/AlN depending on the relaxation degree of the $Al_{0.75}Ga_{0.25}N$ sublayer.

Table 2.1: Calculated maximum QW number without introducing misfit dislocations (r-plane).

For 265 nm LEDs ($Al_{0.5}Ga_{0.5}N$/$Al_{0.75}Ga_{0.25}N$ on $Al_{0.75}Ga_{0.25}N$)	
Well width	Maximum QW number
1.5 nm	5
2.0 nm	4
2.5 nm	3
For 230 nm LEDs ($Al_{0.75}Ga_{0.25}N$/$Al_{0.88}Ga_{0.12}N$ on $Al_{0.88}Ga_{0.12}N$)	
Well width	Maximum QW number
1.5 nm	13
2.0 nm	10
2.5 nm	8

(r-plane). $Al_{0.75}Ga_{0.25}N/Al_{0.88}Ga_{0.12}N$ MQWs on $Al_{0.88}Ga_{0.12}N$ are assumed for 230 nm LEDs. The barrier width was set to 5 nm, and the $(r_{x'}, r_{y'})$ was set to (1.0, 0.5) considering experimental results, which will be described in Sec. 3.6.2. The calculated maximum QW numbers are three or more than three, which is sufficient QW number. The difference in maximum QW number between 265 nm LEDs and 230 nm LEDs results from designed differences in AlN molar fractions between QWs and barriers.

2.4 Difference in Light Extraction between c-plane and r-plane

2.4.1 Calculation Formula of LEE

Formula for c-QWs

A radiative recombination rate is proportional to $|\langle\psi_{\mathrm{e}}|\boldsymbol{e}\cdot\hat{\boldsymbol{p}}|\psi_{\mathrm{h}}\rangle|^2$, where $|\psi_{\mathrm{e}}\rangle$ is the electron wavefunction, $|\psi_{\mathrm{h}}\rangle$ is the hole wavefunction, $\boldsymbol{e}$ is the unit vector with the (electric field's) direction of optical polarization, and $\hat{\boldsymbol{p}}$ is the momentum operator. In the case of nitride semiconductors, ψ_{e} and ψ_{h} are written as

$$\psi_{\mathrm{e}} = \phi_{\mathrm{e}}\,|S\rangle\,, \tag{2.7}$$

$$\psi_{\mathrm{h}} = g_x\,|X\rangle + g_y\,|Y\rangle + g_z\,|Z\rangle\,, \tag{2.8}$$

where ϕ_{e} and g_i $(i = x, y, z)$ are envelope functions of electrons and holes, $|S\rangle$ and $|I\rangle$ $(I = X, Y, Z)$ are s-orbital-like, and p_i-orbital-like basis functions $(i = x, y, z)$. If $\boldsymbol{e} = \sin\theta\cos\phi\boldsymbol{e}_x + \sin\theta\sin\phi\boldsymbol{e}_y + \cos\theta\boldsymbol{e}_z$ (coordinate system is taken as shown in Fig. 2.1), light intensity with polarization direction of $\boldsymbol{e}$, $I_{\boldsymbol{e}}$, seems to be as follow naively thinking,

$$I_{\boldsymbol{e}} \propto |\sin\theta\cos\phi M_x + \sin\theta\sin\phi M_y + \cos\theta M_z|^2, \tag{2.9}$$

$$M_x = \int \phi_{\mathrm{e}}^* g_x\,\langle S|p_x|X\rangle\,dz', \tag{2.10}$$

$$M_y = \int \phi_{\mathrm{e}}^* g_y\,\langle S|p_y|Y\rangle\,dz', \tag{2.11}$$

$$M_z = \int \phi_{\mathrm{e}}^* g_z\,\langle S|p_z|Z\rangle\,dz', \tag{2.12}$$

where M_i is the momentum matrix elements, z' is the growth direction. Therefore, naively thinking, LEE toward c-axis (LEE in the case of PL of

c-QWs) is described as

$$\left.\frac{\mathrm{d}\eta_{\mathrm{LEE},c}}{\mathrm{d}\theta}\right|_{\theta=0}\mathrm{d}\theta = \frac{\mathrm{d}\theta\int\mathrm{d}\phi|\cos\phi M_x+\sin\phi M_y|^2}{\int\int|\sin\theta\cos\phi M_x+\sin\theta\sin\phi M_y+\cos\theta M_z|^2\sin\theta\mathrm{d}\phi\mathrm{d}\theta}, \tag{2.13}$$

where $\eta_{\mathrm{LEE},c}$ is the total LEE of c-QWs (total reflection is not taken into consideration). However, when assuming $M_x = M_y = M$ considering symmetry of c-QWs, $|\cos\phi M_x + \sin\phi M_y|^2$ [in the numerator of Eq. (2.13)] is equal to $|M|^2$ when $\phi = 0$, and $|\sqrt{2}M|^2$ when $\phi = \pi/4$. This means that light intensities are different depending on a polarization direction even if the polarization direction is changed on c-plane. This result is strange. We consider the true equation of LEE in case of c-QWs, $\eta_{\mathrm{LEE},c}$ satisfies

$$\begin{aligned}&\left.\frac{\mathrm{d}\eta_{\mathrm{LEE},c}}{\mathrm{d}\theta}\right|_{\theta=0}\mathrm{d}\theta\\ &=\frac{\mathrm{d}\theta\int\mathrm{d}\phi\left(|\cos\phi M_x|^2+|\sin\phi M_y|^2\right)}{\int\int\left(|\sin\theta\cos\phi M_x|^2+|\sin\theta\sin\phi M_y|^2+|\cos\theta M_z|^2\right)\sin\theta\mathrm{d}\phi\mathrm{d}\theta}.\end{aligned} \tag{2.14}$$

Justification of Eq. (2.14)

Observed light is superposition of many photons emitted from various regions. Let the number of photons be N. The electric field of observed light, $\boldsymbol{E}$, is described as

$$\boldsymbol{E}(t) = \sum_{j=1}^{N}\boldsymbol{E}_j(t) \tag{2.15}$$

$$\boldsymbol{E}_j(t) = \mathrm{Re}\left\{\tilde{\boldsymbol{E}}_j(t)\right\} = \mathrm{Re}\left\{\tilde{E}_{x,j}(t)\boldsymbol{e}_x+\tilde{E}_{y,j}(t)\boldsymbol{e}_y+\tilde{E}_{z,j}(t)\boldsymbol{e}_z\right\} \tag{2.16}$$

$$\tilde{E}_{i,j} = E_{i,j}\exp\left(\mathrm{i}(\omega t+\phi_{i,j}(t))\right). \tag{2.17}$$

Thus, observed light intensity is described as

$$\langle|\boldsymbol{E}(t)|^2\rangle = \langle|\tilde{\boldsymbol{E}}(t)\tilde{\boldsymbol{E}}^*(t)|\rangle \tag{2.18}$$

$$= \left\langle\sum_{j,k}\left(\tilde{E}_{x,j}(t)\tilde{E}^*_{x,k}(t)+\tilde{E}_{y,j}(t)\tilde{E}^*_{y,k}(t)+\tilde{E}_{z,j}(t)\tilde{E}^*_{z,k}(t)\right)\right\rangle \tag{2.19}$$

$$\approx \sum_j\left(|E_{x,j}|^2+|E_{y,j}|^2+|E_{z,j}|^2\right). \tag{2.20}$$

Random change of phase was assumed for the last deformation of equation considering spontaneous emission from QWs. $\sum_j|E_{i,j}|^2$ in Eq. (2.20) corresponds to $|M_i|^2$.

Formula for QWs of arbitrary planes

We will extend Eq. (2.14) to QWs on arbitrary planes. First, we extend Eq. (2.13). The integrand in the numerator of Eq. (2.13) is written as the inner product of $\boldsymbol{e}_\phi = (\boldsymbol{e}_x, \boldsymbol{e}_y, \boldsymbol{e}_z)R_z(\phi)(1,0,0)^t$ and $\boldsymbol{M} = (\boldsymbol{e}_x, \boldsymbol{e}_y, \boldsymbol{e}_z)(M_x, M_y, M_z)^t$ (t means a transposed matrix), where $R_z(\phi)$ is a rotation matrix (rotation axis: z-axis) [2]. Similarly thinking, Eq. (2.13) is extended to be

$$\left.\frac{\mathrm{d}\eta_{\mathrm{LEE}}}{\mathrm{d}\theta'}\right|_{\theta'=0} \mathrm{d}\theta' = \frac{\mathrm{d}\theta' \int \mathrm{d}\phi' |\boldsymbol{e}_{\phi'} \cdot \boldsymbol{M}|^2}{\int\int |\sin\theta\cos\phi M_x + \sin\theta\sin\phi M_y + \cos\theta M_z|^2 \sin\theta \mathrm{d}\phi\mathrm{d}\theta}, \tag{2.21}$$

where $\boldsymbol{e}_{\phi'} = (\boldsymbol{e}_x, \boldsymbol{e}_y, \boldsymbol{e}_z)R_y(\theta_\mathrm{c})R_z(\phi')R_y(-\theta_\mathrm{c})(\cos\theta_\mathrm{c}, 0, -\sin\theta_\mathrm{c})^t$ and θ_c is the off-angle from c-plane. Finally, the extension of Eq. (2.14) is

$$\begin{aligned}&\left.\frac{\mathrm{d}\eta_{\mathrm{LEE}}}{\mathrm{d}\theta'}\right|_{\theta'=0} \mathrm{d}\theta' \\ &= \frac{\mathrm{d}\theta' \int \mathrm{d}\phi' M'}{\int\int (|\sin\theta\cos\phi M_x|^2 + |\sin\theta\sin\phi M_y|^2 + |\cos\theta M_z|^2)\sin\theta \mathrm{d}\phi\mathrm{d}\theta},\end{aligned} \tag{2.22}$$

$$\begin{aligned}M' = &\left|\left\{\left(\cos\phi'\cos^2\theta_\mathrm{c} + \sin^2\theta_\mathrm{c}\right)\cos\theta_\mathrm{c} - (\sin\theta_\mathrm{c}\cos\theta_\mathrm{c}(1-\cos\phi'))\sin\theta_\mathrm{c}\right\} M_x\right|^2 \\ &+ \left|\left\{(\sin\phi'\cos\theta_\mathrm{c})\cos\theta_\mathrm{c} - (-\sin\phi'\sin\theta_\mathrm{c})\sin\theta_\mathrm{c}\right\} M_y\right|^2 \\ &+ \left|\left\{(\sin\theta_\mathrm{c}\cos\theta_\mathrm{c}(1-\cos\phi'))\cos\theta_\mathrm{c} - \left(\cos\phi'\sin^2\theta_\mathrm{c} + \cos^2\theta_\mathrm{c}\right)\sin\theta_\mathrm{c}\right\} M_z\right|^2.\end{aligned} \tag{2.23}$$

2.4.2 Calculation Result of Light Extraction

$\mathrm{d}\eta_{\mathrm{LEE}}/\mathrm{d}\theta'|_{\theta'=0}$, which is proportional to light extraction in the growth direction (light extraction of PL measurement) was calculated in the case of c- and r-AlGaN/AlN and AlGaN/$Al_{0.9}Ga_{0.1}N$ MQWs. The well width and the barrier width were set to 1.5 nm and 5 nm, respectively. All layers were set to be coherent to ideal AlN in the case of AlGaN/AlN MQWs, and to ideal $Al_{0.9}Ga_{0.1}N$ in the case of AlGaN/$Al_{0.9}Ga_{0.1}N$ MQWs.

Figure 2.7 shows the calculated $\mathrm{d}\eta_{\mathrm{LEE}}/\mathrm{d}\theta'|_{\theta'=0}$. Light extraction from r-QWs is higher than that of c-QWs in the far-UVC region. On the other hand, c-QWs have higher light extraction in the other wavelength region. In order to investigate the reason for this trend, Fig. 2.8 shows calculation results of optical transition matrix elements, M_i, of AlGaN/AlN MQWs. In the case of c-QWs, M_z becomes higher than M_x and M_y at shorter wavelengths because

[2] $(\boldsymbol{e}_x, \boldsymbol{e}_y, \boldsymbol{e}_z)R_z(\phi)(1,0,0)^t$ means the result of rotation of $\boldsymbol{e}_x$

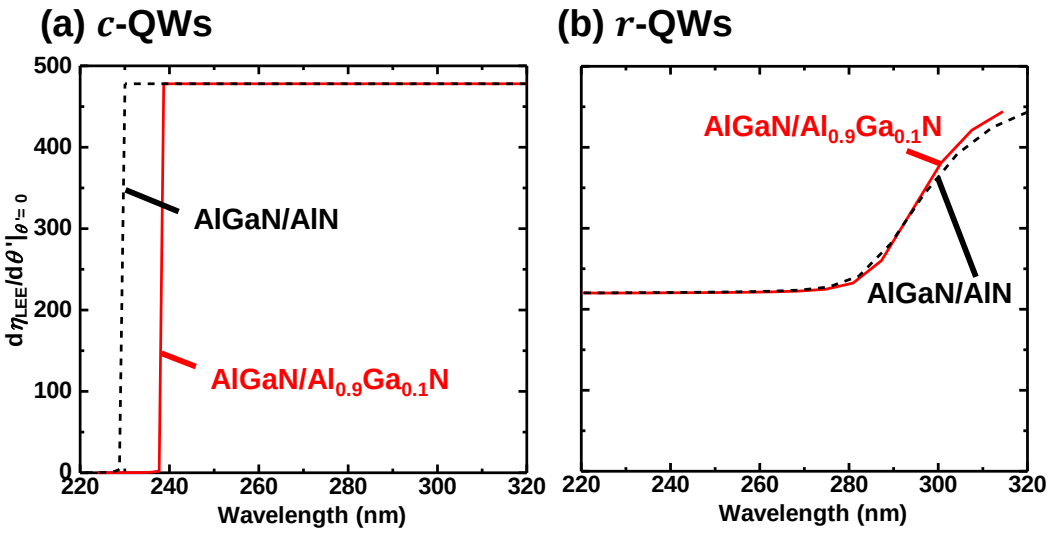

Figure 2.7: Calculated light extraction toward the growth direction.

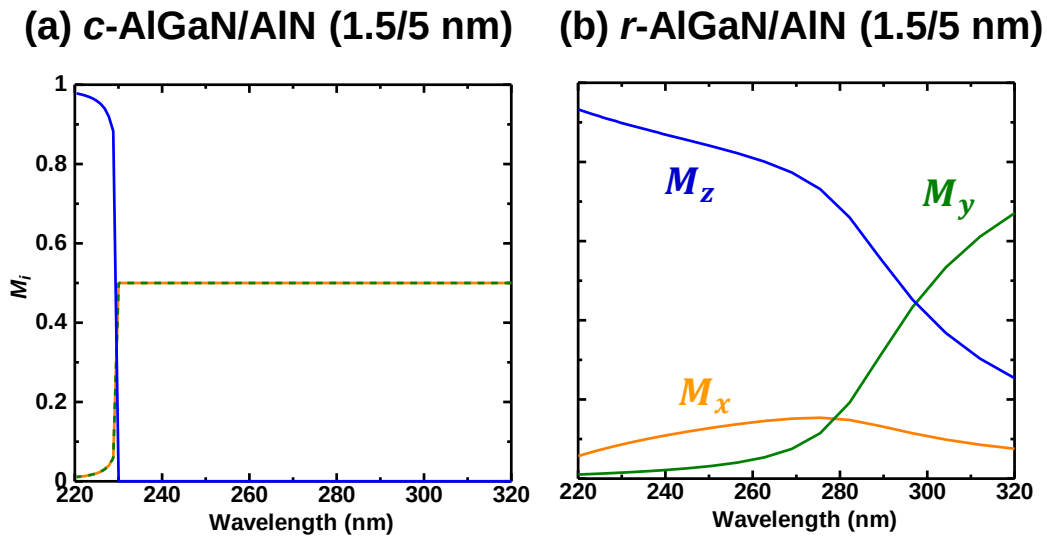

Figure 2.8: Calculation results of optical transition matrix elements of (a) c- and (b) r-AlGaN/AlN (1.5/5 nm) MQWs.

CH band becomes the top of valence bands. Therefore, $d\eta_{LEE}/d\theta'|_{\theta'=0}$ decreases drastically at shorter wavelengths in the case of c-QWs. By contrast, $d\eta_{LEE}/d\theta'|_{\theta'=0}$ of r-QWs decreases slightly at shorter wavelengths because of the reduction in M_y, but still remains high. As a result, r-QWs maintain a certain level of light extraction even in the far-UVC region.

When the barrier layer is changed from AlN to $Al_{0.9}Ga_{0.1}N$, the wavelength range of high light extraction decreases in the case of c-QWs. This is due to the reduction of barrier height and the reduced compressive strain [70]. Interestingly, r-QWs show almost no change in light extraction by the change in AlN molar fraction of barrier layer. Practically, the barrier layer must be AlGaN considering CIE as shown in the latter section (Fig. 4.13). Almost no change in light extraction by the use of AlGaN instead of AlN is the superiority of r-plane to c-plane especially in shorter wavelength regions.

2.5 Superiority of r-plane to Other Semipolar Planes in Terms of Current Injection Efficiency

Electric fields in r-plane QWs are lower than those in c-plane QWs as shown in Fig. 2.2. For example, however, $(11\bar{2}2)$ QWs (angle from c-plane: $\sim 58°$) have much lower internal electric field. Nevertheless, we expect r-plane LEDs to have better performance than $(11\bar{2}2)$ LEDs. Figure 2.9 (a) shows CIEs of far-UVC LEDs calculated by a commercial device simulator (SiLENSe v.6.4 or v.6.5, STR Corporation [71]) and Fig. 2.9 (b) shows the structure used in the calculations. Dislocation density was set to 0. As a result, IQEs are always calculated as 1 and ideal conditions can be considered. The calculated CIE of the r-plane LED is slightly lower than that of the c-plane LED but remains high. By contrast, the calculated CIE decreases drastically when the off angle is inclined to that of $(11\bar{2}2)$. This result can be understood from the calculated band diagrams at ~ 20 A/cm^2 shown in Fig. 2.10. The barrier height of EBL to electron becomes lower and that to hole becomes higher as the inclination angle becomes higher. Either or both of them increase the ratio of electron current to total current at p-layers. The reason for the change in the barrier height with increasing off angle is the reduction in polarization because the difference in polarization induces band bending. The calculated result indicates that moderate polarization enhances CIEs. This is the reason for the superiority of r-plane to other semipolar planes whose inclination angle is higher than that of r-plane. Considering IQE will be enhanced by the reduction of internal electric fields by inclining the angle

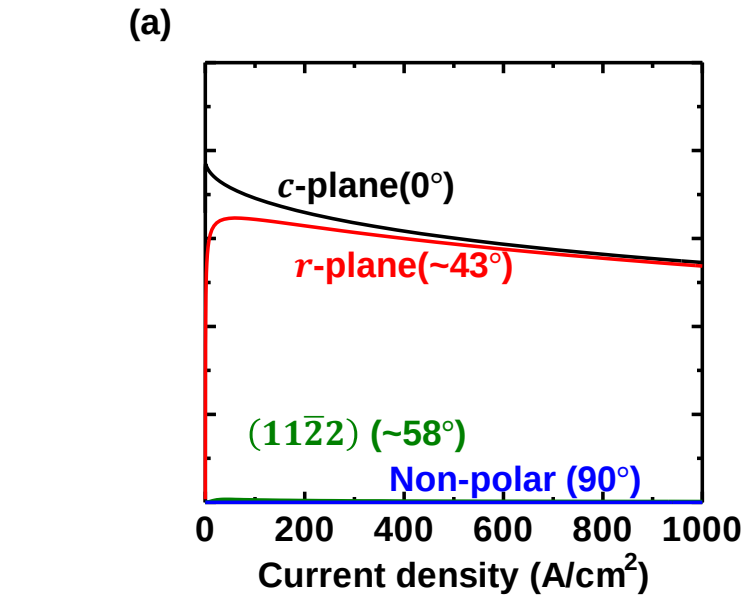

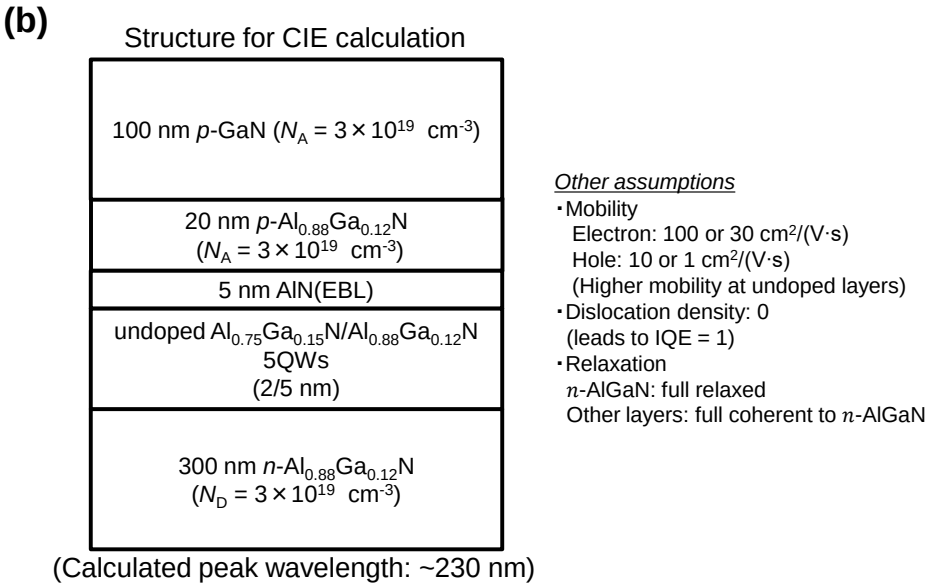

Figure 2.9: (a) Calculated CIEs on various planes, (b) Structure for CIE calculation.

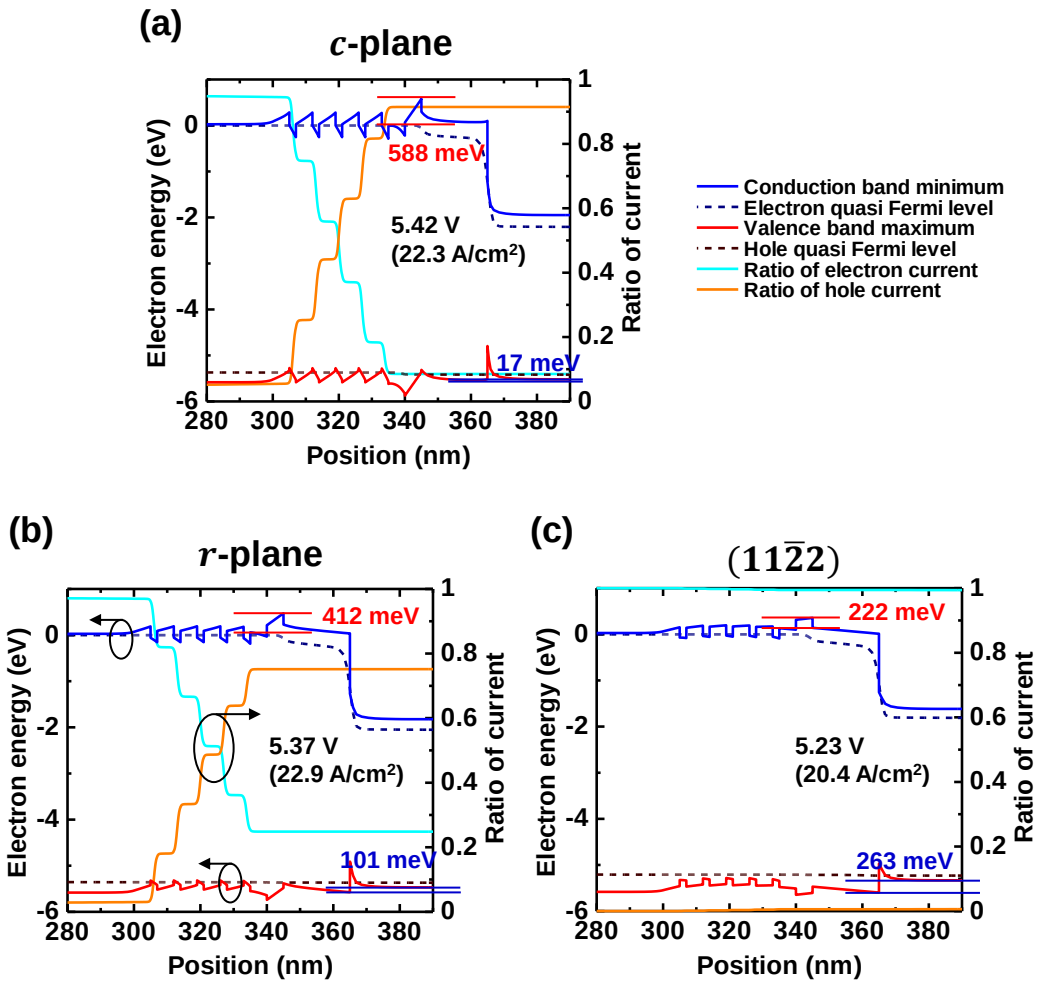

Figure 2.10: Calculated band diagrams and ratios of electron current and hole current at ∼20 A/cm^2 on (a) c-plane, (b) r-plane, and (c) (11$\bar{2}$2).

from c-plane (Fig. 2.3), r-plane may be the most suitable plane for AlGaN-based LEDs.

In addition, we have recently found through theoretical calculations [72] that polarization doping is effective to achieve high hole density not only when the c-plane is used but also when the r-plane is used as the growth plane. Since the ionization energy of Mg acceptor in AlN is too high [4,73,74], obtaining p-AlGaN with high AlN molar fraction is difficult. This result will also be an advantage of r-plane LEDs.

2.6 Summary

In this chapter, advantages of r-plane LEDs over c-plane LEDs were theoretically investigated in terms of IQEs, LEEs, and CIEs. First, advantages in terms of IQE were investigated. Squared overlap integral of electrons and holes of 2-nm-thick r-plane QWs is higher than that of 1-nm-thick c-QWs. Critical thickness of r-plane AlGaN is larger than that of practical c-plane (i.e. c-plane with slight off angle). The maximum number of r-plane QW without introducing misfit dislocations is three or more than three when the well width is 2.5 nm or less than 2.5 nm. In terms of LEE, r-QWs were found to show their superiority to c-QWs especially in the far-UVC region by the calculation of optical transition matrix elements. The CIE decreased as the growth plane was inclined from c-plane, but r-plane (43° from c-plane) LEDs have enough high CIEs. However, when a growth plane was inclined to $(11\bar{2}2)$ plane (58° from c-plane), CIEs decreased drastically. The reason for the drastic decrease in CIEs was found to be the reduction of electric polarization. Considering the balance of IQE, LEE, and CIE, r-plane is the most favorable plane for UVC LEDs.

Chapter 3

Growth of Semipolar r-plane AlGaN Films

3.1 Introduction

Our group has been fabricated homoepitaxial r-AlN with smooth surfaces by metalorganic vapor phase epitaxy (MOVPE) method [58–60]. However, AlGaN films are necessary for fabricating LEDs because of high resistivity of n-type AlN fabricated by MOVPE method [4, 62, 63]. Fabrication of Si-doped AlN with low resistivity by MOVPE method is currently difficult[1]. Therefore, r-AlGaN with smooth surfaces are fabricated in this chapter.

3.2 Experimental Conditions

3.2.1 Growth Method and Growth Machine

AlGaN epitaxial layers were fabricated by MOVPE method. Trimethylaluminum (TMA), trimethylgallium (TMG), and ammonia (NH_3) were used as precursors of Al, Ga, and N elements. H_2 is used as carrier gas. r-AlN sub-

[1]There are some reports of Si-doped AlN with low resistivity. Si-doped AlN with resistivity below 0.1 $\Omega \cdot$ cm has recently been achieved in Si-implanted AlN annealed under UV illumination [75] and Si-doped AlN fabricated by plasma-assisted molecular beam epitaxy (MBE) using metal modulation epitaxy (MME) [76]. The reason for the low resistivity might be that the true ionization energy of Si donor in AlN is low. Ionization energy of Si in AlN has been thought to be high from results of Hall effect measurement [4, 62, 63] and calculations by density functional theory using hybrid functional [77, 78]. However, our group has recently found that ionization energy of Si is 64.8 meV from PL measurement of high quality homoepitaxial Si-doped AlN and that this value is close to the theoretical value (67.2 meV) [79].

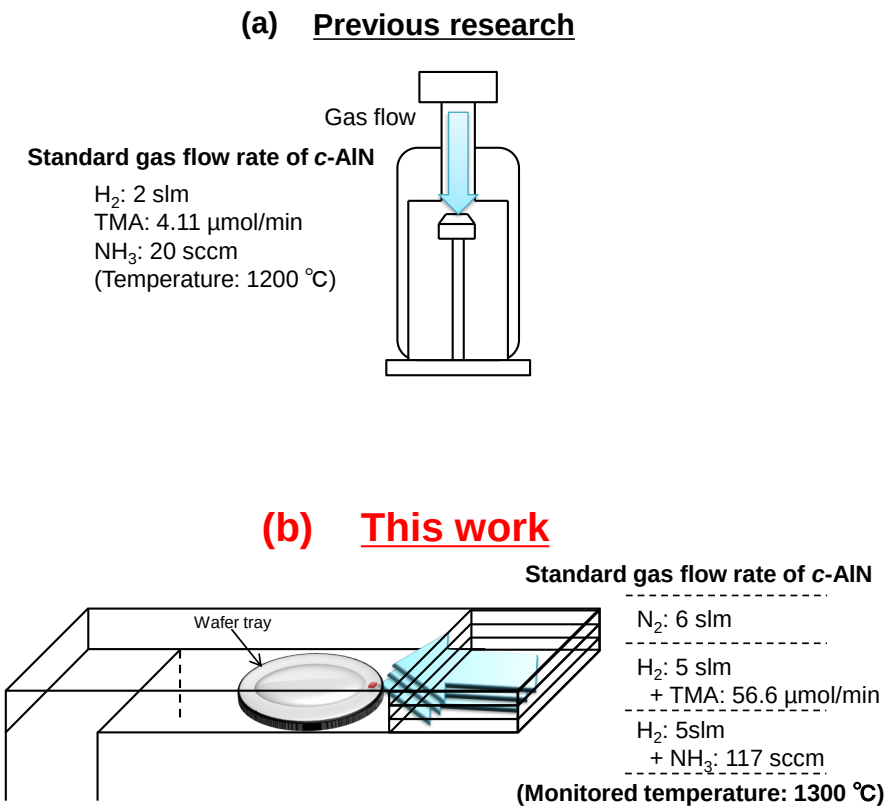

Figure 3.1: MOVPE machines used in (a) the previous study [58–60], and (b) this study.

strates used in this study were prepared by physical vapor transport (PVT) method. The Si, C, and P impurity levels are as low as 9.4×10^{15}, 1.1×10^{17}, and 3.4×10^{17} cm^{-3}, respectively. Hence, the AlN substrates with a thickness of 450 μm have a transmittance as high as $\geq$50% in a wavelength range of 250–280 nm. Prior to growth, the AlN substrates were subjected to wet etching in a 3:1 H_2SO_4:H_3PO_4 mixture for 10 min at 90 °C to remove the surface aluminum hydroxide [80].

In this study, we changed the growth machine from the previous one. Figure 3.1 shows schematic images of growth machines used in the previous study [58–60] and in this study. There are some differences between the previous machine and the current one. Firstly, the reactor configuration is different; a vertical type in the previous study and a horizontal type in this study. Secondly, the size of the previous machine is small and only small samples can be placed on the succeptor. By contrast, that of the current machine is large and a 2 inch substrate can be placed.

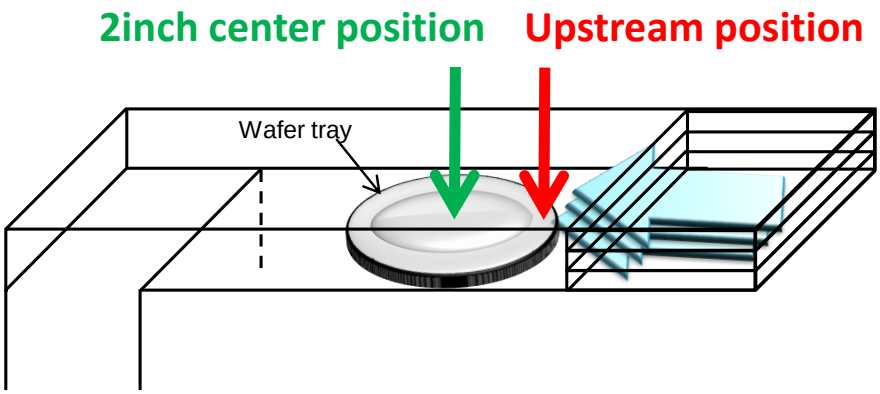

Figure 3.2: Substrate setting positions used in this study. The green arrow marks the usual position, and the red arrow marks the upstream position for growth under high pressure conditions.

3.2.2 Growth Position

In the previous study, high pressure growth such as 500 Torr was found to be suitable for fabrications of semipolar plane homoepitaxial AlN layers with smooth and pit-free surfaces instead of usually adopted low pressure such as 76 Torr [58–60]. On the other hand, high pressure usually reduces the growth rate of AlN [81] because pre-reactions between TMA and NH_3 in gas phase are more likely at high pressure. As described in Sec. 3.2.1 we changed growth machine after the previous study. This change will affect on the degree of reduction in growth rate. In fact, AlN could not be fabricated at 500 Torr at the usual substrate setting position of the current machine (described by the green arrow in Fig. 3.2, we refer to this position as 2 inch center position in this thesis) .

Therefore, a position closer to the gas inlet is used, as indicated by the red arrow in Fig. 3.2 (we refer to this position as the upstream position) for growth under high pressure conditions. Figure 3.3 shows pressure dependences of standard *c*-plane AlN growth rate of each machine. Here, the shown AlN growth rate of the current machine is that of AlN fabricated at the upstream position. TMA flow rate and NH_3 flow rate of the current machine are 56.6 µmol/min and 5.22 mmol/min, respectively. In the case of the current machine, growth rate decreased drastically by increasing growth pressure. For example, the growth rate at 76 Torr at the upstream position is ∼6 µm/h (∼2 µm/h at 2inch center position), and the growth rate at 500 Torr at the upstream position is 0 µm/h (0 µm/h at 2inch center position). Therefore, it is difficult to fabricate AlN at high pressure with the current

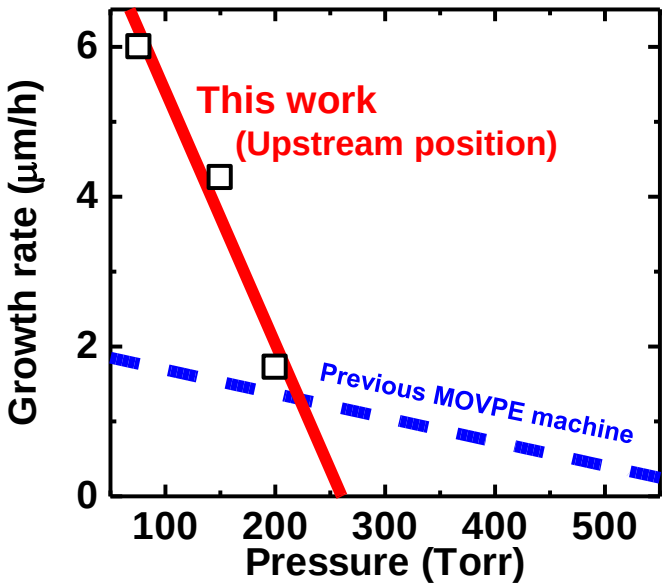

Figure 3.3: Growth rates of AlN using the previous MOVPE machine [58–60] and the current one.

machine. The difference between the current machine and the previous one might result from the difference in configuration type. A study also reported that the reduction of growth rate in horizontal configuration is more severe than that of a vertical type [81]. Therefore, samples were fabricated at 200 Torr and at the upstream position in the early stage of this study. The growth rate at 200 Torr at the upstream position is ∼2 µm/h (0 µm/h at 2inch center position) when TMA and NH_3 flow rates are 56.6 µmol/min and 5.22 mmol/min.

3.2.3 Substrate Setting at the Upstream Position

In this research, it sometimes happens that substrates are blown away by gas flow change during growth or before/after growth because used substrates are small. Therefore, the substrate setting was changed as the research progressed. Figure 3.4 shows the substrate settings in this research. A sapphire substrate holds the substrate for growth to prevent from being blown away in substrate setting 1. In addition to that, such a sapphire is adhered to another sapphire substrate by AlN paste in substrate setting 2. In substrate setting 3, a counterbore is added to the wafer tray at the growth position and the substrate is surrounded by sapphire substrates in order to reduce effects of steps between the substrate and the wafer tray on gas flow. In fact,

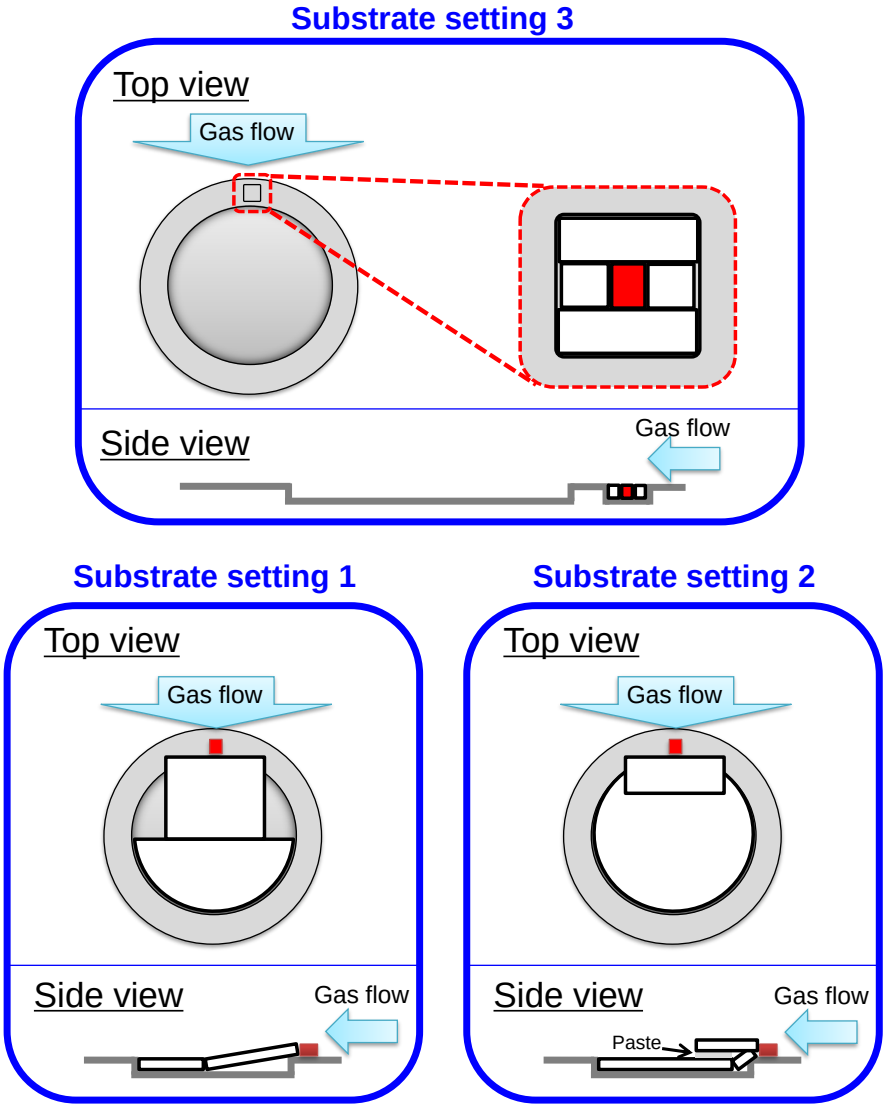

Figure 3.4: Substrate settings at the upstream position used in this study.

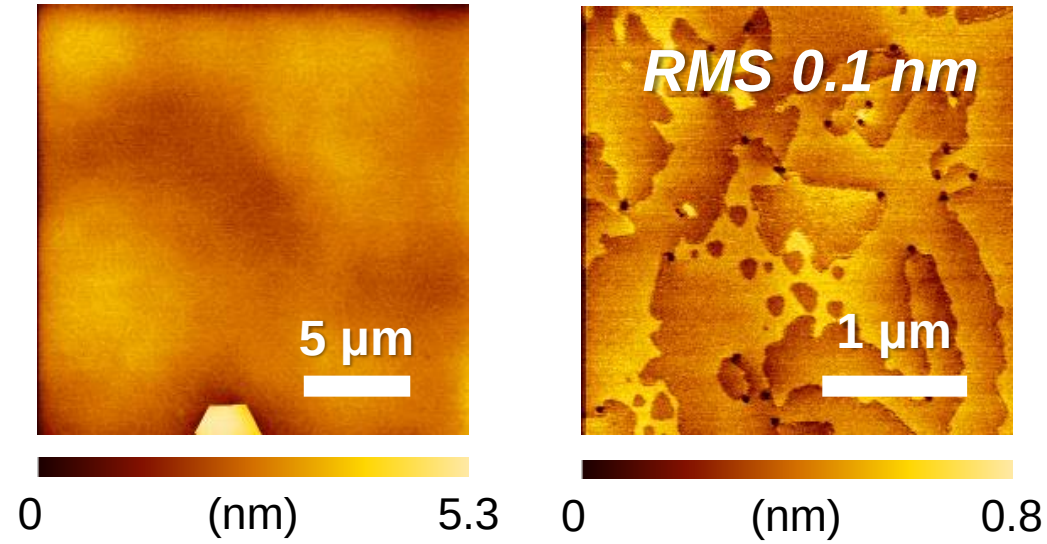

Figure 3.5: AFM images of c-AlN on a 2inch sapphire substrate grown under the standard condition of the current MOVPE machine.

a change in the substrate setting changed surfaces of epi-layer, and substrate setting 1 and 2 had a poor effect on reproducibility when sapphire holders were remade. Although substrate setting 3 has been adopted finally, this thesis also uses data from samples fabricated under other substrate settings. We will explicitly mention it when such data are used.

3.3 Growth of r-AlGaN under High Pressure Condition

3.3.1 AlN

Prior to the growth of homoepitaxial r-AlN films, c-AlN films were fabricated on a 2inch sapphire substrate at a low pressure (76 Torr). Figure 3.5 shows the AFM images of the fabricated c-AlN/sapphire. Smooth surfaces with step terrace structures are well observed although a bit of hexagonal hillocks which result from nitridation process [82] are also observed.

Then, homoepitaxial r-AlN films were fabricated. Figure 3.6 describes the growth profile of homoepitaxial r-AlN films. The growth temperature was set to 1300 °C[2], which is the optimal growth temperature of c-AlN on

[2]Growth temperature is the monitored temperature in this thesis.

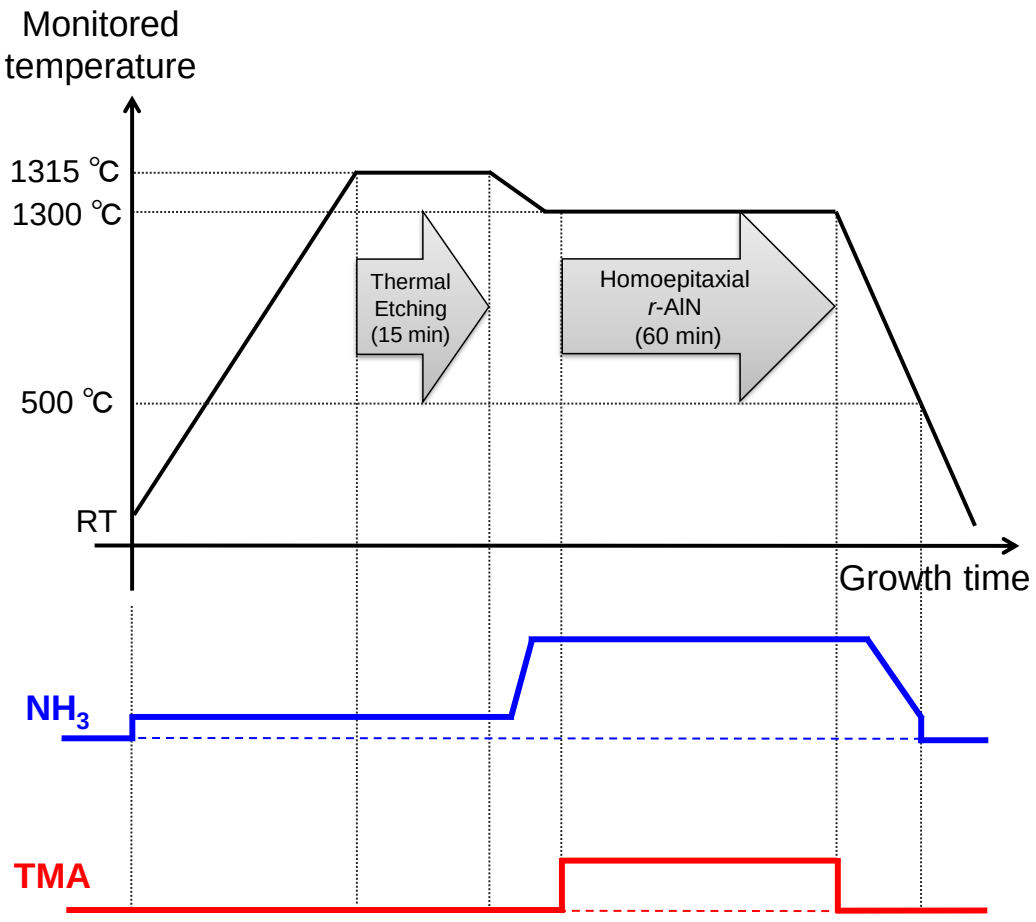

Figure 3.6: Growth sequence of homoepitaxial r-AlN films.

c-sapphire substrates of the current MOVPE machine. The growth time was 60 min and thermal annealing process was performed for 15 min before the growth. *r*-AlN films were fabricated at various TMA flow rates and input [3] V/III ratios while monitored growth temperature and pressure were fixed at 1300 °C and 200 Torr. Growth rates were estimated from AlN grown side-by-side or grown under the same growth condition on sapphire substrates. No difference in growth rates between *c*-plane and *r*-plane AlN is confirmed by cross-sectional scanning electron microscopy (SEM) and scanning transmission electron microscopy (STEM).

Figure 3.7 shows AFM images of the fabricated AlN surfaces. Smooth surface morphology and low root mean square (RMS) of surface roughness (0.5 nm at pit-free region) were obtained under a certain growth condition (TMA flow rate: 72 µmol/min, NH_3 flow rate: 20 mmol/min). Figure 3.8 shows the AFM images in Fig. 3.7 ordered by NH_3 flow rate in order to investigate the reason for the change in surface morphology. It is found that higher NH_3 flow rate seems to reduce pit density. However, growth rates also decrease with increasing NH_3 flow rate. To investigate the effects of growth rate, an *r*-AlN film was fabricated by decreasing TMA flow rate at a low NH_3 flow rate (high pit density condition in Fig. 3.8). Figure 3.9 shows AFM images of *r*-AlN grown at the original and a reduced growth rates under a low NH_3 frow rate condition (left side in Fig. 3.9). Here, the substrate setting is changed by the progress of research. Therefore, an AFM image of *r*-AlN fabricated under the different substrate setting but the best gas flow rate condition found above is also shown in Fig. 3.9 (right side). Simple comparison might be difficult since the growth rate was different under the new substrate setting, but higher NH_3 flow rate at fixed growth rate ($\sim$1 µm/h) enables low pit density. From this result, we considered the main reason for the reduction in large pit density is the increase in NH_3 flow rate. By contrast, small pits appear when NH_3 flow rate was increased too much as shown in Fig. 3.8. The same tendency is observed when *r*-AlGaN films are fabricated, which will be described in Sec. 3.4. The details including possible mechanisms of pit formation and elimination will be described in Sec. 3.5.

3.3.2 AlGaN

AlGaN films are necessary for fabricating LEDs because of high resistivity of *n*-type AlN fabricated by MOVPE method [4, 62, 63]. Thickness used for *n*-type AlGaN films of horizontal type LEDs is typically $\sim$2 µm [83–87]

[3] The actual V/III ratio (V/III ratio near a substrate, not near the gas inlet) will be larger than input V/III ratio because of pre-reaction of TMA and NH_3 and higher NH_3 flow rate than TMA flow rate.

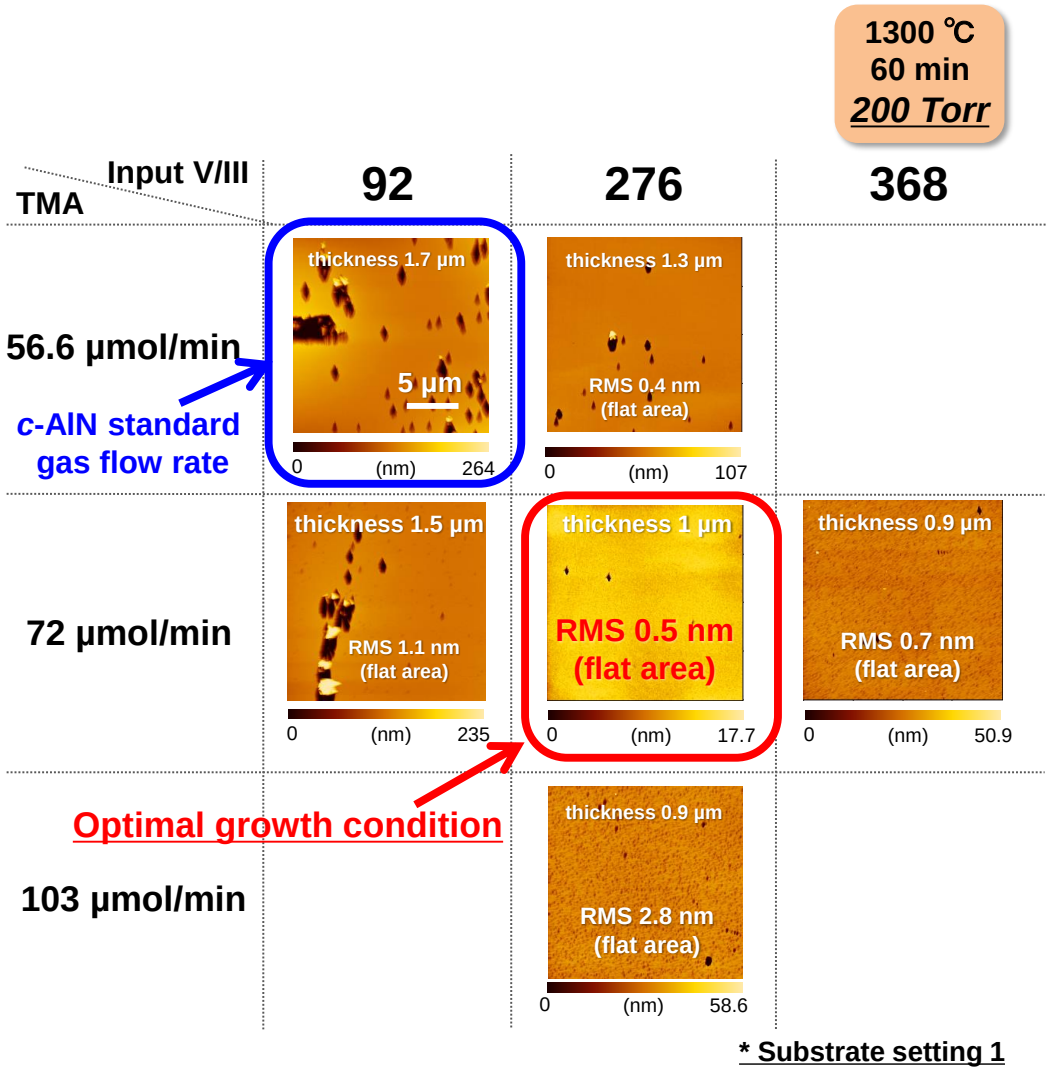

Figure 3.7: AFM images of homoepitaxial r-AlN films grown at the upstream position.

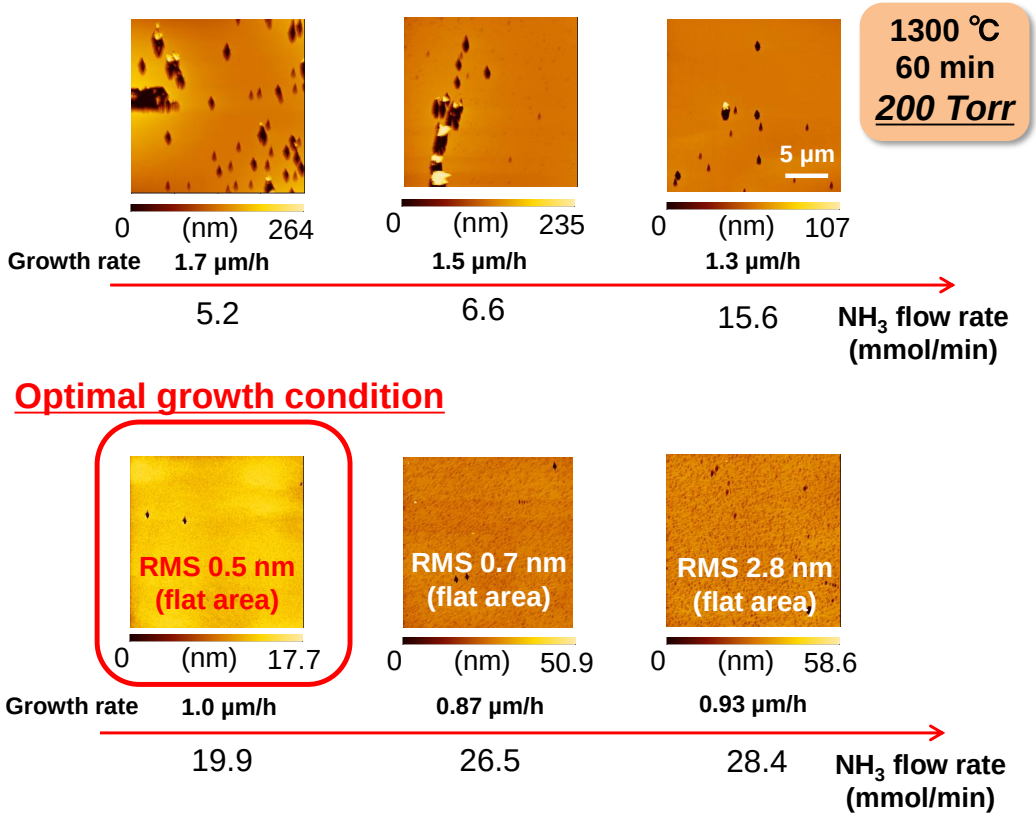

Figure 3.8: Reordered AFM images of homoepitaxial r-AlN films in Fig. 3.7.

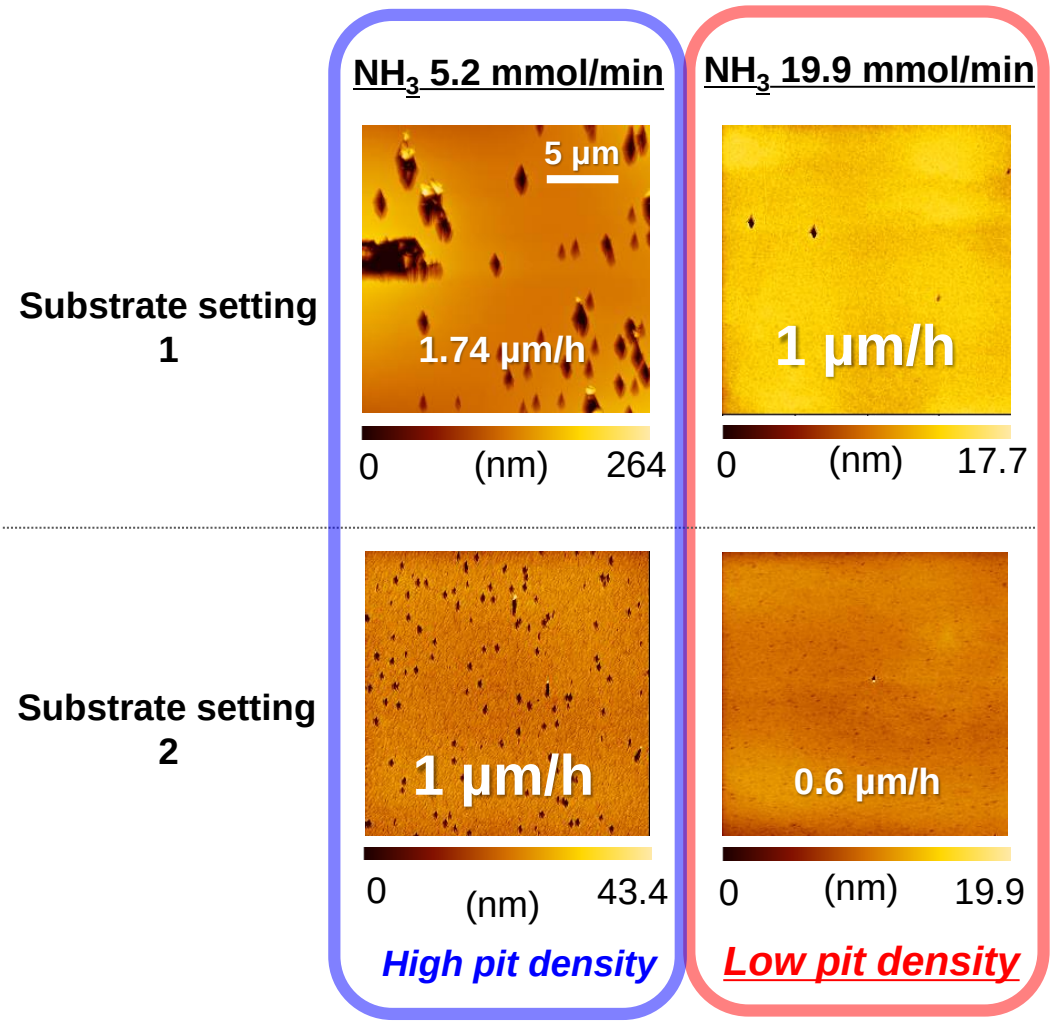

Figure 3.9: Effect of growth rate and NH_3 flow rate on pit density of r-AlN.

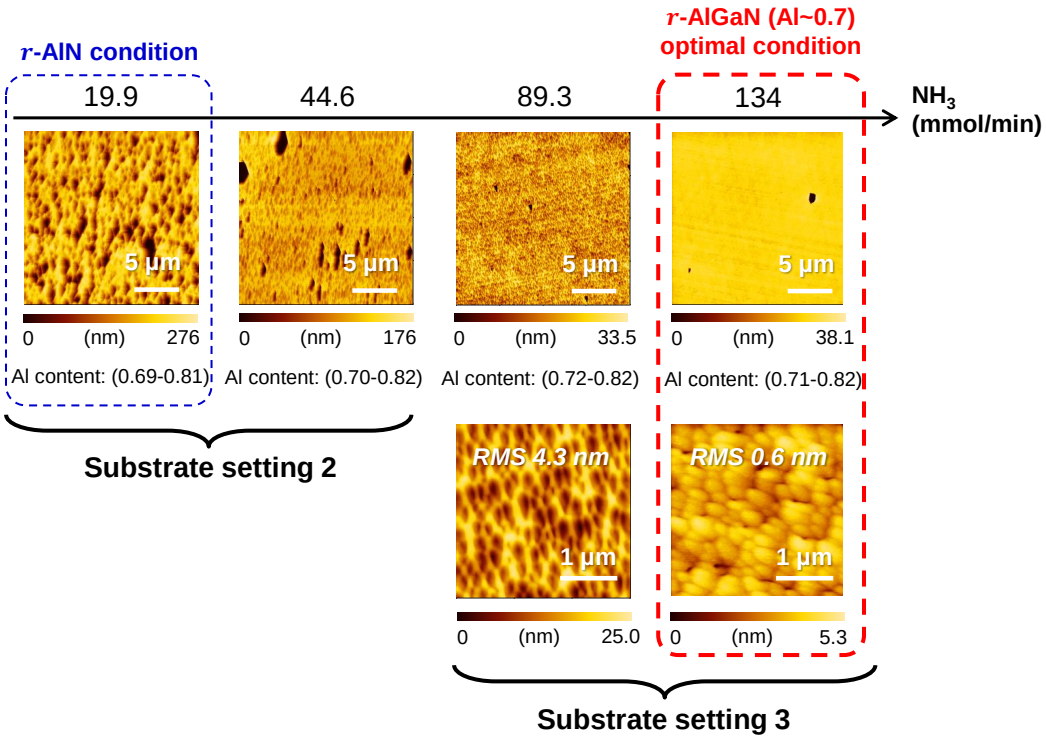

Figure 3.10: NH_3 flow rate dependence of AFM images of r-AlGaN films (AlN molar fraction $\sim$0.7). AlN molar fractions were estimated by symmetric XRD 2θ-ω scan of r-plane assuming fully relaxed (smaller AlN molar fraction) or fully coherent to ideal AlN (larger AlN molar fraction).

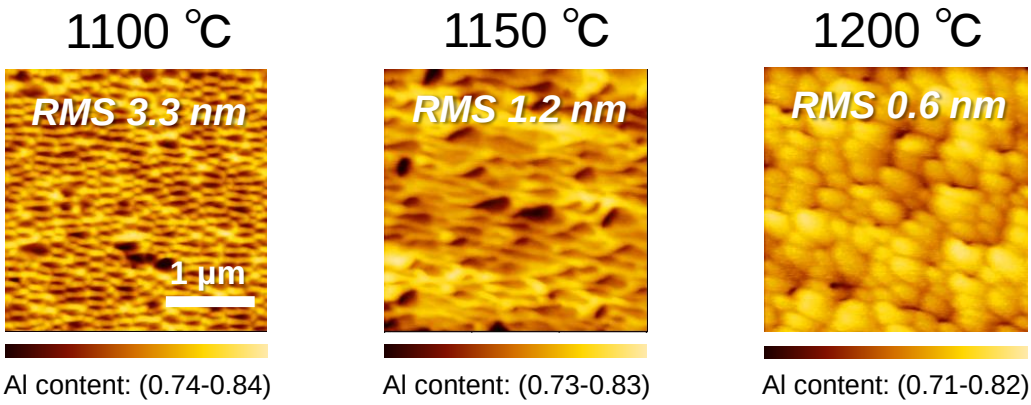

Figure 3.11: Growth temperature dependence of AFM images of r-AlGaN films (AlN molar fraction ∼0.7). AlN molar fractions were estimated by symmetric XRD 2θ-ω scan of r-plane assuming fully relaxed (smaller AlN molar fraction) or fully coherent to ideal AlN (larger AlN molar fraction).

considering series resistance. Therefore, optimal growth conditions of thick r-plane AlGaN films were investigated. Firstly, sum of TMA and TMG flow rates was set to 72 µmol/min, which is the best TMA flow rate of r-AlN found in Sec. 3.3.1, and growth temperature was set to 1200 °C. Decreased growth temperature was aimed to facilitate Ga incorporation. Growth time was set to 70 min or 60 min. Figure 3.10 shows AFM images of fabricated AlGaN films at various NH_3 flow rates. The ratio of TMA and TMG was adjusted to fix AlN molar fraction between 0.7–0.8. In addition, the substrate setting was changed depending on the progress of this study. AlN molar fractions of fabricated r-AlGaN films estimated by symmetric XRD 2θ-ω scan are 0.69–0.72 assuming fully relaxed and 0.81–0.82 assuming fully coherent to ideal AlN. Considering the experimental result which will be described in Sec. 3.6.2, AlN molar fractions under the fully relaxed condition will be close to the actual ones. Increase in NH_3 flow rate is also effective in the case of $Al_{0.7}Ga_{0.3}N$. RMS of surface roughness of $Al_{0.7}Ga_{0.3}N$ grown under the optimal NH_3 flow rate (134 mmol/min) is 0.6 nm in pit-free region.

Growth temperature dependence of surface morphology of r-AlGaN films was also investigated because a higher growth temperature might introduce higher density of point defects[4]. Figure 3.11 shows growth temperature de-

[4]The number of point defects, n, is described as $n/N = A\exp(-E^{\mathrm{f}}/k_{\mathrm{B}}T)/(1 + A\exp(-E^{\mathrm{f}}/k_{\mathrm{B}}T))$, where N is the site number of point defects, k_{B} is the Boltzmann constant, T is the absolute temperature, E^{f} is the formation energy of point defects, $A = \exp(-\Delta s/k_{\mathrm{B}}T)$, and Δs is the formation entropy of point defects. Increase in tem-

pendence of AFM images of r-AlGaN films (AlN molar fraction ∼0.7). The growth time, NH_3 flow rate, sum of TMA and TMG flow rates were set to optimal ones in Fig. 3.10 (60 min, 134 mmol/min, and 72 µmol/min, respectively). The ratio of TMA and TMG was adjusted so that AlN molar fraction became ∼0.7. Poor surface morphology was observed at reduced temperatures as shown in Fig. 3.11. We consider that the poor surface morphology resulted from the formation of pits as will be discussed in Sec. 3.5. The optimal temperature of r-AlGaN films (AlN molar fraction: ∼0.7) was found to be 1200 °C.

3.3.3 GaN

Due to poor electric conduction [4, 88, 89] and high work function [90] of Mg-doped p-AlGaN, forward voltages of UV-LEDs without p-GaN are high [23, 91–94]. Therefore, current UV-LEDs typically use GaN as a p-type layer and/or a contact layer [24, 83, 84, 87, 95–118]. In order to use r-GaN as a p-type layer, growth conditions of r-GaN were investigated. The NH_3 flow rate was 134 mmol/min, and the TMG flow rate was 28.8 µmol/min, which is the same value as the optimal r-$Al_{0.7}Ga_{0.3}N$ fabricated in Sec. 3.3.2. The growth temperature was reduced to 1000 °C. Prior to growths, $Al_{0.7}Ga_{0.3}N$ was fabricated under the optimal condition described in Sec. 3.3.2. Figure 3.12 shows NH_3 flow rate dependence of AFM images of r-GaN. When NH_3 flow rate is 134 mmol/min, which is the optimal value of growths of r-$Al_{0.7}Ga_{0.3}N$ (Sec. 3.3.2), a lot of pits are observed. Increase in NH_3 flow rate to 223 mmol/min (V/III: 7758) enables the reduction of pit density. Therefore, in this study, the optimal NH_3 flow rate of r-GaN is 223 mmol/min. The growth rate was ∼60 nm/h. Practically higher growth rate may be suitable for the industrial use, and should be achieved in the future.

3.4 Growth of r-AlGaN under Low Pressure Condition

We succeeded in fabricating AlGaN films with smooth surfaces in Sec. 3.3.2. However, in the case of the MOVPE machine of this study (Fig. 3.3), loss of precursors at high pressure growth was found to be severe, which is not economical. In addition, this often clogs up the filter in front of the pump.

perature results in higher n/N if E^f is independent of temperature. However, E^f depends on Fermi level and Fermi level depends on temperature. Therefore, the situation is more complicated.

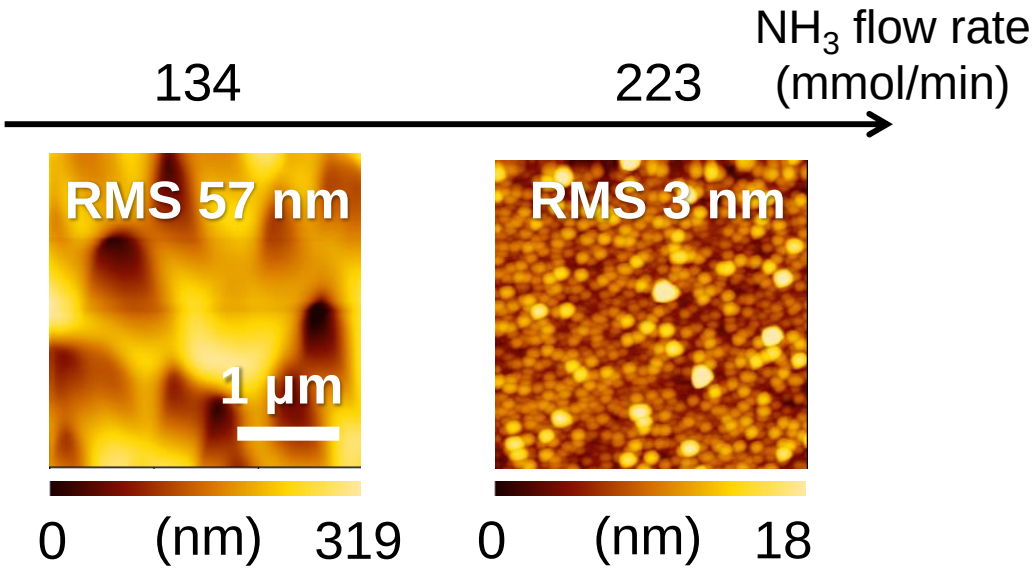

Figure 3.12: NH_3 flow rate dependence of AFM images of r-GaN.

These will be obstacles to the expansion of r-plane AlGaN LEDs into industrial applications. Therefore, AlGaN growth under low pressure conditions at 2 inch center position was explored.

AlN molar fraction: ∼0.75

We firstly tried to fabricate r-AlGaN with AlN molar fraction of ∼0.75. NH_3 flow rate and growth temperature were set to 134 mmol/min and 1200 °C, respectively. These are the optimal values in Sec. 3.3.2. However, the TMA flow rate and growth pressure were set to 56.6 µmol/min and 38 Torr, respectively. These are the optimal values of c-AlN at 2 inch center position. The TMG flow rate was determined to be 19.1 µmol/min (TMA/(TMA+TMG) is 0.75) so that AlN molar fraction becomes ∼ 0.75. Figure 3.13 shows AFM images of the fabricated r-AlGaN. The AlN molar fraction estimated by the method described in Sec. 3.6.1 is 0.76. Although there are still a few pits, the RMS in 3×3 µm^2 is as low as 0.8 nm, which is low enough to fabricate QWs. The possibility of obtaining smooth surfaces even at low pressure has been confirmed.

There is a trade-off between the absorption of radiation emitted from QWs and the resistivity of n-AlGaN when fabricating UVC LEDs emitting at shorter wavelengths because the resistivity of n-AlGaN increases drastically at higher AlN molar fractions [119]. For example, the AlN molar fraction

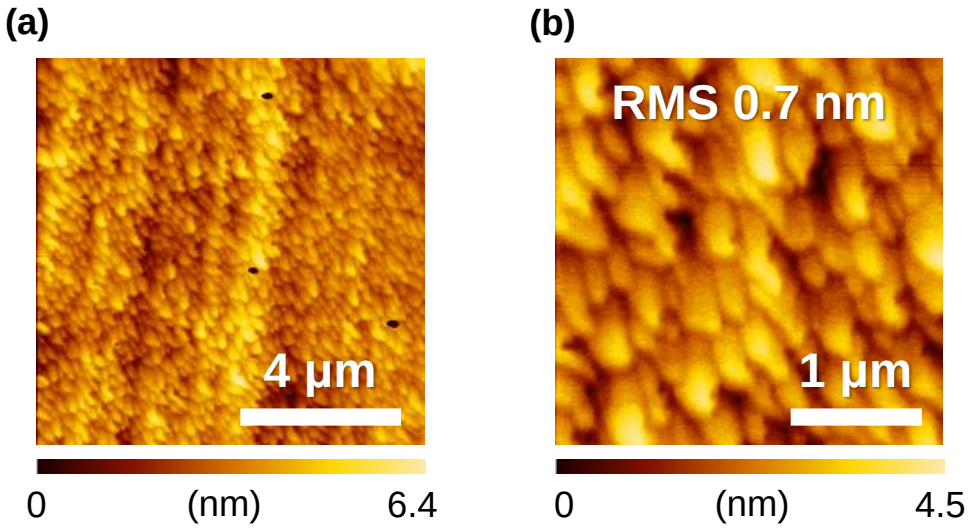

Figure 3.13: AFM images of an r-AlGaN film grown at 2 inch center position under the low pressure condition (AlN molar fraction: ∼0.75) in (a) 10 μm×10 μm area and (b) 3 μm×3 μm area.

suitable for the fabrication of UVC LEDs emitting at ∼230 nm is ∼0.88, as shown in Fig. 3.14, considering that the typical half width of at half maximum (FWHM) of emission spectra from QWs is about 10 nm. Therefore, we tried to fabricate r-AlGaN films with higher AlN molar fraction.

Toward AlN molar fraction of ∼0.83

We optimized growth conditions of AlGaN films with AlN molar fraction of ∼0.83 for LEDs of which wavelength is ∼240 nm next. Figure 3.15 shows NH_3 flow rate and TMA/(TMA+TMG) dependences of AFM images of r-plane AlGaN grown at fixed TMA flow rate, monitored growth temperature, and pressure (56.6 μmol/min, 1200 °C, and 38 Torr, respectively). AlN molar fractions estimated by the method described in Sec. 3.6.1 and/or XRD symmetric 2θ-ω scan of r-plane are also written in Fig. 3.15. Decrease in TMG flow rate keeping NH_3 flow rate at 156 mmol/min resulted in poor surface morphology. However, AlGaN films with AlN molar fraction of 0.83 with good surface morphology were achieved by decreasing NH_3 flow rate from 134 mmol/min to 22.4 mmol/min. The change in surface morphology by changing growth conditions will be discussed in Sec. 3.5.

Toward AlN molar fraction of ∼0.88

Finally growth conditions of AlGaN films with AlN molar fraction of ∼0.88 for LEDs of which wavelength is ∼230 nm were optimized. Figure 3.16 shows NH_3 flow rate and TMA/(TMA+TMG) dependences of AFM images of *r*-plane AlGaN grown at fixed TMA flow rate, monitored growth temperature, and pressure (56.6 µmol/min, 1200 °C, and 38 Torr, respectively). When TMA/(TMA+TMG) was 0.85 at 1200 °C, increasing NH_3 flow rate flattened surface to some extent at a first glance. However, the directions of streaks on samples grown under low NH_3 flow rate conditions at 1200 °C are the same as the directions of pit edges. In addition, the increase in NH_3 flow rate results in higher pit density in the case of *r*-AlN [60]. Therefore, we consider that increase in NH_3 flow rate leads to higher pit density and smaller pit size.

r-$Al_{0.88}Ga_{0.12}N$ films with smooth surfaces were not obtained under the growth conditions in Fig. 3.16. There are two routes in obtaining AlGaN films with higher AlN molar fractions. One is decrease in TMG flow rate, which is tried as described above and failed to obtain *r*-AlGaN with both of higher AlN molar fractions and smooth surfaces. The other is an increase in growth temperature. Increase in growth temperature might lead to lower pit density as shown in Sec. 3.3.2. Therefore, we tried an increased growth temperature. Figure 3.17 shows NH_3 flow rate and monitored growth temperature dependences of AFM images of those grown at fixed MO flow rate and pressure (TMA flow rate: 56.6 µmol/min, TMG flow rate: 14.1 µmol/min, pressure: 38 Torr). Increasing growth temperature from 1200 °C to 1250 °C resulted in a rough surface. However, decrease in NH_3 flow rate at 1250 °C led to lower pit density, and an Al(Ga)N film with good surface morphology was obtained at an NH_3 flow rate of 2.63 mmol/min. Decrease in NH_3 flow rate at 1250 °C also led to higher AlN molar fraction due to facilitated Ga evaporation. Therefore, increases in TMG flow rate to the condition where NH_3 flow rate is 2.63 mmol/min were explored next in order to decrease AlN molar fraction.

Figure 3.18 shows AFM images of *r*-AlGaN films grown at a fixed NH_3 flow rate (2.63 mmol/min). An $Al_{0.88}Ga_{0.12}N$ film was obtained by increasing TMG flow rate, but the surface morphology deteriorated. Therefore, TMA flow rate was decreased in order to improve surface morphology through the decrease in growth rate. The RMS of surface roughness of *r*-AlGaN films decreases with decreasing TMA flow rate, and is less than 1 nm when TMA flow rate decreased by one third. Interestingly, AlN molar fraction was almost unchanged by the decrease only in TMA flow rate, probably due to high evaporation of Ga adatoms. *r*-$Al_{0.88}Ga_{0.12}N$ films with smooth surfaces were obtained by the optimization of growth conditions.

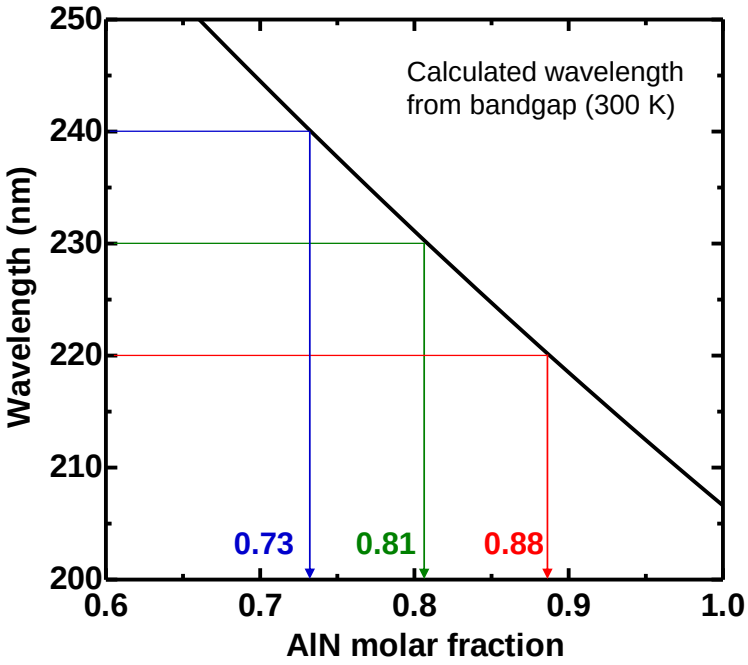

Figure 3.14: AlN molar fraction dependence of corresponding wavelength to bandgaps

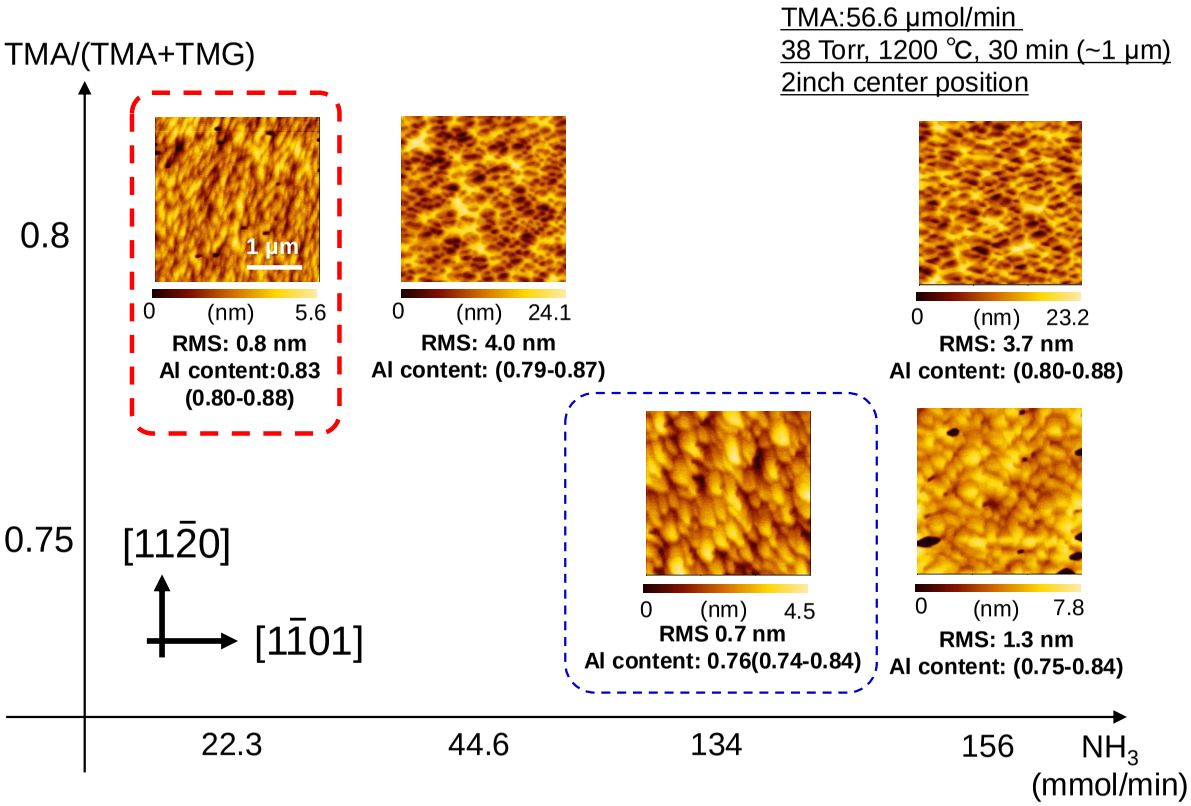

Figure 3.15: AFM images of r-AlGaN films grown at various TMA/(TMA+TMG) and NH_3 flow rate toward AlGaN films with AlN molar fraction of 0.83. AlN molar fractions were estimated by the method described in Sec. 3.6.1 and/or symmetric XRD 2θ-ω scan assuming fully relaxed (smaller AlN molar fraction in the parentheses) or fully coherent to ideal AlN (larger AlN molar fraction in the parentheses).

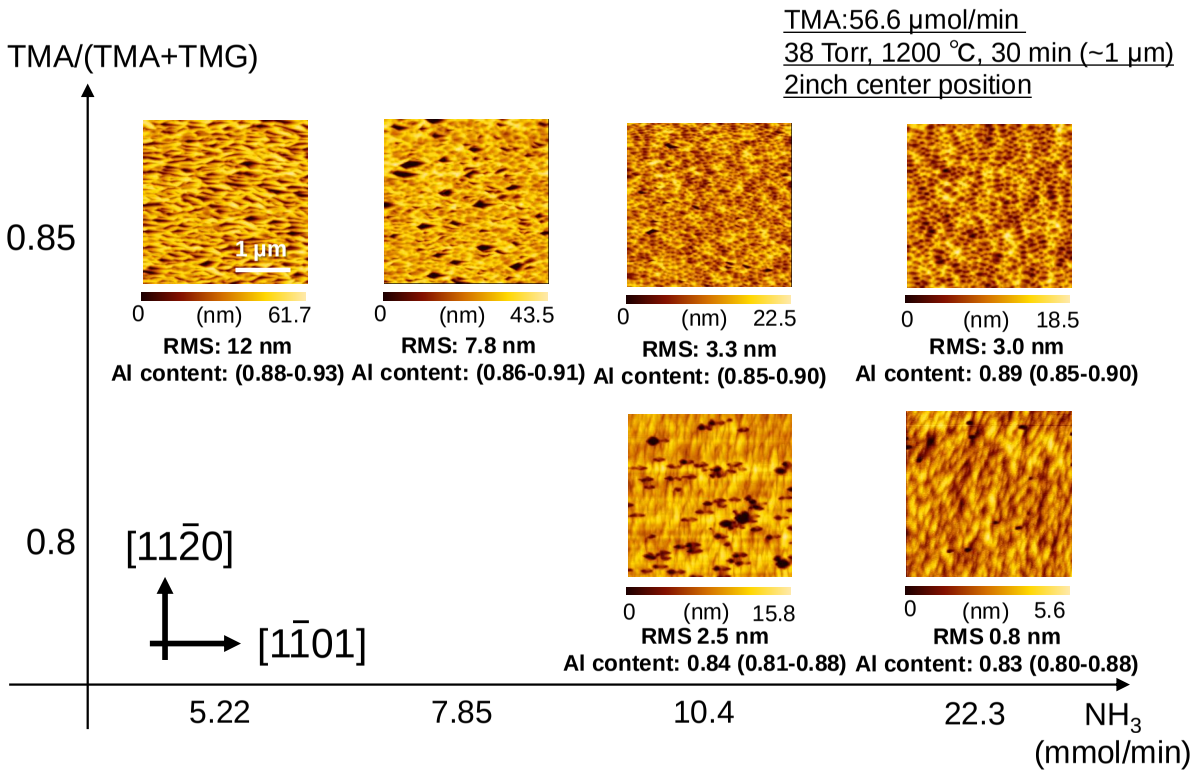

Figure 3.16: AFM images of r-AlGaN films grown at various TMA/(TMA+TMG) and NH_3 flow rate toward AlGaN films with AlN molar fraction of 0.88. AlN molar fraction were estimated by the method described in Sec. 3.6.1 and/or symmetric XRD 2θ-ω scan assuming fully relaxed (smaller AlN molar fraction in the parentheses) or fully coherent to ideal AlN (larger AlN molar fraction in the parentheses).

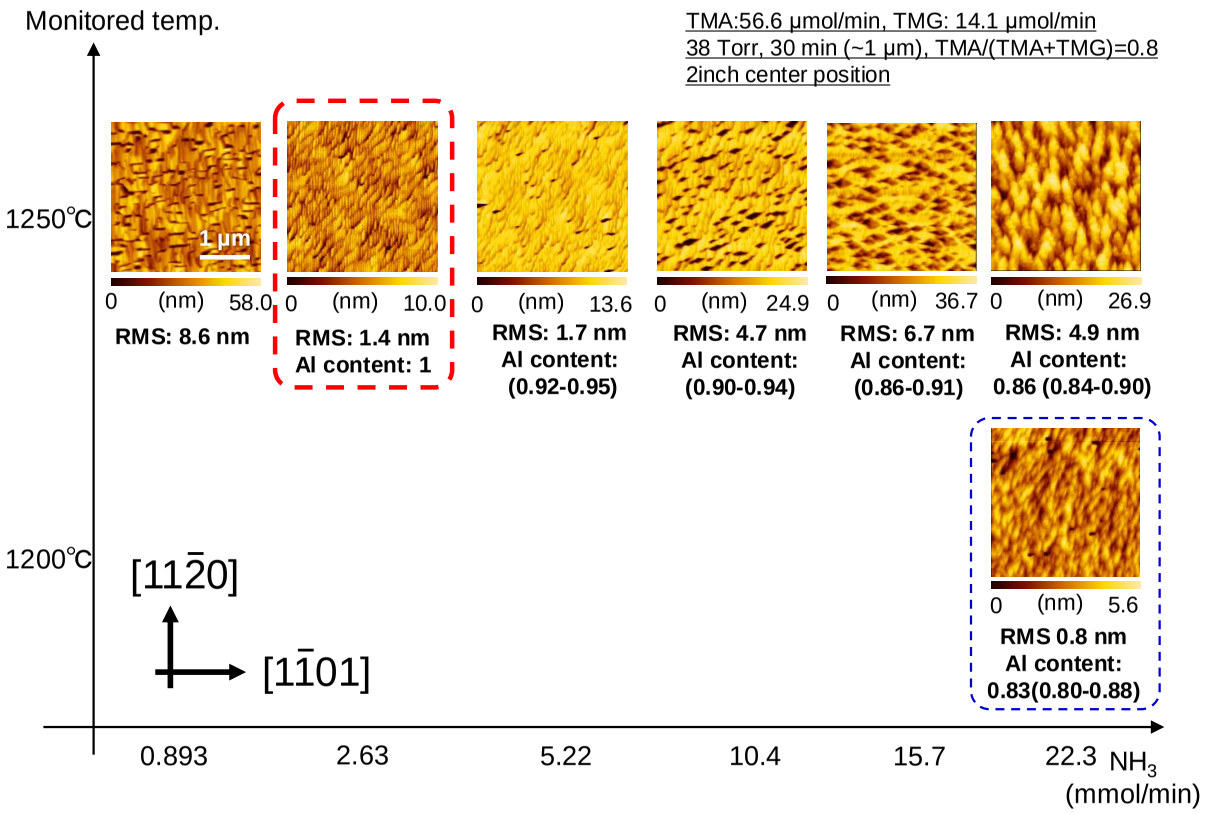

Figure 3.17: AFM images of r-AlGaN films grown at various NH_3 flow rate toward AlGaN films with AlN molar fraction of 0.88. AlN molar fractions were estimated by the method described in Sec. 3.6.1 and/or symmetric XRD 2θ-ω scan assuming fully relaxed (smaller AlN molar fraction in the parentheses) or fully coherent to ideal AlN (larger AlN molar fraction in the parentheses).

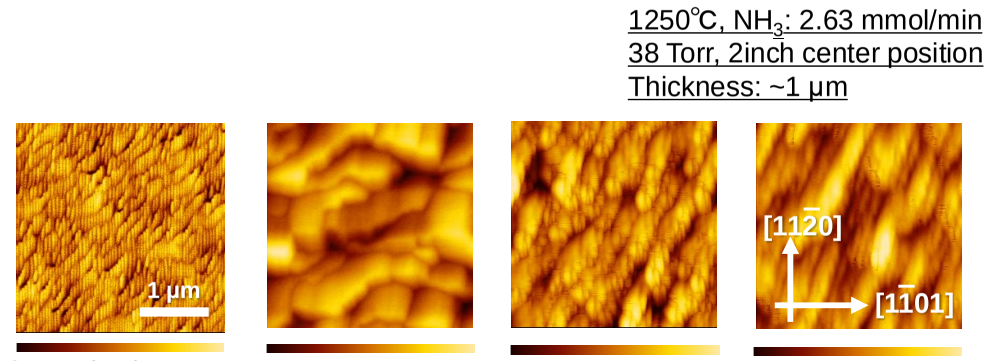

TMA[μmol/min]	56.6	56.6	28.3	18.8
TMG[μmol/min]	14.1	105	98	105
Growth time[min]	30	30	60	90

Figure 3.18: AFM images of r-AlGaN films grown at fixed NH_3 flow rate (2.63 mmol/min) toward AlGaN films with AlN molar fraction of 0.88. AlN molar fractions were estimated by the method described in Sec. 3.6.1 and/or symmetric XRD 2θ-ω scan assuming fully relaxed (smaller AlN molar fraction in the parentheses) or fully coherent to ideal AlN (larger AlN molar fraction in the parentheses).

3.5 Possible Explanation of the Change in Surface Morphology by Changing Growth Conditions

In this study, pit density is changed depending on growth conditions, such as NH_3 flow rate and growth temperature. In the previous study [60], an increase in NH_3 flow rate lead to slight increase in pit density but the mechanism of change in pit density is discussed only when growth pressure is changed. In this section, the mechanism of change in pit density by growth conditions is discussed.

Pit density is considered to be determined by the balance between pit formation and pit elimination. Firstly, NH_3 dependence of pit density is discussed. Figure 3.19 shows NH_3 flow rate dependence of pit density of r-AlN and $Al_{0.83}Ga_{0.17}N$. We consider that poor surface morphology of $Al_{0.83}Ga_{0.17}N$ films grown under high NH_3 flow rate conditions results from the formation of a lot of small pits considering the direction of each stripe. In both cases, an increase in NH_3 flow rate resulted in an increase in pit density. Therefore, pits are easily formed under high NH_3 flow rate conditions. On the other hand, in the case of r-$Al_{0.7}Ga_{0.3}N$, an increase in NH_3 flow rate is required for low pit density (Fig. 3.10). A possible mechanism for the NH_3 flow rate dependence of the pit density of r-AlGaN with lower AlN molar fraction is as follows. Generally, higher NH_3 flow rate reduces migration length of adatoms, resulting in a higher probability of the nucleus formation in pits. This nucleus will be three-dimensional one because of the existence of a kink at the bottom of pits. This three-dimensional nucleus will eventually bury pits as growth proceeds because of faster growth rate than that of two-dimensional one. This hypothesis is consistent with the previous report where higher pressure will eliminate pits [60], considering that higher pressure leads to a reduction in migration length of adatoms. In short, a higher NH_3 flow rate leads to pit elimination. By contrast, a lower NH_3 flow rate leads to pit expansion. Generally when multiple planes with different orientations are grown under non-equilibrium conditions such as MOVPE growth, faster planes will be eliminated as the growth goes. If migration length of adatoms is long, migration of adatoms from a pit region to a flat region will occur. As a result, growth rate of the pit region will be lower than that of a flat region, which will lead to larger pit size as growth proceeds.

Secondly, the AlN molar fraction dependence of pit density is discussed. Figure 3.20 shows a change in pit density of r-AlGaN films with AlN molar fraction (part of Fig. 3.15). Both of the r-AlGaM films in Fig. 3.20 were fabricated under the same NH_3 flow rate. As shown in Fig. 3.20, pits are

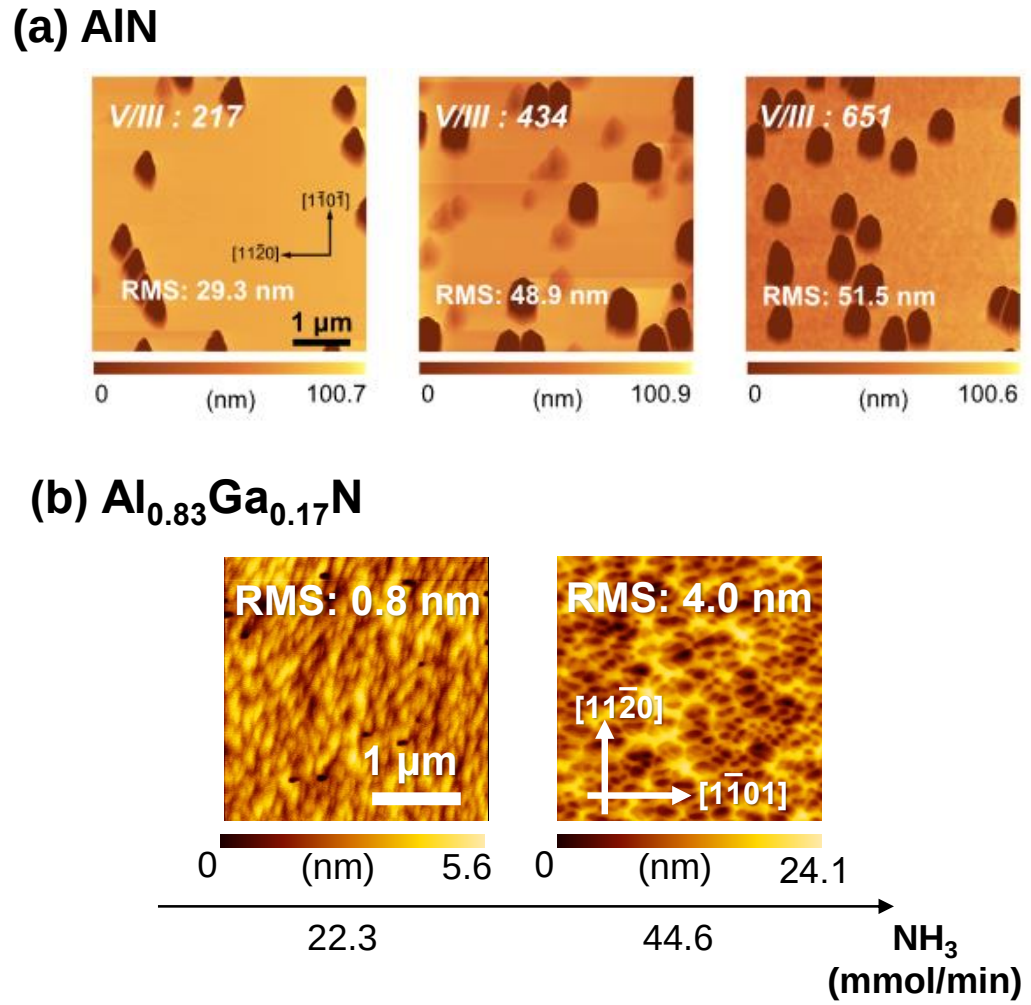

Figure 3.19: NH_3 flow rate dependences of pit density of (a) r-AlN [60] and (b) r-$Al_{0.83}Ga_{0.17}N$ films.

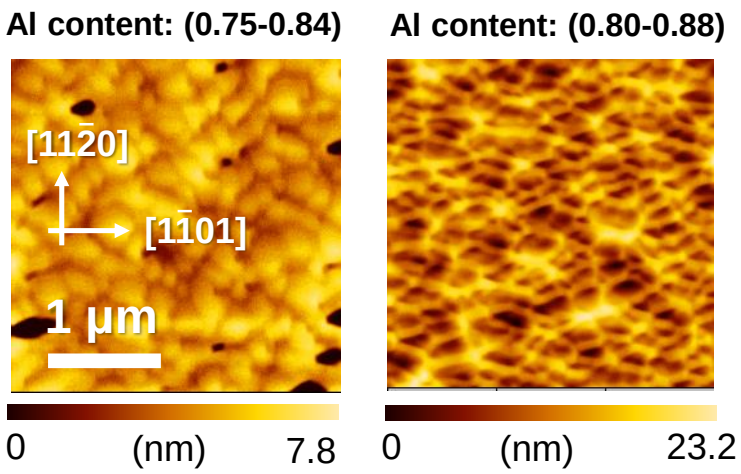

Figure 3.20: Change in pit density of r-AlGaN films with AlN molar fraction (part of Fig. 3.15).

difficult to form at lower AlN molar fraction. Next, the effect of AlN molar fraction on pit elimination is discussed. Generally, migration length of Al is shorter than that fo Ga. Therefore, a higher AlN molar fraction leads to shorter migration length and results in a higher probability of pit elimination.

Thirdly, the growth temperature dependence of pit density is discussed. Higher growth temperature was found to be favorable in terms of pit density in Sec. 3.3.2 and in Sec. 3.4. Generally, higher temperature leads to longer migration length. As discussed above, longer migration length results in lower probability of pit elimination, which contradicts to the fact that higher temperature reduces pit density. Therefore, pits are difficult to form under higher growth temperature conditions.

Finally, we summarize the effects of growth conditions and AlN molar fraction on pit formation and pit elimination. Figure 3.21 shows AFM images of obtained r-AlGaN films as functions of NH_3 flow rate and AlN molar fractions. Higher NH_3 flow rate and AlN molar fraction lead to a higher probability of pit formation (right upper side in Fig. 3.21 (a)). On the other hand, higher NH_3 flow rate and AlN molar fraction lead to a higher probability of pit elimination (right upper side in Fig. 3.21 (b)). As a result, optimal growth conditions exist due to the balance between pit formation and pit elimination and optimal growth conditions are lined on the diagonal line toward right bottom side in Fig. 3.21. In addition, a higher growth temperature is favorable in term of pit formation (unfavorable in terms of pit elimination).

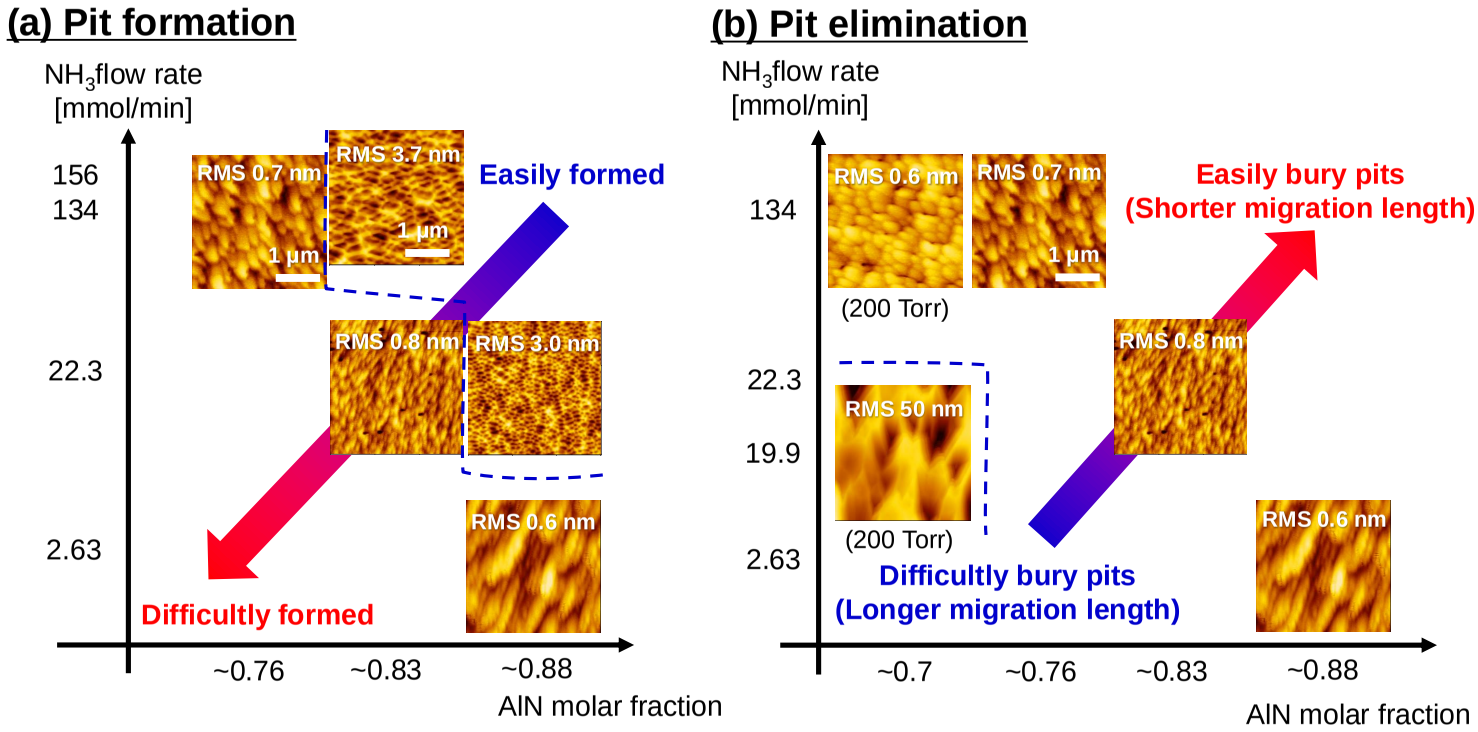

Figure 3.21: Effect of NH_3 flow rate and AlN molar fraction on (a) pit formation and (b) pit elimination.

3.6 Experimental Relaxation of Semipolar r-plane AlGaN Films

In heteroepitaxial growths, such as AlGaN on AlN, the epitaxial layer is coherently grown on the substrate (i.e. grown maintaining lattice constants of the epitaxial layer to those of the substrate) when the thickness of epitaxial layer is thin. As the growth proceeds, lattice constants of the epitaxial layer approach its ideal values. The degrees of the approach are expressed by relaxation degrees. Critical thickness of MQWs depends on relaxation degrees (i.e. lattice constants) of the AlGaN sublayer. Relaxation degrees of c-$Al_{0.7}Ga_{0.3}N$ thicker than ∼1 µm, which is necessary for a horizontal type of LEDs, were theoretically calculated to be nearly 100 % [59,66]. By contrast, relaxation degrees of ∼1 µm thick c-$Al_xGa_{1-x}N$ (x >0.6) are experimentally zero [102,119–122]. We successfully fabricated semipolar r-plane AlGaN films with smooth surfaces in Sec. 3.3.2 and Sec. 3.4. In this section, AlN molar fractions and relaxation degrees of r-plane AlGaN films are evaluated with X-ray diffraction (XRD) measurement.

3.6.1 Evaluation Method of AlN Molar Fraction and Relaxation Degree of r-plane AlGaN Films

Procedure

When the lattice mismatch between $(1\bar{1}02)$ r-plane $Al_xGa_{1-x}N$ and underlying unstrained AlN induces strain, $Al_xGa_{1-x}N$ is distorted as shown in Fig. 3.22 [69]. For strained $Al_xGa_{1-x}N$, an orthogonal coordinate (x', y', z') is defined, where x' is parallel to $[\bar{1}101]$, y' is parallel to $[\bar{1}\bar{1}20]$, and z' is perpendicular to the $(1\bar{1}02)$ plane. (That is, x' and y' are in the r-plane.) Strain elements $\varepsilon_{i'j'}$ $(i, j = x, y, z)$ can be calculated as

$$\varepsilon_{x'x'} = \frac{e^{\mathrm{s}} - e^{\mathrm{us}}}{e^{\mathrm{us}}}, \tag{3.1}$$

$$\varepsilon_{y'y'} = \frac{a^{\mathrm{s}}_{y'} - a^{\mathrm{us}}_{y'}}{a^{\mathrm{us}}_{y'}}, \tag{3.2}$$

$$\varepsilon_{z'z'} = \frac{d^{\mathrm{s}}_{(1\bar{1}02)} - d^{\mathrm{us}}_{(1\bar{1}02)}}{d^{\mathrm{us}}_{(1\bar{1}02)}}. \tag{3.3}$$

The superscripts "s" and "us" represent "strained" and "unstrained", respectively. d is the interplanar spacing of the crystallographic plane denoted as a subscript. Figure 3.22 depicts the definitions of e and $a_{y'}$. e represents the diagonal length of one hexagonal lattice viewed along the y' axis. $a_{y'}$

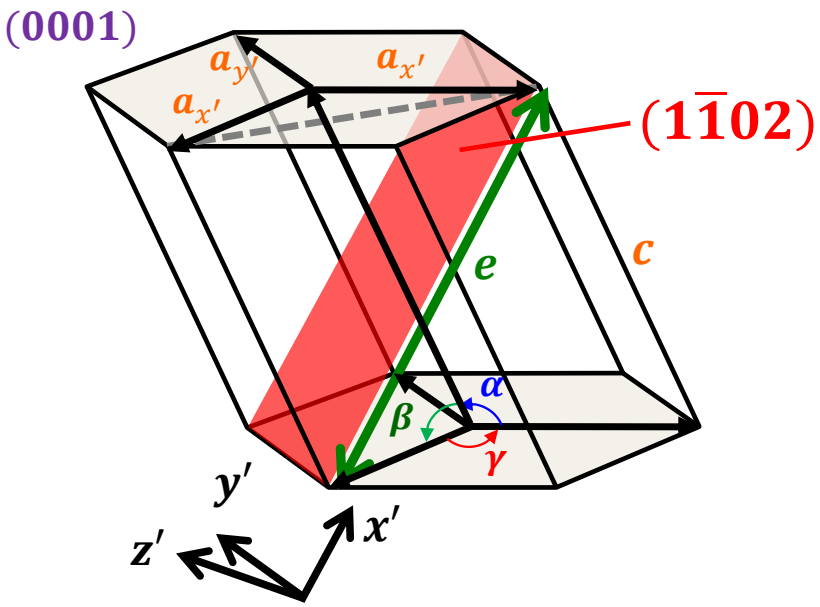

Figure 3.22: Schematics of distorted r-$Al_xGa_{1-x}N$ on AlN and coordinate system. α is the angle between $[\bar{1}2\bar{1}0]$ and $[0001]$, β is the angle between $[0001]$ and $[2\bar{1}\bar{1}0]$, γ is the angle between $[2\bar{1}\bar{1}0]$ and $[\bar{1}2\bar{1}0]$.

is an a lattice parameter along the y' axis. $a_{y'}$ equals the AlN a-lattice parameter when coherently grown. This is equal to the unstrained $Al_xGa_{1-x}N$ a-lattice parameter when completely relaxed. Once $\varepsilon_{x'x'}$, $\varepsilon_{y'y'}$, and $\varepsilon_{z'z'}$ are determined experimentally, the Al composition x can be obtained by finding x that satisfies

$$\varepsilon_{z'z'} = \frac{(S'_{13}S'_{22} - S'_{23}S'_{12})\varepsilon_{x'x'} + (S'_{23}S'_{11} - S'_{13}S'_{12})\varepsilon_{y'y'}}{S'_{11}S'_{22} - S'^2_{12}}, \tag{3.4}$$

where S'_{kl}s are elastic compliance constants defined for the (x', y', z') coordinate. The rotation method of S_{kl} to S'_{kl} is described later. This general equation is derived by assuming traction-free surfaces (namely, $\sigma_{z'z'} = 0$, where σ is a strain tensor), and holds for distorted hexagonal crystals.

Definition of Lattice Relaxtion Degrees

The lattice relaxation degrees along the x' and y' axes, which are defined as $r_{x'}$ and $r_{y'}$, respectively, are expressed as

$$e^{\mathrm{s}} = r_{x'}e^{\mathrm{us}} + (1 - r_{x'})e^{\mathrm{sub}}, \tag{3.5}$$

$$a^{\mathrm{s}}_{y'} = r_{x'}a^{\mathrm{us}}_{y'} + (1 - r_{y'})a^{\mathrm{sub}}_{y'}, \tag{3.6}$$

where the superscript "sub" represents the substrate.

Formula of Elastic Compliance Constants Defined for (x', y', z') Coordinate

Formula of elastic compliance constants used in this study are as follows [123],

$$S'_{11} = S_{11}\cos^4\theta + S_{33}\sin^4\theta + \frac{2S_{13}+S_{44}}{4}\sin^2 2\theta, \tag{3.7}$$

$$S'_{12} = S_{12}\cos^2\theta + S_{13}\sin^2\theta, \tag{3.8}$$

$$S'_{13} = S_{13}(\cos^4\theta + \sin^4\theta) + \frac{S_{11}+S_{33}-S_{44}}{4}\sin^2 2\theta, \tag{3.9}$$

$$S'_{22} = S_{11}, \tag{3.10}$$

$$S'_{23} = S_{12}\sin^2\theta + S_{13}\cos^2\theta, \tag{3.11}$$

$$S_{11} = \frac{C_{11}C_{33}-C_{13}^2}{\Delta}, \tag{3.12}$$

$$S_{12} = \frac{C_{13}^2-C_{12}C_{33}}{\Delta}, \tag{3.13}$$

$$S_{13} = \frac{(C_{12}-C_{11})C_{13}}{\Delta}, \tag{3.14}$$

$$S_{33} = \frac{C_{11}^2-C_{12}^2}{\Delta}, \tag{3.15}$$

$$S_{44} = \frac{1}{C_{44}}, \tag{3.16}$$

$$\Delta = (C_{11}-C_{12})\{(C_{11}+C_{12})C_{33}-2C_{13}^2\}, \tag{3.17}$$

where, C_{ij} represents elastic stiffness constants. S_{ij} of AlGaN is calculated by linear interpolartion of C_{ij}.

Calculation Method of Each Lattice Constant

The calculation method of lattice constants used in this study is essentially the same as a paper [124] but we performed 2θ-ω scans for only four planes, symmetric r-plane, asymmetric $(1\bar{1}03)$, $(1\bar{1}05)$, and $(1\bar{2}12)$ for simplicity. The glancing incidence and glancing exit geometry were employed for the asymmetric planes, and the two peak values of 2θ were averaged for calculations of interplanar distances in order to improve accuracy. Interplanar distance of (hkl) plane (in 3 digit notation) is expressed as (Eq. (5b) in [124]),

$$\frac{1}{d^2_{(hkl)}} = \frac{4}{3}\frac{h^2+k^2+hk}{a^2_{x'}} + \frac{8h^2+8k^2+20hk}{3\sqrt{3}a^2_{x'}}\delta_\gamma + \frac{4(k-h)l}{3a_{x'}c}\delta_\alpha + \frac{l^2}{c^2}, \tag{3.18}$$

Table 3.1: Experimentally obtained AlN molar fraction and relaxation degree of r-AlGaN films (thickness $\sim$ 1 µm).

AlN molar fraction	$r_{x'}$	$r_{y'}$
0.76	1.1	0.51
0.83	1.1	0.16
0.88	1.1	0.45

where $a_{x'}$ is a lattice parameters along $[1\bar{2}10]$ and $[\bar{2}110]$, $\delta_\alpha = \alpha - 90°$, and $\delta_\gamma = \gamma - 90°$. $a_{x'}$, c, δ_α, and δ_γ can be estimated by measuring linearly independent four $d_{(hkl)}$s.

$a_{y'}$ and e can be calculated using the following equation (modification of Equation (8) in [124]) for distance along arbitrary direction $[uvw]$, $L_{[uvw]}$,

$$\begin{aligned} L^2_{[uvw]} =& (ua_{x'})^2 + (va_{x'})^2 + (wc)^2 \\ &+ 2vwa_{x'}c\cos\beta + 2uva^2_{x'}\cos\gamma + 2wuca_{x'}\cos\alpha, \end{aligned} \tag{3.19}$$

where $\beta = 90° + \delta_\beta$, $\delta_\beta = -\delta_\alpha$, $a_{y'} = L_{[110]}$ and $e = L_{[1\bar{1}\bar{1}]}$.

3.6.2 Experimental Evaluation of Relaxation Degree

Calculated AlN molar fractions and relaxation degrees of the optimal r-AlGaN films obtained in Sec. 3.4 are shown in Tab. 3.1. When calculating relaxation degrees, it is assumed that the lattice constants of r-AlN substrates are the ideal ones (a=0.3112 nm, c=0.4982 nm [125]). From Tab. 3.1, anisotropic relaxation is confirmed and r-plane AlGaN films are easy to relax along x' axis. (The reason why $r_{x'}$ is slightly larger than 1 may be due to inaccuracy of the estimated lattice constants.) Semipolar $In_xGa_{1-x}N$ films on GaN also show anisotropy in the lattice relaxation [69], suggesting that lattice relaxation is strongly related to the crystal anisotropy of nitride semiconductors. Figure 3.23 shows the calculation result of lattice relaxation process of r-$Al_{0.7}Ga_{0.3}N$ [59] and the experimental result of the relaxation degree of r-$Al_{0.76}Ga_{0.24}N$ obtained in this study. The experimental relaxation degree along x' direction is nearly the same as the theoretical one, but that along y' direction is far from the theoretical one. The reason for this discrepancy is currently unclear, but this might be related to the slow relaxation process of c-AlGaN [102, 119–122] because y' direction is an in-plane direction of c-plane.

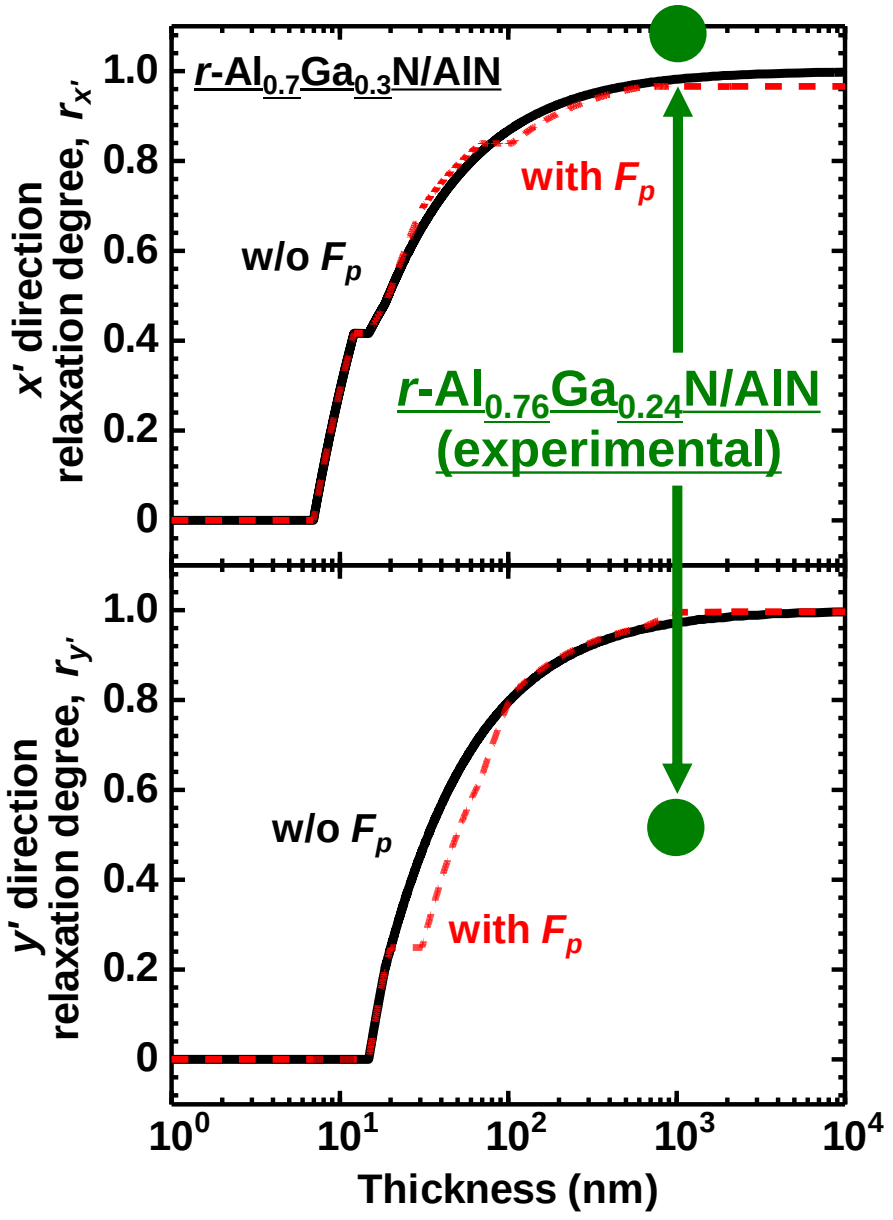

Figure 3.23: Experimentally obtained relaxation degrees of an r-$Al_{0.76}Ga_{0.24}N$ film plotted on calculated relaxation degrees of r-$Al_{0.7}Ga_{0.3}N$. The calculation result is taken from [59].

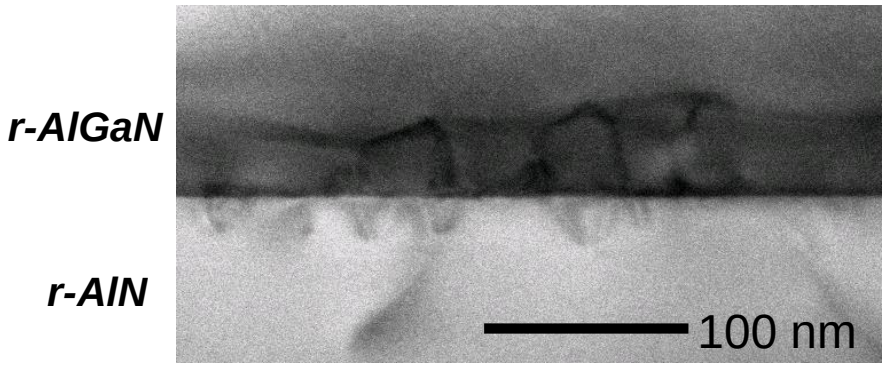

Figure 3.24: Cross-sectional STEM image of lattice-relaxed $Al_xGa_{1-x}N$ on r-AlN viewed along the $[1\bar{1}01]$ direction.

3.6.3 Effect of Lattice Relaxation of r-AlGaN Films on QWs

Our result shows that r-AlGaN films grown on r-AlN relax more easily than those on c-AlN. Hence, it is possible that new threading dislocations will be formed when AlGaN is relaxed and they will deteriorate the optical characteristics of subsequent QWs. To investigate the distribution of dislocations in r-plane AlGaN on AlN, cross-sectional STEM was performed. The sample for STEM is identical to r-AlGaN fabricated in Sec. 3.3.2. Figure 3.24 shows a STEM image of an AlGaN/AlN interface viewed along the $[1\bar{1}01]$ direction. Dislocations originating from the stress relaxation are confined in the vicinity of the interface between $Al_xGa_{1-x}N$ and AlN. Similar phenomena have been observed in $(11\bar{2}2)$ InGaN/GaN interfaces and $(11\bar{2}2)$ AlGaN/GaN interfaces [69, 126, 127]. Therefore, the effect of misfit dislocations on QWs fabricated on r-plane AlGaN films is small.

3.7 Summary

In this chapter, growth conditions of r-plane AlGaN films with smooth surfaces were established. Growth conditions of r-AlN, r-$Al_{0.7}Ga_{0.3}N$, and r-GaN were established at 200 Torr. Growth conditions of r-AlGaN films with AlN molar fractions of 0.76, 0.83, 0.88 were also established even at low pressure of 38 Torr. Then, the mechanism of change in pit density by growth conditions was discussed. Pit density is determined by the balance between pit formation and pit elimination. Low NH_3 flow rate, high growth temperature, and low AlN molar fraction conditions are favorable in terms of pit

formation. However, in terms of pit elimination, a shorter migration length of adatoms is favorable, i.e. high NH_3 flow rate, high pressure, low growth temperature, and high AlN molar fraction. As a result, optimal growth conditions exist. Relaxation degrees of the fabricated r-AlGaN films were also investigated. r-AlGaN films were easily relaxed along the $[1\bar{1}01]$ direction, as expected from the theoretical calculation of relaxation process. However, they were hardly relaxed along the $[11\bar{2}0]$ direction compared with the $[1\bar{1}01]$ direction. This might be related to nearly no relaxation observed on c-AlGaN films. Dislocations originating from the stress relaxation are confined in the vicinity of the interface between AlGaN and AlN. Therefore, the effect of misfit dislocations on QWs fabricated on r-plane AlGaN films is small.

Chapter 4

Optical Characteristics of Semipolar r-plane QWs

4.1 Introduction

QWs are the centerpiece of LEDs. Among three components of EQEs, that is IQEs, LEEs, and CIEs, information on IQEs and LEEs can be obtained through PL measurements. In this chapter, optical characteristics of fabricated r-plane AlGaN-based QWs are experimentally investigated. Selective excitation of the well layers is necessary for accurate estimation of IQEs [128–130]. Therefore, in the first half of this chapter, AlGaN/AlN QWs are investigated due to the limitation of the available laser system. For LEDs, AlGaN/AlGaN QWs are necessary to achieve high CIEs. Therefore, in the second half of this chapter, AlGaN/AlGaN QWs are investigated.

4.2 TIPL and TRPL Analysis of Semipolar r-AlGaN/AlN QWs

AlGaN/AlN QWs were fabricated by the MOVPE method on c-AlN substrates, c-AlN/sapphire templates, and r-AlN substrates under various growth conditions. In this section, IQEs of AlGaN/AlN QWs emitting in the far-UVC region are discussed using time integrated photoluminescence (TIPL) and time resolved PL (TRPL).

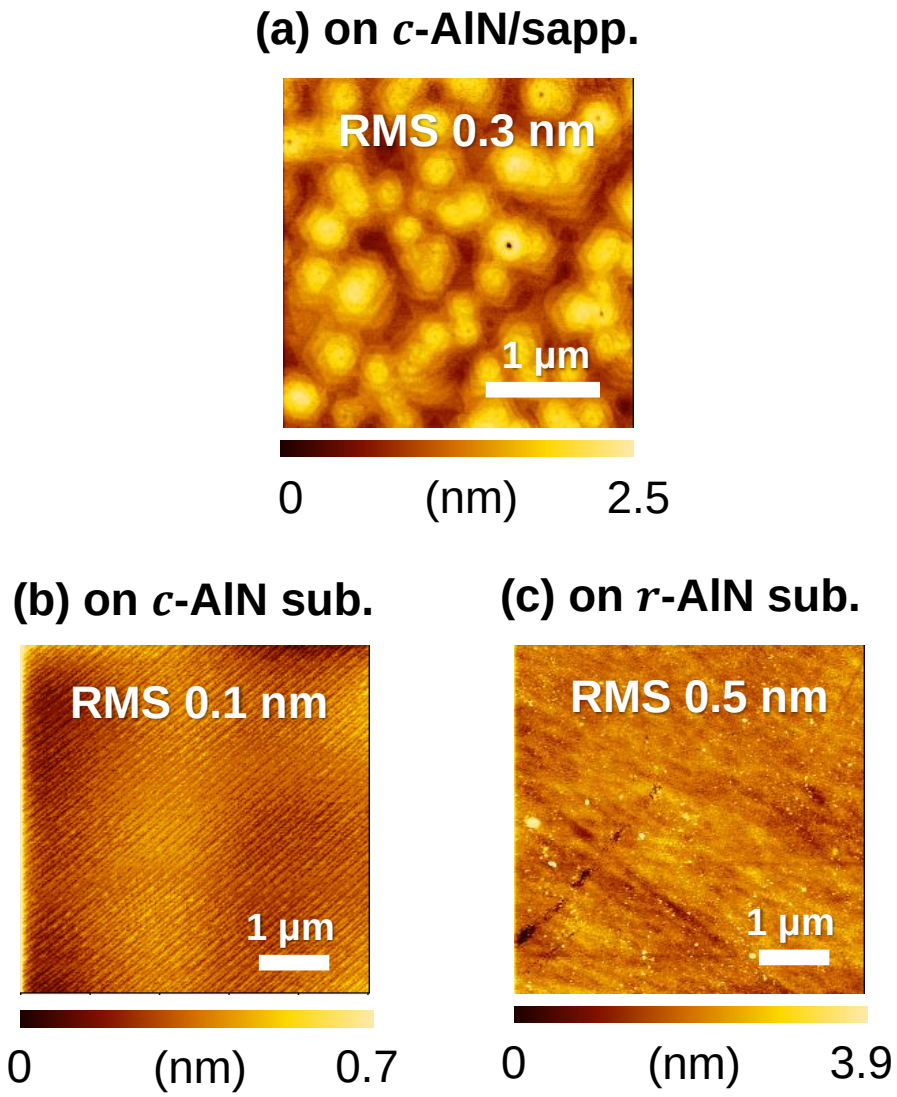

Figure 4.1: Typical AFM images of AlGaN/AlN QWs grown on (a) *c*-AlN/sapphire templates, (b) *c*-AlN substrates, and (c) *r*-AlN substrates.

4.2.1 Samples

AlGaN/AlN QWs were fabricated on c- and r-AlN substrates by the previous MOVPE machine [58–60] and on c-AlN/sapp. templates by the current MOVPE machine. The growth pressures of QWs on c-AlN substrates, c-AlN/sapp. templates, and r-AlN substrates are 38 Torr, 200 Torr, and 500 Torr, respectively. Figure 4.1 shows typical AFM images of AlGaN/AlN QWs grown on c-AlN/sapp. templates, c-AlN substrates, and r-AlN substrates. The RMSs of surface roughness are below 1 nm and sufficiently low.

4.2.2 Measurement System

For the TIPL and TRPL measurements, the 4th harmonics of a ps-pulsed Ti:sapphire laser was used as an excitation source. The repetition rate was 80 MHz, the pulse width was ∼2 ps, and the spot size was ∼100 µm×500 µm. The excitation wavelength was 213 nm, which enabled selective excitation of the well layers because AlN was used as barrier layers. This is necessary for accurate estimation of IQEs [128–130]. TIPL spectra were acquired by a 50 cm monochromator and a charge-coupled device. TRPL signals were acquired by a 30 cm monochromator and a streak camera.

4.2.3 Comparison of Emission Intensity between c- and r-AlGaN/AlN QWs

Figure 4.2 shows spectrally and temporally integrated RT PL intensities of the fabricated QWs excited with a pulse energy fluence of 25 nJ/cm^2, plotted as functions of the emission peak energy. The PL intensities of the c-QWs drastically decreased at higher peak energies. However, this tendency was suppressed in the r-QWs. As a result, the PL intensities of the r-QWs were ∼14 times higher than those of the c-QWs, especially in the far-UVC region. Here, the stronger emission of the r-QWs was not due to the difference in the dislocation densities of the substrates because the c-QWs on c-AlN substrates (dislocation density: $\sim 10^6$ cm^{-2}) show weaker emission than the r-QWs on r-AlN substrates (dislocation density: $\sim 10^7$–10^8 cm^{-2}). In general, 1 nm-thick c-QWs exhibit stronger emission per unit thickness than 2 nm-thick c-QWs because of the 1-nm-QWs' shorter radiative lifetimes and enhanced TE emission. This tendency is confirmed in Fig. 4.2. Nevertheless, r-QWs with a well width of 1—2 nm emit PL more strongly than thinner c-QWs (∼1 nm), thereby indicating the superiority of r-QWs to c-QWs as far-UVC emitters.

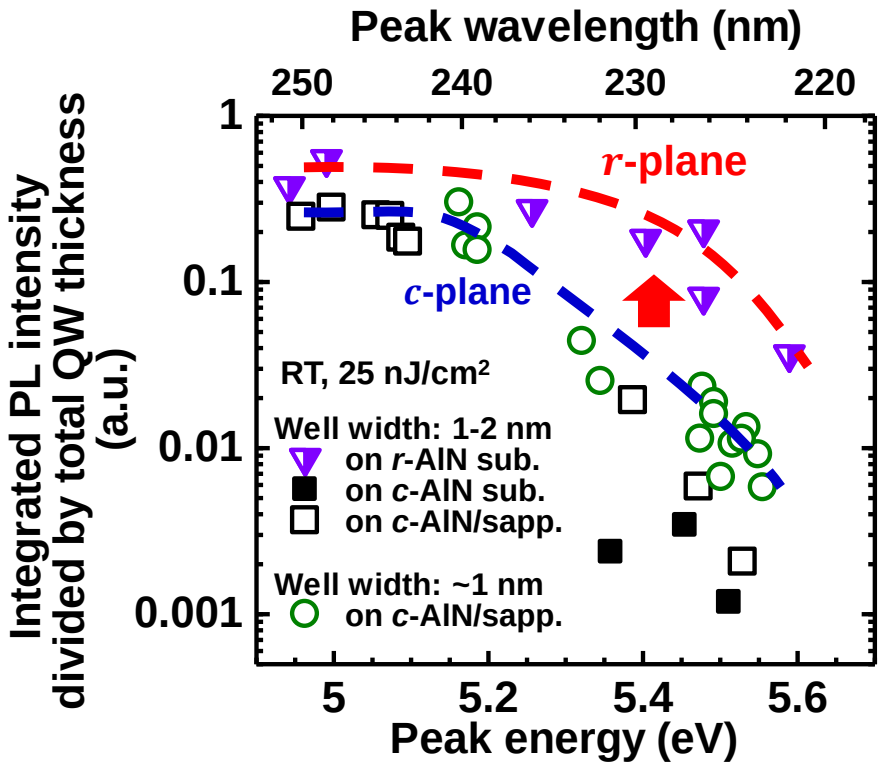

Figure 4.2: Peak energy dependences of integrated PL intensities of c- and r-AlGaN/AlN QWs at RT. The intensities are divided by the total well width to compensate differences in well width and periods.

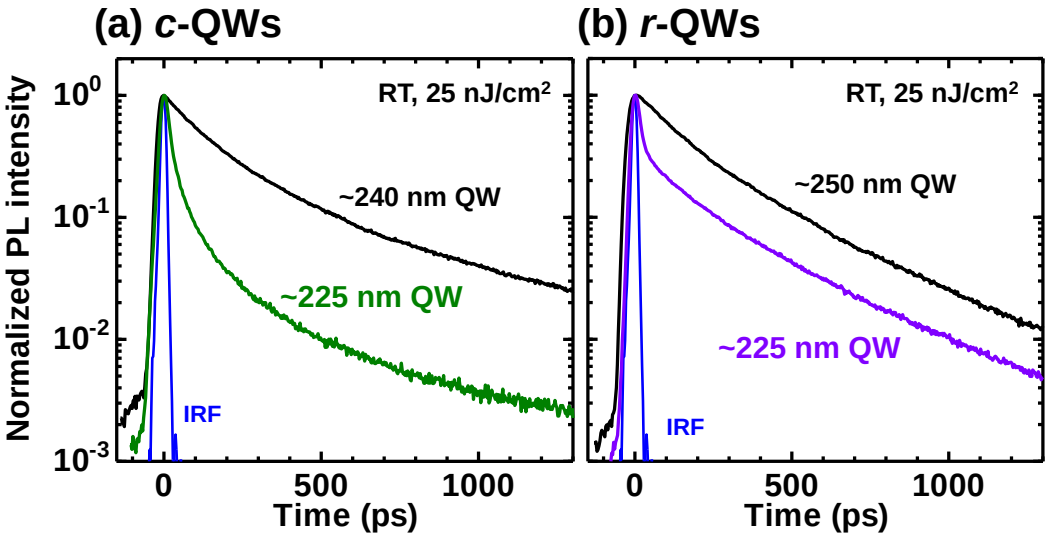

Figure 4.3: Comparison of TRPL decay curves of AlGaN/AlN QWs at RT with emission wavelengths of ∼225 nm and longer wavelengths (*c*-QWs: ∼ 240 nm, *r*-QWs: ∼ 250 nm). Well widths of *c*-QWs are 1 nm, and those of ∼250-nm and ∼225-nm *r*-QWs are 1.1 nm and 1.5 nm respectively.

4.2.4 Appearance of Faster Decay Component in AlGaN/AlN QWs Emitting in the Far-UVC Region

To identify the causes of the observed tendencies in Fig. 4.2, Fig. 4.3 compares the TRPL decay curves of QWs emitting at a wavelength of ∼225 nm or longer (*c*-QW: ∼240 nm, *r*-QW: ∼250 nm) at RT. The ranges for wavelength integration are the peak wavelength ±2 nm. For both the *c*- and *r*-QWs, a faster decay component emerges and dominates their decay curves at the shorter wavelength. We do not consider that the faster decay components result from carrier relaxation to lower energy states because such relaxation does not result in non-single exponential decay according to the model of Gourdon and Lavallard. [131] Rather, the emergence of a faster decay component might be related to low IQEs in the far-UVC region because the IQEs (*i.e.*, $\tau_{\mathrm{r}}^{-1}/(\tau_{\mathrm{r}}^{-1}+\tau_{\mathrm{nr}}^{-1})$, where τ_{r} is the radiative lifetime and τ_{nr} is the nonradiative lifetime), might be low when the nonradiative lifetimes are short.

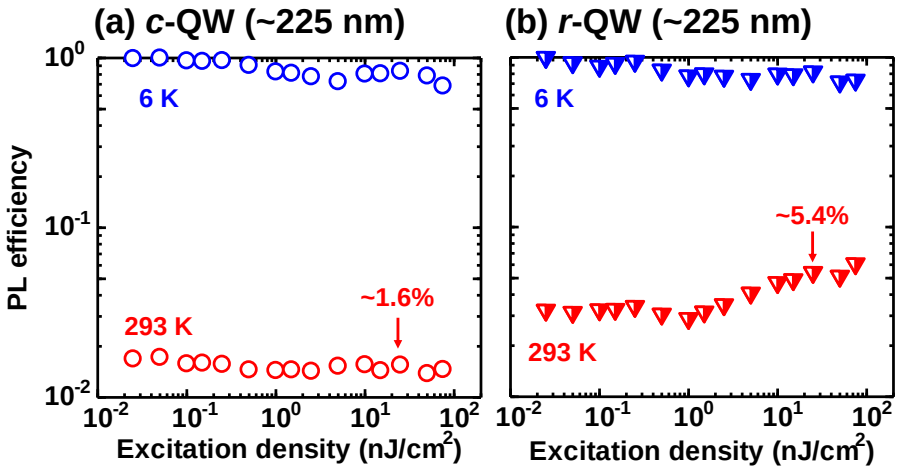

Figure 4.4: Normalized excitation-density-dependent PL efficiencies of (a) c-AlGaN/AlN (1 nm/5 nm) three-period QW and (b) r-AlGaN/AlN (1.5 nm/17 nm) five-period QW. Both QWs emit at ∼225 nm.

4.2.5 Estimation of IQEs of AlGaN/AlN QWs Emitting in the Far-UVC Region

We estimated the IQEs of c- and r-QWs emitting at ∼225 nm on the basis of a combination of excitation-power and temperature-dependent PL. [128,132] Figure 4.4 shows PL efficiencies normalized by the maximum PL efficiency at 6 K. Here, the PL efficiencies are defined as the spectrally and temporally integrated PL intensities divided by the excitation densities. The normalized PL efficiencies are regarded as IQEs. The IQEs of the c-QWs (well width: 1 nm) at RT are ∼1.6 % and nearly independent of the excitation density. The IQEs of the r-QWs (well width: 1.5 nm) at RT are higher than those of the c-QWs and increase with increasing excitation density when the excitation density is greater than ∼1 nJ/cm^2. The r-QWs show an IQE of ∼5.4 % at an excitation density of 25 nJ/cm^2.

IQEs of the QWs with longer wavelengths shown in Fig. 4.3 were also measured similarly. Figure 4.5 shows peak energy dependences of integrated PL intensities (I_{PL}) divided by total well width (D_{well}) and IQEs (η_{IQE}), which are proportional to LEE. LEEs have nearly no peak energy dependence in this wavelength range when focused on each plane. This means that the most dominant factor for peak energy dependences in integrated PL intensities shown in Fig. 4.2 is the change in IQEs at least with regard to r-QWs and 1-nm-thick c-QWs. Therefore, IQEs will be discussed in the latter sections. Higher LEEs of r-AlGaN/AlN QWs than c-AlGaN/AlN QWs (well

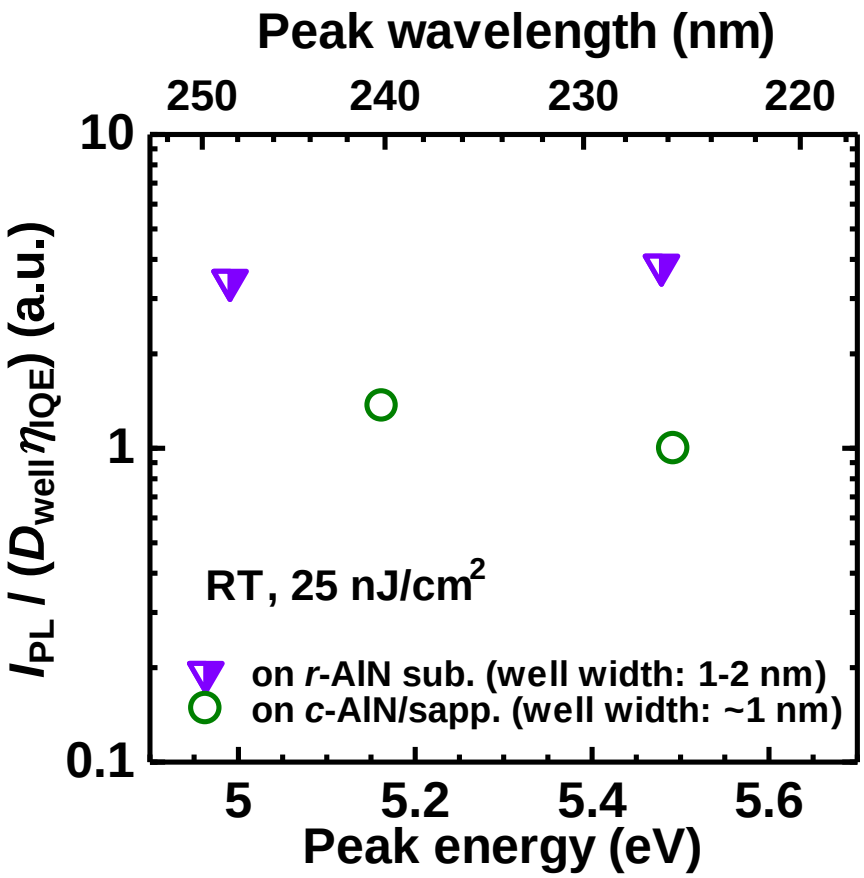

Figure 4.5: Peak energy dependences of integrated PL intensities (I_{PL}) divided by total well width (D_{well}) and IQEs (η_{IQE}) of c- and r-AlGaN/AlN QWs at RT. Well widths of c-QWs are 1 nm, and those of ∼250-nm and ∼225-nm r-QWs are 1.1 nm and 1.5 nm, respectively.

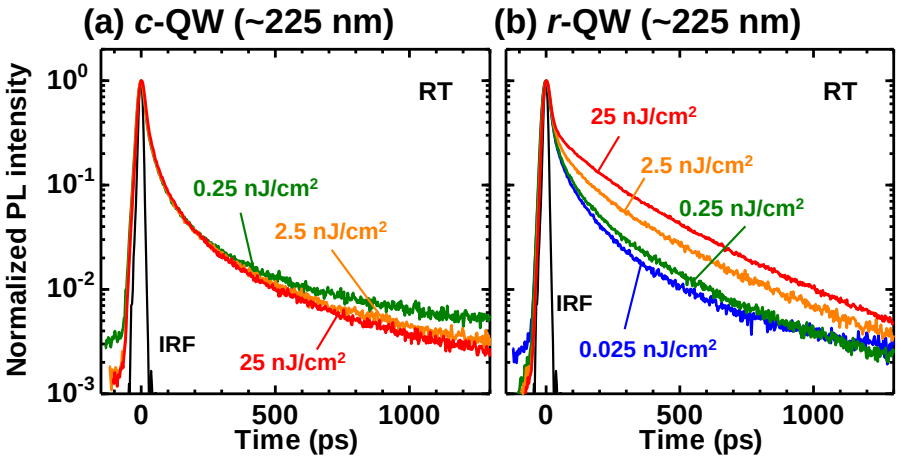

Figure 4.6: Excitation density dependences of TRPL decay curves of (a) c-QW and (b) r-QW. IRF represents the instrument response function.

Table 4.1: Fitting results for TRPL decays with an excitation density of 25 nJ/cm^2.

c-QWs	fast	IM	slow
τ_i (ps)	21	100	420
I_i (normalized)	0.89	0.098	0.015
$I_i\tau_i$ (normalized)	0.54	0.28	0.18
r-QWs	fast	IM	slow
τ_i (ps)	16	140	350
I_i (normalized)	0.80	0.11	0.09
$I_i\tau_i$ (normalized)	0.22	0.27	0.51

width: 1 nm) are a superiority of the use of r-plane.

4.2.6 TRPL Measurement

To clarify the reasons for the higher IQEs of the r-QWs and the different tendencies in the excitation power dependences of IQEs between the c- and r-QWs, we carried out TRPL measurements with various excitation densities at RT. Figure 4.6 shows the acquired TRPL decay curves. The TRPL decay curves of the c-QWs are nearly unchanged with increasing excitation density. By contrast, the TRPL decay curves of the r-QWs are approximately the same as those of the c-QWs at low excitation densities but change remarkably with increasing excitation density.

Within our experiences, the decay curves recorded for QWs emitting at

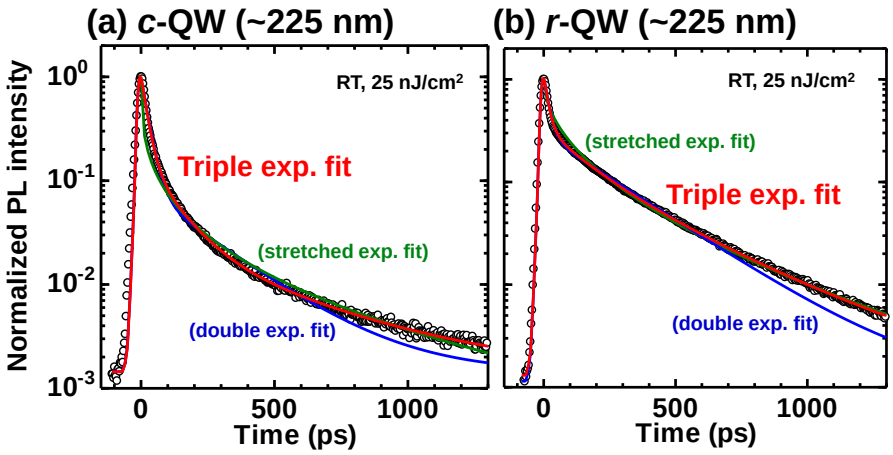

Figure 4.7: Fitting examples of TRPL decay curves of (a) c-QW and (b) r-QW.

~240 nm or longer (*e.g.*, Fig. 4.3) can be fitted with a double-exponential function. [133] However, double-exponential fitting cannot reproduce the decay curves of the QWs emitting at ~225 nm (Fig. 4.7), likely because of the increased number of independent recombination channels in the far-UVC emitters; this interpretation is consistent with the emergence of the fast decay component in the PL decay (Fig. 4.3). We examined a triple exponential fit and a stretched exponential fit and confirmed that the former provided a better fitting result (Fig. 4.7). Therefore, in the present study, PL decay is analyzed with triple exponential functions. Notably, the number of independent events is not strictly three but could be greater than three. A possible origin of the multiple exponential components is the existence of multiple independent regions where nonradiative recombination lifetimes differ as a result of the spatial distributions of potential fluctuation and nonradiative recombination centers. [133, 134]

Table 4.1 shows the fitting results at an excitation density of 25 nJ/cm^2. Here, the fitted equation is $I(t) = \sum_i I_i \exp(-t/\tau_i)$, where i = fast, intermediate(IM), slow; I_i is the coefficient; and τ_i is the lifetime. Because $\int_0^\infty I_i \exp(-t/\tau_i)\mathrm{d}t = I_i\tau_i$, $I_i\tau_i$ represents the contribution of each emission component to the total time-integrated PL intensity. Parameters I_i and $I_i\tau_i$ are normalized so that $\sum_i I_i = 1$ and $\sum_i I_i\tau_i = 1$. Although I_{fast} is dominant among the exponential components, $I_{\mathrm{IM}}\tau_{\mathrm{IM}}$ and $I_{\mathrm{slow}}\tau_{\mathrm{slow}}$ cannot be ignored in comparison with $I_{\mathrm{fast}}\tau_{\mathrm{fast}}$ because τ_{IM} and τ_{slow} are much longer than τ_{fast}.

4.2.7 Fitting and Model for Analysis

For further analyses, we considered three rate equations of exciton for the three decay components (i = fast, IM, slow):

$$\frac{\mathrm{d}n_i}{\mathrm{d}t} = -\left(\frac{1}{\tau_{\mathrm{r},i}} + \frac{1}{\tau_{\mathrm{nr},i}}\right) n_i, \tag{4.1}$$

where n_i is the volume density of excitons. Notably, higher-order terms of the carrier density are not included in Eq. (4.1), unlike the typical ABC model, because higher-order terms cannot well reproduce the decay curves experimentally obtained under various excitation energy densities. In addition, the maximum initial carrier density is as low as $\sim 2\times10^{15}$ cm^{-3}, which does not cause many-body effects. Other assumptions are that the radiative lifetimes in each region are the same ($= \tau_{\mathrm{r}}$) and that the initial exciton density is uniform ($= n_0$) for the three decay components. In this situation, the temporal evolution of the emitted photon number $N_{\mathrm{p}}(t)$ and the consequent PL decay $I(t)$ are expressed as

$$I(t) \propto N_{\mathrm{p}}(t) \propto \frac{n_0}{\tau_{\mathrm{r}}} \sum_i V_i \exp\left(-\frac{t}{\tau_i}\right), \tag{4.2}$$

where $1/\tau_i = 1/\tau_{\mathrm{r},i} + 1/\tau_{\mathrm{nr},i}$. If multiple exponential components originate from independent, multiple regions, V_i can be regarded as the volume of each region. Each coefficient of the exponential functions [I_i in $I(t) = \sum_i I_i \exp(-t/\tau_i)$] is proportional to initial carrier number of each region ($n_0 V_i$).

IQEs are given by the ratio between the number of radiatively recombined carriers and the total number of carriers. Because I_i is proportional to $n_0 V_i$, the experimentally determined overall IQE, η_{IQE}, is expressed as

$$\eta_{\mathrm{IQE}} = \frac{\sum_i I_i \eta_{\mathrm{IQE},i}}{\sum_i I_i}, \tag{4.3}$$

$$\eta_{\mathrm{IQE},i} = \frac{1/\tau_{\mathrm{r}}}{1/\tau_i}, \tag{4.4}$$

where $\sum_i I_i$ corresponds to the total number of carriers and $\eta_{\mathrm{IQE},i}$ is the IQE of each region. We can derive τ_{r} and $\tau_{\mathrm{nr},i}$ using estimated values for η_{IQE}, τ_i, and I_i (Fig. 4.4 and Table 4.1):

$$\tau_{\mathrm{r}} = \frac{\sum_i I_i \tau_i}{\eta_{\mathrm{IQE}} \sum_i I_i}, \tag{4.5}$$

$$\tau_{\mathrm{nr},i} = \frac{1}{1/\tau_i - 1/\tau_{\mathrm{r}}}. \tag{4.6}$$

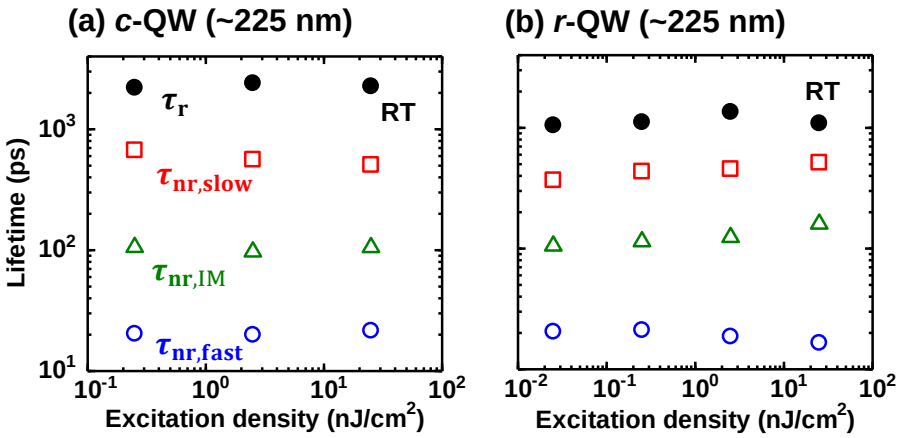

Figure 4.8: Estimated lifetimes of (a) c-QW and (b) r-QW which emit at a wavelength of ∼225 nm.

Table 4.2: Ratios of IQEs and those of the inverse of radiative lifetimes between the r- and c-QWs.

Excitation density (nJ/cm^2)	0.25	2.5	25
$\eta_{\mathrm{IQE},r}/\eta_{\mathrm{IQE},c}$	2.2	2.4	3.5
$\frac{(1/\tau_\mathrm{r})_r}{(1/\tau_\mathrm{r})_c}$	2.0	1.8	2.1

Figure 4.8 shows the derived τ_r and $\tau_{\mathrm{nr},i}$. The $\tau_{\mathrm{nr},i}$ values of the r-QW are nearly the same as those of the c-QW. However, the τ_r of the r-QW is one-half that of the c-QW. Although the well width of the c-QW is 1 nm and that of the r-QW is 1.5 nm, the τ_r of the r-QW is shorter.

We here estimate the contribution of the approximately twofold-enhanced radiative recombination probability (Fig. 4.8) to the IQE improvement (Fig. 4.4). Equation (4.3) is deformed to

$$\eta_\mathrm{IQE} = \frac{1}{\tau_\mathrm{r}}\left(\sum_i I_i\tau_i\right), \tag{4.7}$$

where I_i is normalized ($\sum_i I_i = 1$). Table 4.2 compares the ratio of η_IQE and that of $1/\tau_\mathrm{r}$ between the r- and c-QWs. When the excitation density is low, the η_IQE ratio is approximately equal to the $1/\tau_\mathrm{r}$ ratio. Therefore, at the low excitation density, the larger IQEs of the r-QW compared with those of the c-QW are attributed to the shorter radiative lifetimes of the r-QW. However, the η_IQE ratio is larger than the $1/\tau_\mathrm{r}$ ratio when the excitation density increases, which means that the higher IQEs of the r-QW under higher excitation densities are due to not only a faster τ_r but also a larger

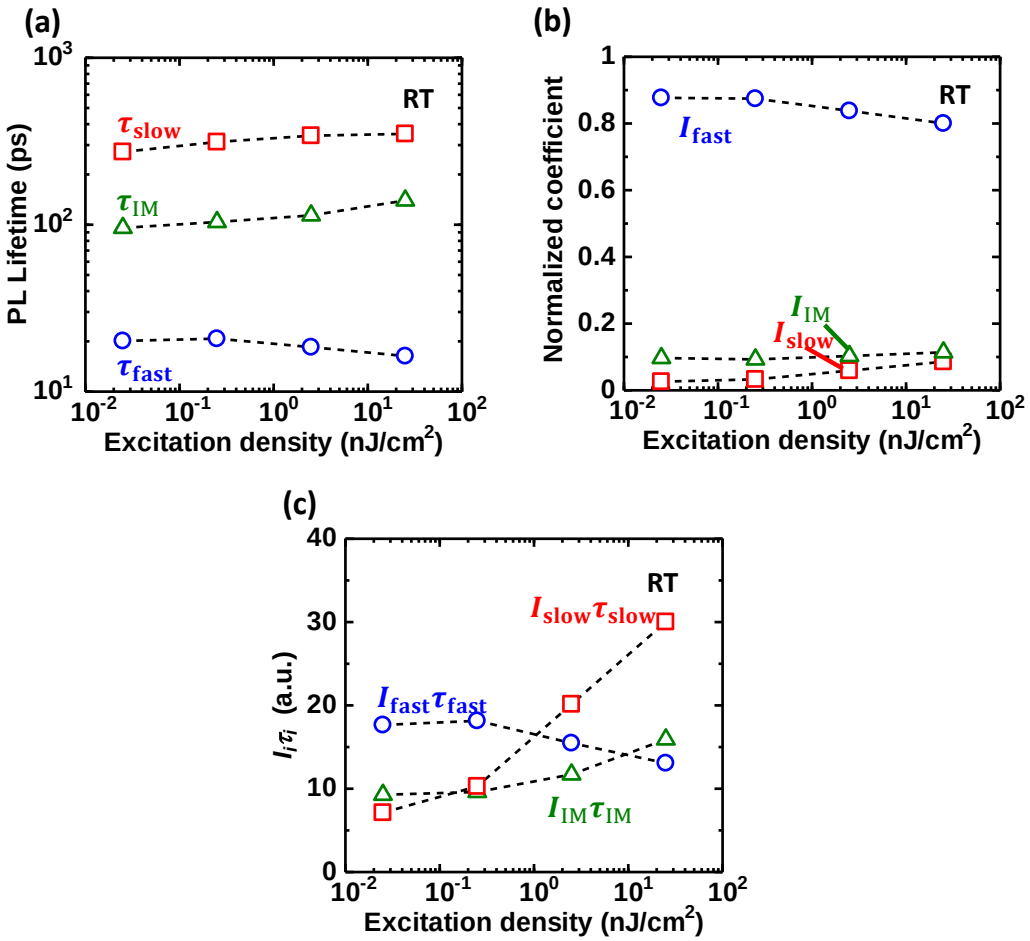

Figure 4.9: Excitation density dependences of (a) PL lifetimes τ_i, (b) coefficients of each exponential function I_i, and (c) their product $I_i\tau_i$ of the r-QW which emit in far-UVC region with a wavelength of ∼225 nm.

$\sum_i I_i\tau_i$ [Eq. (4.7)].

To distinguish the contributions of τ_i and I_i to the increase in $\sum_i I_i\tau_i$, Fig. 4.9 shows the excitation power dependence of τ_i, I_i, and $I_i\tau_i$. When the excitation density is increased from 0.025 nJ/cm^2 to 25 nJ/cm^2, τ_{IM} and τ_{slow} slightly increase by a factor of ∼1.3 [Fig. 4.9(a)]. By contrast, I_{slow} substantially increases by a factor of ∼3.3 [Fig. 4.9(b)]. As a result, $I_{\mathrm{slow}}\tau_{\mathrm{slow}}$ increases by a factor of ∼4.2 [Fig. 4.9(c)]. Therefore, the increase in I_{slow} is the main contributor to the increase in the IQEs of the r-QW under high excitation densities. Because the degrees by which I_{slow} increases and I_{fast} decreases are approximately the same [Fig. 4.9(b)], and because $I_i \propto V_i$, we presume that part of the volume characterized by fast recombination is changed to a volume characterized by slow recombination. We consider that this change can occur when nonradiative recombination centers in V_{fast} are filled with photogenerated carriers. [133, 135] Notably, Fig. 4.8 suggests that the $\eta_{\mathrm{IQE},i}$ values are nearly independent of the excitation densities. Therefore, the increase in the total IQE of the r-QW (Fig. 4.4) is not due to the improvement of component $\eta_{\mathrm{IQE},i}$ values but is due to the increase in I_{slow} (*i.e.*, due to the increase in the contribution from the high IQE component). By contrast, I_{slow} in the c-QW was nearly unchanged by the excitation density (Fig. 4.6). The reason for the different behaviors of I_{slow} in the c- and r-QWs is unclear but might be attributable to the r-QW having fewer nonradiative recombination centers than the c-QW. This hypothesis is supported by the higher total IQE in the r-QW and by the fact that homoepitaxially grown r-AlN typically has a lower density of point defects than c-AlN. [136] In addition, the types of nonradiative recombination centers might differ between the c- and r-QWs.

4.3 Optical Polarization PL of AlGaN/AlN QWs

The type of top of valence bands affects on light extraction. There are three valence bands in wurtzite III-nitrides, which are called as heavy-hole (HH), light-hole (LH) and crystal-field split-off hole (CH or SH) bands. HH consists of the p_x- and the p_y-like states, LH consists mainly of the p_x- and the p_y-like states, and CH consists of mainly the p_z-like state. (Coordinate system is taken as in Fig. 2.1.) As a result, $\boldsymbol{E} \perp c$ when HH band is the top valence band, mainly $\boldsymbol{E} \perp c$ when LH band is the top valence band, and mainly $\boldsymbol{E} \parallel c$ when CH band is the top valence band, where $\boldsymbol{E}$ is the electric field of light emitted by the recombination of electrons and holes. Therefore,

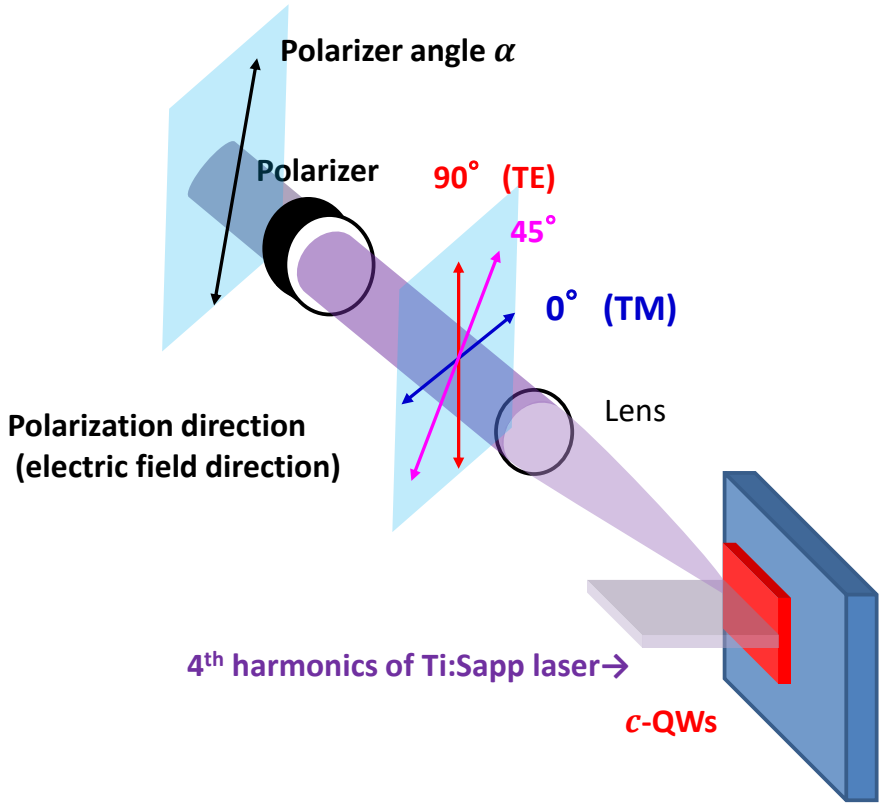

Figure 4.10: Measurement system of optical polarization PL of c-plane QWs.

when CH band is the top valence band and c-plane is used as a growth plane, LEE becomes very low as theoretically confirmed in Sec. 2.4.2. In this section, light extraction is experimentally discussed through polarization PL measurement.

4.3.1 Measurement of Optical Polarization (c-plane)

Measurement System

Figure 4.10 shows the measurement system of optical polarization PL of c-plane QWs. Used laser was the same as described in Sec.4.2.2. Laser was focused by a cylindrical lens from the surface normal, and emission was observed from the sample edge with a polarizer. Optical polarization PL was performed at RT.

Measurement Results

Figure 4.11 shows the measurement result of out-of-plane optical polarization of *c*-AlGaN/AlN QWs (well width: 1 nm). The emission of TE mode is stronger than TM mode. The stronger emission of TE mode is due to the use of AlN as barrier layers and thin QW width. Figure 4.12 shows reported measurement result of out-of-plane optical polarization of *c*-AlGaN/AlGaN (1/5 nm) QWs [137]. When emission wavelength is ∼225 nm, stronger emission of TE mode than TM mode is confirmed in the case of AlGaN/AlN QWs (Fig. 4.11). However, weaker emission of TE mode than TM mode is confirmed in the case of AlGaN/AlGaN QWs (Fig. 4.12, 2nd figure from the left). This difference is due to the reduction of barrier height and consequent weaker quantum effect [70], and is also theoretically confirmed in Sec. 2.4.2. Practically AlGaN barriers and large well widths are necessary for LEDs from the point of view achieving sufficient CIEs. Figure 4.13 (a) shows simulated current density dependence of CIEs of *c*-LEDs with $Al_{0.88}Ga_{0.12}N$ or AlN barriers. Structures for the calculation are the same as that shown in Fig. 2.9 except for barrier layers. Figure 4.13 (b) shows CIEs of *c*-LEDs with thinner QWs (Fig. 4.13 (a): 2 nm, Fig. 4.13 (b): 1 nm). The change in barrier from AlGaN to AlN and thinner well width lead to drastic reduction in CIEs. Therefore, from the point of view achieving both of high CIEs and high LEEs, the use of *c*-plane is not suitable for far-UVC LEDs.

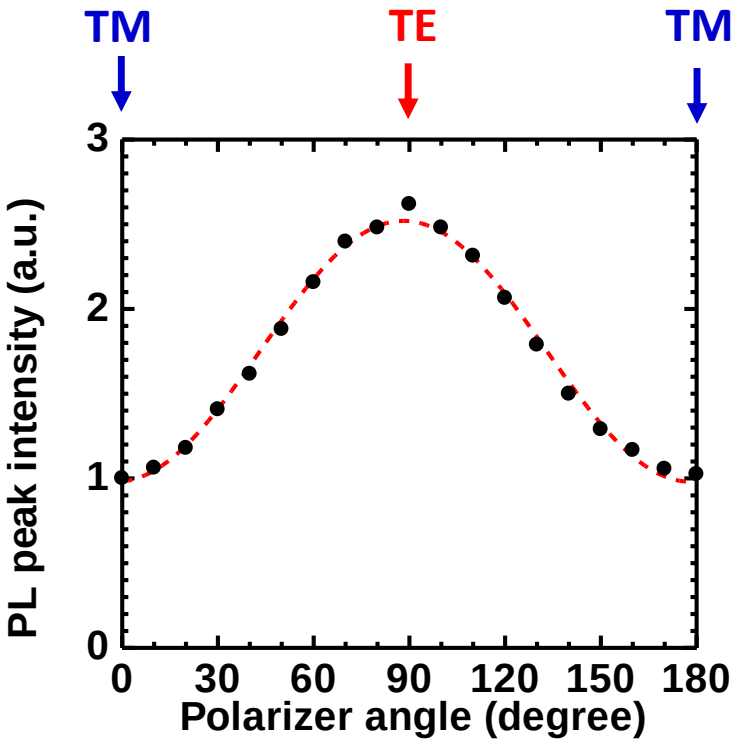

Figure 4.11: Measurement result of out-of-plane optical polarization of *c*-AlGaN/AlN (1/5 nm) QWs emitting at 225 nm.

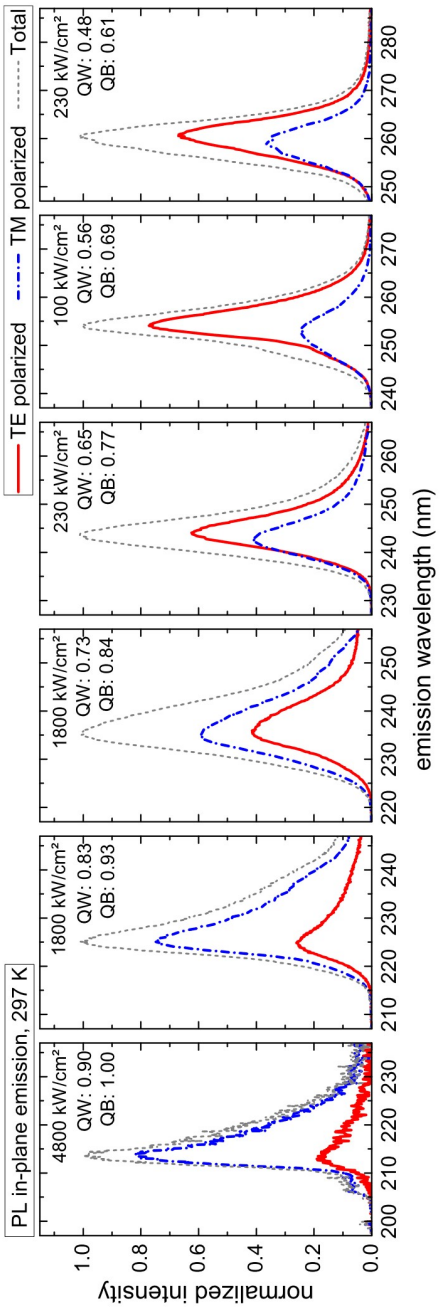

Figure 4.12: Reported out-of-plane optical polarization of c-AlGaN/AlGaN (1/5 nm) QWs [137].

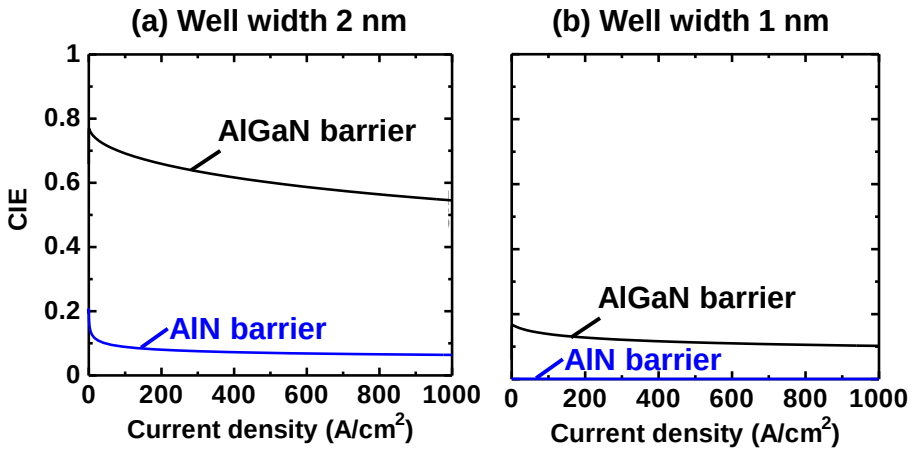

Figure 4.13: Simulated current density dependences of CIEs of c-LEDs with AlGaN or AlN barriers. The well widths are (a) 2 nm, and (b) 1 nm.

4.3.2 Measurement of Optical Polarization (r-plane)

Measurement System

Figure. 4.14 shows a sample shape of r-plane samples and a coordinate system. There is no symmetry in the x' and y' directions. However, out-of-plane optical polarization PL should be performed only along y'-axis. This is because total reflection will occur on m-plane, which is one of the exposed planes and an inclined plane of the $y'z'$ plane. Therefore, not only out-of-plane polarization PL but also in-plane polarization PL was performed. Figure 4.15 shows the measurement systems. Coordinate system in Fig. 4.15 is the same as that in Fig. 4.14. PL system of out-of-plane polarization PL for r-QWs is basically the same as that for c-QWs. PL system of in-plane polarization PL is basically the same as that of usual PL described in Sec.4.2.2, except for the insertion of polarizer.

Measurement Results

Figure 4.16 (a) shows experimentally obtained optical polarization on a-plane (one of out-of-plane polarization) and Fig. 4.16 (b) shows that on r-plane (in-plane polarization). $I_{\boldsymbol{E}\|c} > I_{\boldsymbol{E}\|m} > I_{\boldsymbol{E}\|a}$ means $|M_z|^2 > |M_x|^2 > |M_y|^2$, where I is an emission intensity and M is an optical transition matrix element. Although the ratio is slightly different, this trend is the same as in theoretical calculations (Fig. 2.8).

Light extraction is also compared according to experimental results of

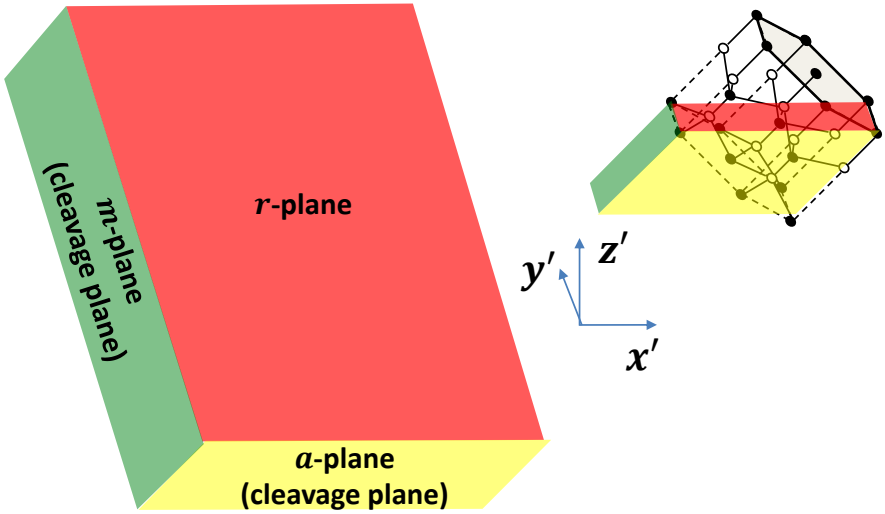

Figure 4.14: Sample shape of r-plane samples.

optical polarization PL and Eq. (2.22). As a result, light extraction from the r-AlGaN/AlN QW (well width:1.5 nm) is estimated to be 0.6 times higher than that from the c-AlGaN/AlN QW (well width:1.0 nm) at wavelength of ∼225 nm. This estimation contradicts with the experimental results of PL intensity (Sec. 4.2.3) and IQE (Sec. 4.2.5), which estimates 3.9 times higher light extraction from the r-QW than the c-QW. The reason for this discrepancy is currently unknown and should be investigated in the future.

4.4 Evaluation of r-AlGaN/AlGaN QWs

Toward fabricating LEDs, AlGaN should be used as a barrier layer instead of AlN as shown in Fig. 4.13. In this section, r-AlGaN/AlGaN QWs are fabricated on the basis of growth conditions established in Chap. 3 and evaluated.

4.4.1 Structure and Growth Condition

In this section, all samples were fabricated at the upstream position. Firstly r-AlGaN was grown on r-AlN substrate under the optimal conditions described in Sec. 3.3.2 for 60 min (∼660 nm) followed by AlGaN/AlGaN QWs (2/5 nm) and 20-nm-thick cap AlGaN layer. AlN molar fractions of sublayer, barrier layer, and cap layer are identical. Figure 4.17 shows the way of supplying precursors. AlN molar fraction of well layer was adjusted by adding TMG

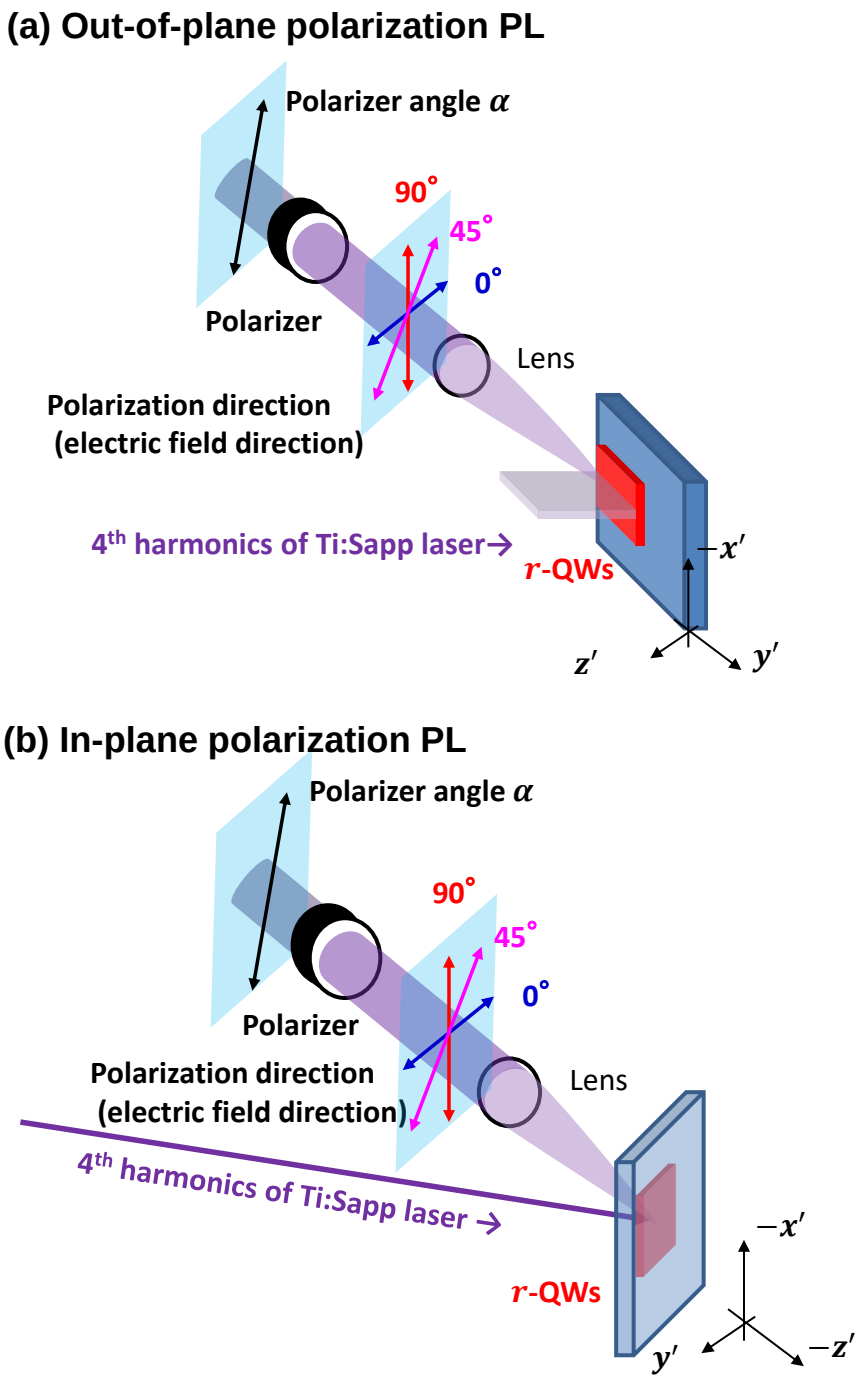

Figure 4.15: Measurement systems of (a) out-of-plane and (b) in-plane optical polarization PL of r-plane QWs.

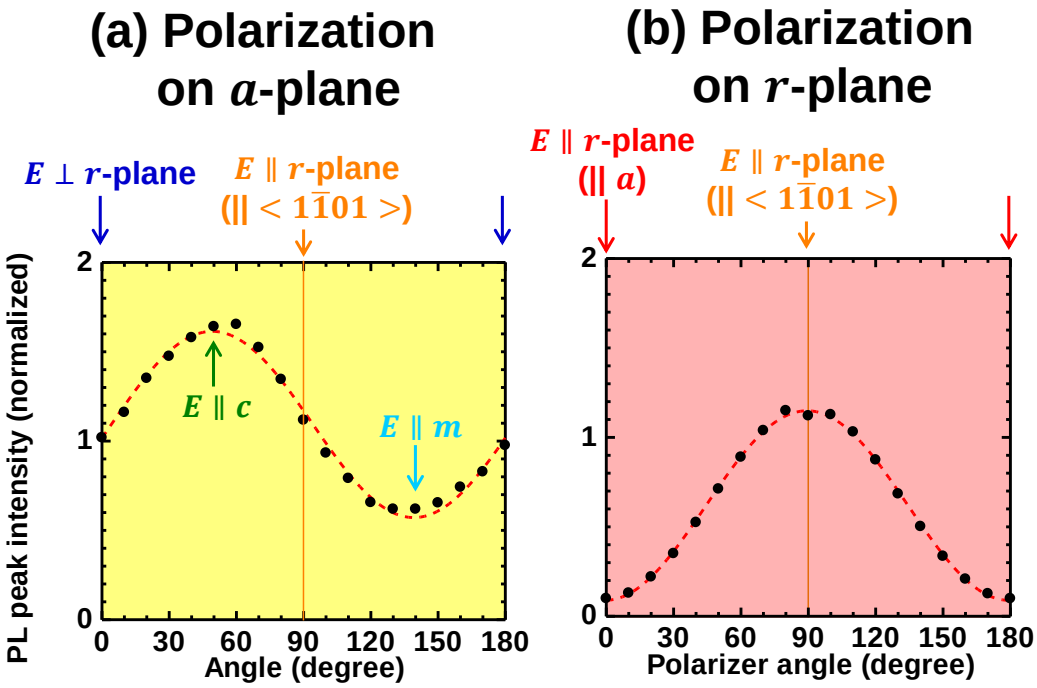

Figure 4.16: Measurement results of optical polarization (b) on a-plane, and (c) r-plane of r-AlGaN/AlN QWs which emit at a wavelength of ∼225 nm.

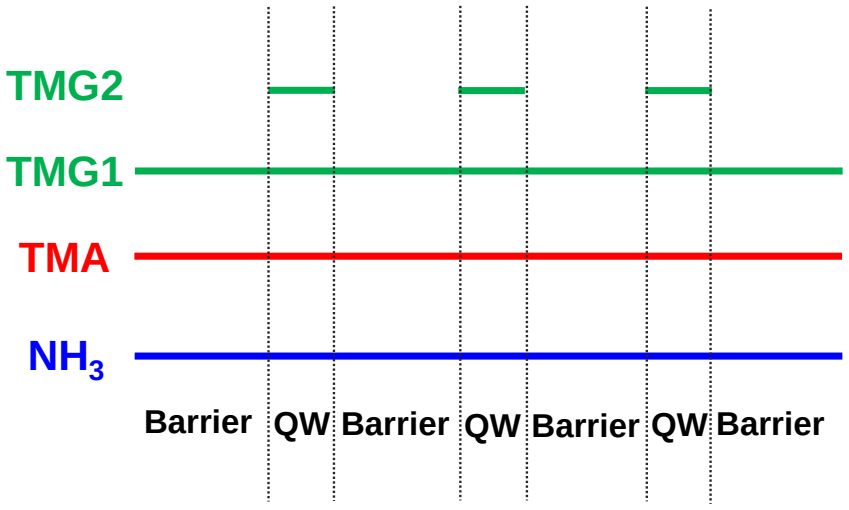

Figure 4.17: Method of gas supply during fabrication of QWs.

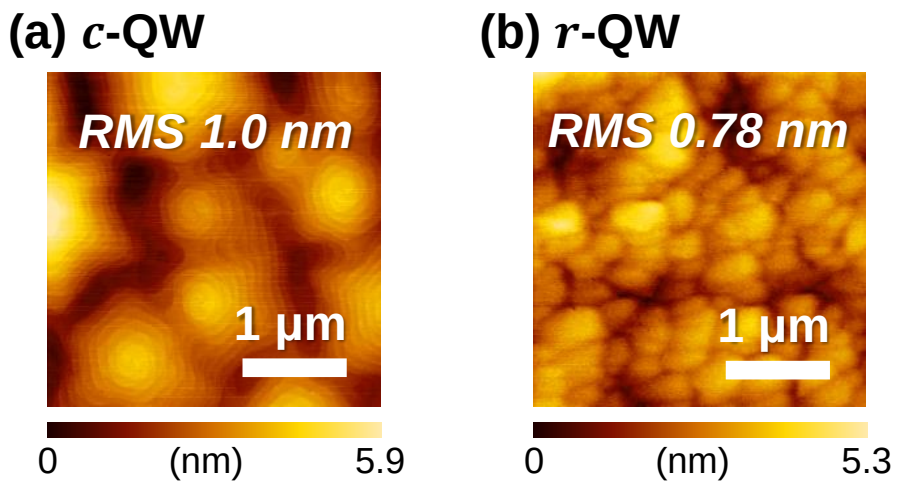

Figure 4.18: AFM images of (a) c- and (b) r-AlGaN/AlGaN QWs grown side-by-side at the upstream position.

to growth conditions of barrier layer. We also fabricated c-AlGaN/AlGaN QWs by placing a c-AlN/sapp. template and an r-AlN substrate side by side.

4.4.2 Surface and Interface

Figure 4.18 shows AFM images of AlGaN/AlGaN QWs grown at the upstream position. Both of the c- and r-QWs have smooth surfaces. Figure 4.19 shows cross-sectional TEM images of AlGaN/AlGaN QWs grown at the upstream position. (Designed barrier width for the TEM samples was 20 nm.) Both of the c- and r-QWs have abrupt interfaces. QW and barrier thicknesses are the same as designed ones, and there are no differences in QW thickness between the c- and r-QWs.

4.4.3 Emission Spectra

Figure 4.20 shows PL spectra of c- and r-AlGaN/AlGaN QWs grown side-by-side at the upstream position. Stronger emission is observed from r-AlGaN/AlGaN QWs. The peak energy difference between the c- and r-AlGaN/AlGaN QWs suggests smaller AlN molar fraction of the r-QW than the c-QW. This is because STEM observations (Fig. 4.19) confirm similar QW thicknesses and because presumably smaller electric field in r-QWs than c-QWs would lead to a shorter wavelength if AlN molar fractions were identical. The r-plane seems to incorporate Ga more efficiently than the c-plane

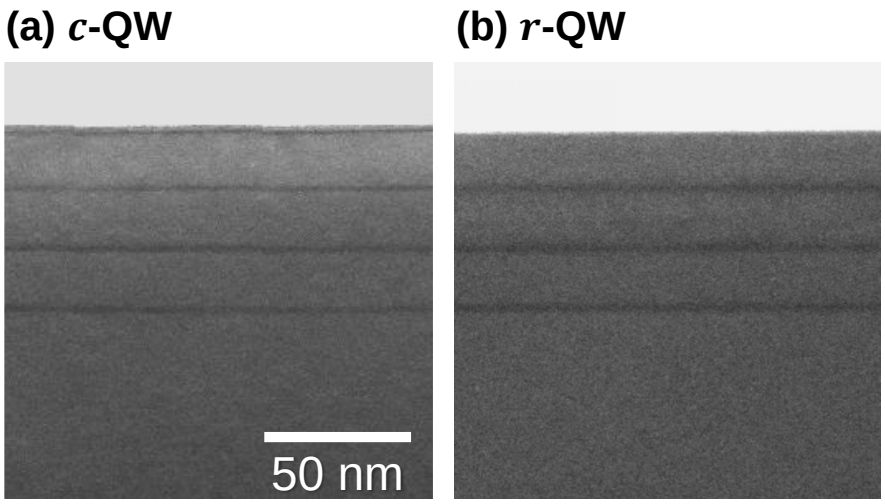

Figure 4.19: Cross-sectional STEM bright-field images of (a) c- and (b) r-AlGaN/AlGaN QWs grown side-by-side at the upstream position.

and this is also confirmed by energy dispersive X-ray spectrometry (EDS).

4.4.4 Temperature Dependence

Figure 4.21 shows temperature dependence of PL integrated intensity of r-AlGaN/AlGaN QWs emitting at ∼260 nm at RT. The excitation energy density per pulse was 7.1 nJ/cm^2. The ratio of RT and LT integrated intensity was 0.4 %. One of the reason for the low ratio may be the non-selective excitation condition. However, further optimization of QW layer may be needed.

4.5 Summary

In this chapter, optical characteristics of fabricated c- and r-QWs were investigated by PL measurement. PL intensities of the fabricated AlGaN/AlN QWs decreased as wavelengths became shorter. The degrees of the decrease were different between the c- and the r-QWs, and the r-QWs showed much higher PL intensities especially in the far-UVC region (e.g. ∼14 times higher at ∼225 nm). In fact, the IQE and LEE of r-QW emitting at ∼225 nm were 3.4 and 3–4 times higher than those of c-QW. Then, TRPL measurements were performed at RT. The analyses of TRPL decay curves revealed that the reason for the higher IQE of the r-QW was shorter radiative lifetime of the r-

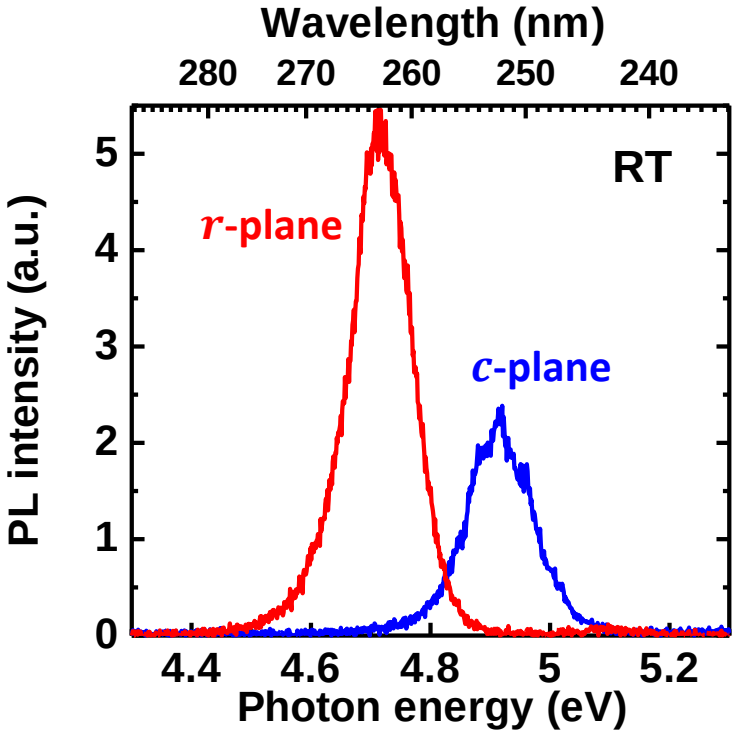

Figure 4.20: PL spectra of c- and r-AlGaN/AlGaN QWs grown side-by-side at the upstream position. The excitation energy density per pulse was 7.1 nJ/cm^2.

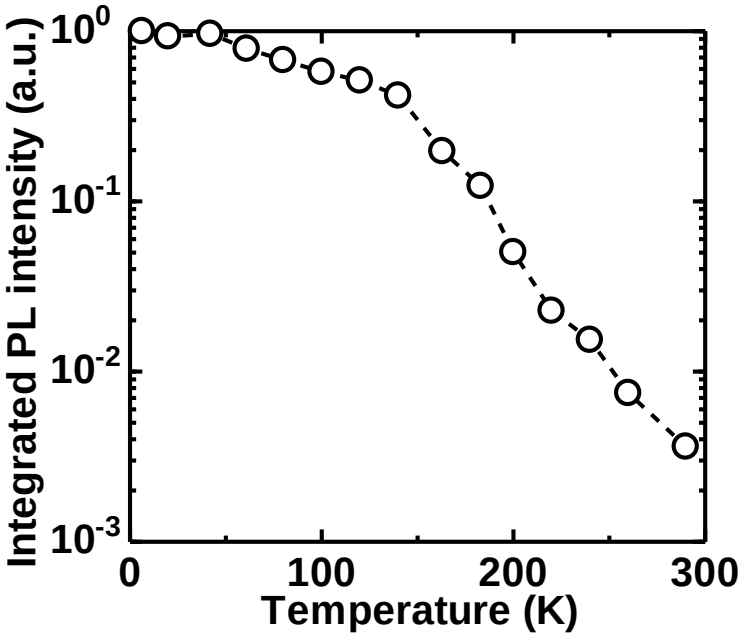

Figure 4.21: Temperature dependence of PL integrated intensity of r-AlGaN/AlGaN QWs which emit at ∼260 nm at RT.

QW and possibly reduced non-radiative recombination centers in the r-QW. AlGaN/AlGaN QWs were also fabricated. AlN molar fraction of AlGaN on r-plane was found to be smaller than that on c-plane. This is because the wavelength of r-QW was longer than that of c-QW grown side by side and because no difference in thicknesses was observed between c- and r-QWs.

Chapter 5

Demonstration of Semipolar r-plane UVC LED

5.1 Introduction

We have established growth conditions for thick r-plane AlGaN films and for QWs emitting in the UVC region in Chap. 3 and Chap. 4. Toward fabrication of LEDs, fabrication of n- and p-type layers is necessary. In this chapter, doping techniques of semipolar r-plane AlGaN films are established based on the growth conditions obtained in Chap. 3. Subsequently, r-plane AlGaN-based UVC LEDs are demonstrated.

5.2 Fabrication of n-AlGaN

For demonstrations of LEDs, n-AlGaN is needed instead of n-AlN because of their high resistivity [4, 62, 63]. Therefore, r-plane n-AlGaN films with sufficient conductivity are fabricated in this section. We used tetraethylsilane (TES) as a precursor of Si donor.

5.2.1 Electric Characteristics of Si-doped c-AlGaN

We firstly optimized TES flow rate by fabricating Si-doped AlGaN on c-AlN/sapphire template due to the limited number of r-AlN substrates. We used the upper position as the growth position described in Sec. 3.2.2. TMA, TMG and NH_3 flow rate of Si-doped AlGaN is the same as that of the optimal value at the upper position described in Sec. 3.3.2. The growth time is 60 min. After growths, Ti/Al/Ti/Au (30/100/50/200 nm) electrodes were deposited by thermal evaporation and annealed for 30 s in air at 900 °C. The annealing

Table 5.1: Hall effect measurement of Si-doped c- and r-AlGaN.

Plane	Carrier type	Resistivity Ω·cm	Mobility $cm^2/V{\cdot}s$	Carrier density cm^{-3}
c	n	2.0×10^{-2}	30	1.1×10^{19}
r	n	1.3×10^{-2}	31	1.6×10^{19}

process is necessary to reduce the potential barrier width at the interface between AlGaN and the electrodes by the formation of N vacancies resulting from the formation of TiN [138]. Just before the deposition of electrodes, AlGaN films are dipped into a 3:1 H_2SO_4:H_3PO_4 mixture for 10 min at 90 °C in order to remove the oxidized layer formed on the surface.

Figure 5.1 shows results of Hall effect measurements on n-AlGaN fabricated at various TES flow rates. The applied current is 1 mA. The results of n-AlGaN on c-sapphire previously fabricated by the MOVPE machine used in this thesis is included in Fig. 5.1 [139]. Electron density increases linearly with TES flow rate and the self-compensation effect was not observed within this range. Therefore, further optimization can be done but the lowest resistivity is comparable to reported ones [119]. In this study, the optimal TES flow rate was set to 26.7 nmol/min.

5.2.2 Electric Characteristics of Si-doped r-AlGaN

A Si-doped r-AlGaN film is fabricated at the optimal TES flow rate described in Sec. 5.2.1. The other gas flow rates were set to the optimal ones described in Sec. 3.3.2. The thickness of the Si-doped r-AlGaN was set to 660 nm. Prior to the 660-nm-thick Si-doped r-AlGaN, 330-nm-thick undoped AlGaN was grown in order to suppress the diffusion of impurities into Si-doped AlGaN. Figure 5.2 shows AFM images of undoped and Si-doped r-$Al_{0.7}Ga_{0.3}N$. The surface morphology is worse than that of undoped r-AlGaN, but the RMS of surface roughness is still as low as 2.1 nm.

Ti/Al/Ti/Au (30/100/50/200 nm) electrodes were deposited on the Si-doped r-AlGaN. Figure 5.3 shows I-V characteristics of the optimal c- and r-plane Si-doped AlGaN films. Although the annealing process was performed at as high as 900 °C, they still show non-Ohmic characteristics. It is reported that vanadium-based electrodes show better electrical characteristics than titanium-based electrodes [140, 141]. Electrodes should be changed in the future works. As shown in Fig. 5.3, r-plane Si-doped AlGaN shows higher slope than c-plane Si-doped AlGaN at high voltages. This means lower resistivity of r-plane Si-doped AlGaN, which may result from lower AlN mo-

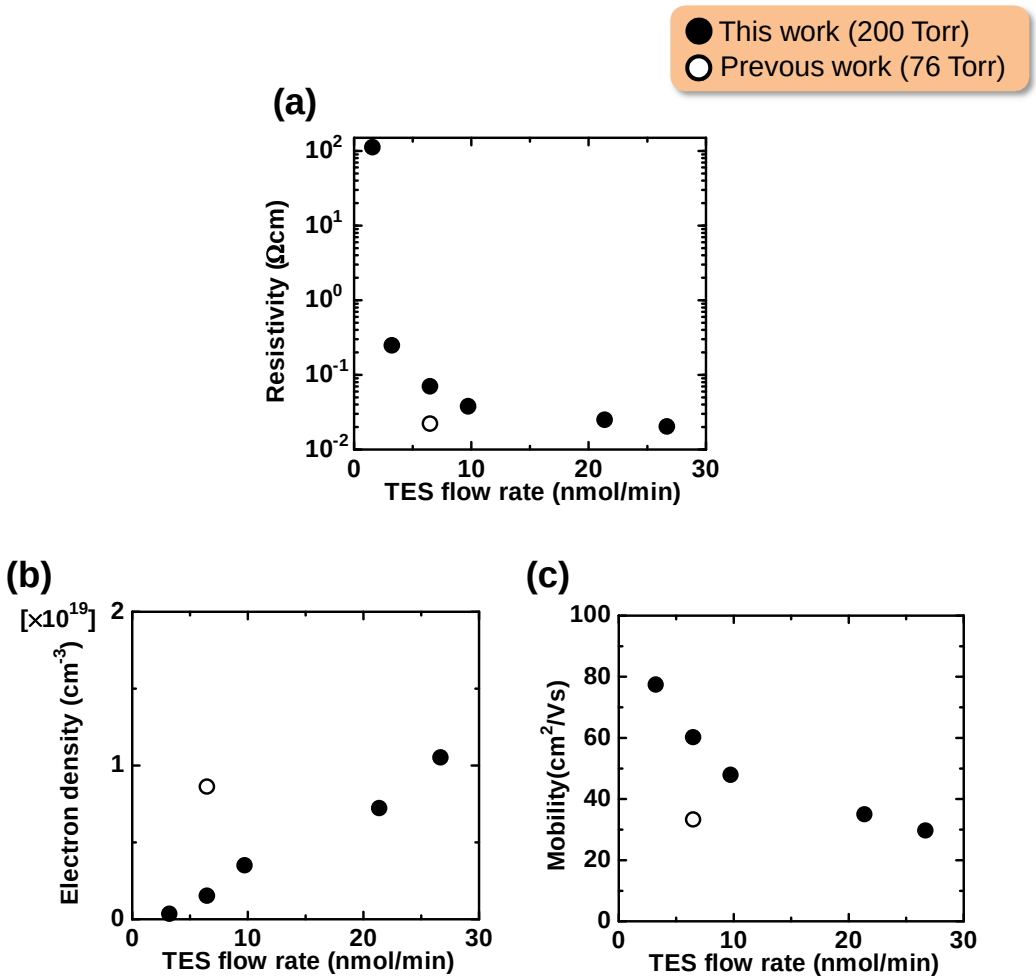

Figure 5.1: Electric characteristics of Si-doped *c*-AlGaN grown on *c*-AlN/sapphire template, (a) resistivity, (b) electron density, and (c) mobility.

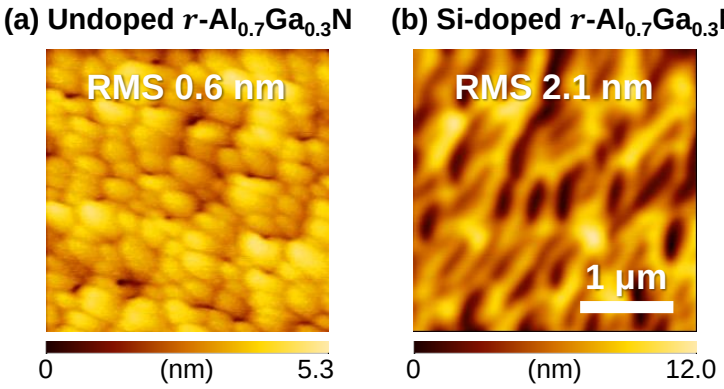

Figure 5.2: AFM images of (a) undoped and (b) Si-doped r-$Al_{0.7}Ga_{0.3}N$.

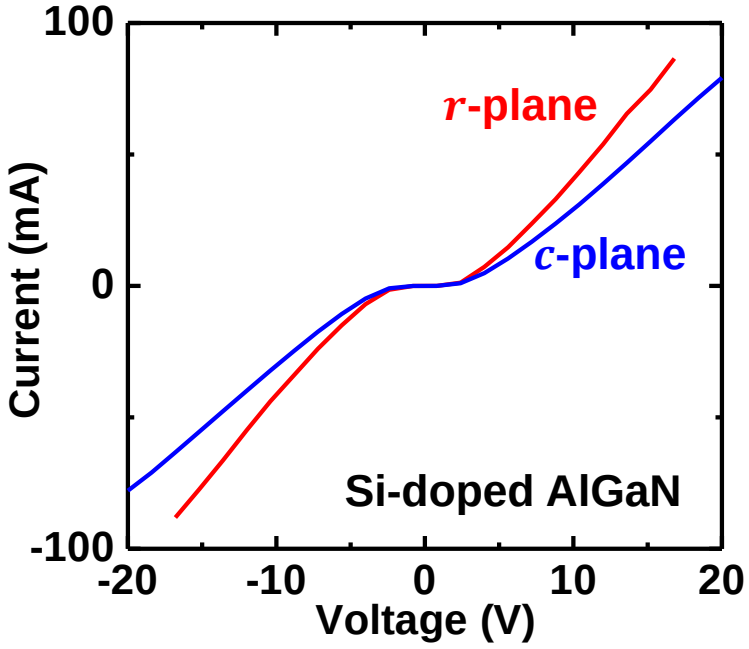

Figure 5.3: IV characteristics of Si-doped c- and r-AlGaN.

lar fraction and consequent lower Si donor ionization energy [62, 142–144] of r-AlGaN than c-AlGaN. It should be noted that turn-on voltages of c- and r-plane Si-doped AlGaN are nearly the same. This means nearly the same net donor density and degree of Fermi level pinning between c- and r-plane Si-doped AlGaN. Table 5.1 shows results of Hall effect measurements for the c- and r-plane Si-doped AlGaN. The higher carrier density of r-plane Si-doped AlGaN may result from the lower Si ionization energy of lower AlN molar fraction of r-AlGaN. Mobilities are nearly the same between c- and r-plane Si-doped AlGaN.

5.3 Demonstration of Semipolar r-plane UVC-LED

Structure

Figure 5.4 shows designed LED structure. The LED consists of ∼2-µm-thick n-AlGaN, 3-period $Al_xGa_{1-x}N$ (2 nm) / $Al_yGa_{1-y}N$ (5 nm) QWs, undoped AlN (1 nm) electron blocking layer, undoped $Al_yGa_{1-y}N$ (7.5 nm), undoped $Al_xGa_{1-x}N$ (7.5 nm), and ∼150-nm-thick p-GaN. The undoped $Al_yGa_{1-y}N$ (7.5 nm) and $Al_xGa_{1-x}N$ (7.5 nm) layers are inserted with the intention of improving hole injection into the QW region by the formation of psuedo-graded AlGaN layer, but the effect has not been verified.

Fabrication of c-plane p-GaN

Prior to fabrication of r-plane UVC LEDs, c-plane Mg-doped p-GaN was grown at the same gas flow rate as that of r-GaN described in Sec. 3.3.3. Cp_2Mg was used as a precursor of Mg. The II/III ratio was set to 1.93×10^{-3}. After the growth, annealing was performed at 600 °C for 10 min in the air in order to activation of Mg acceptors. Then Ni/Au(5/200 nm) electrodes were deposited and annealing was performed at 400 °C for 10 min in the air in order to the improvement of I-V characteristics. Hall effect measurement performed. p-Type conductivity was confirmed and the hole density, the mobility, and the resistivity were 2.2×10^{18} cm^{-3}, 1.8 $cm^2/(V\cdot s)$, and 1.6 Ω·cm, respectively. (p-Type conductivity has yet to be directly confirmed for r-GaN.)

Results

The epitaxial wafer is defined into 500 × 500 μm^2 LED mesas via photolithography and reactive ion etching. All measurements were performed on-wafer

Figure 5.4: Designed r-plane LED structure which emit UVC light in this study.

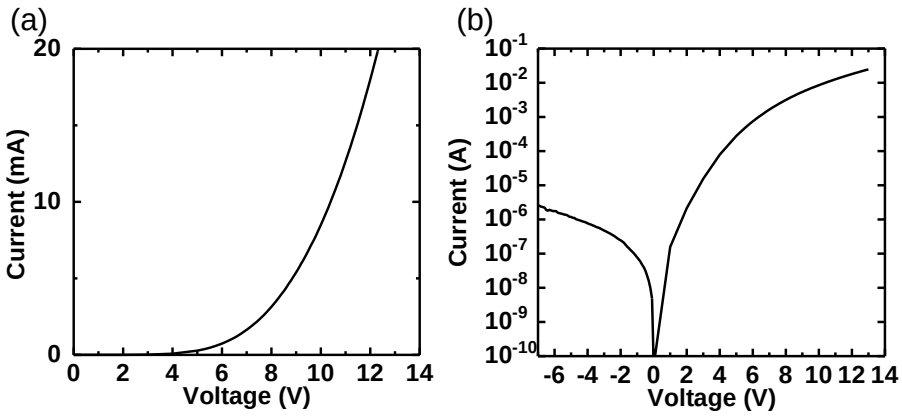

Figure 5.5: IV characteristics of the fabricated r-plane UVC LED, (a) linear scale plot and (b) semi-log scale plot.

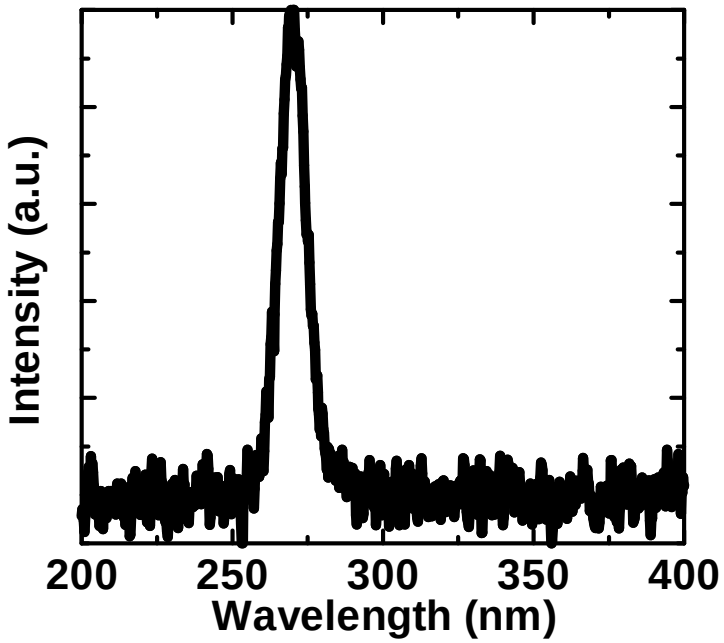

Figure 5.6: EL spectrum of the r-AlGaN based UVC LED acquired under forward current injection of 5 mA.

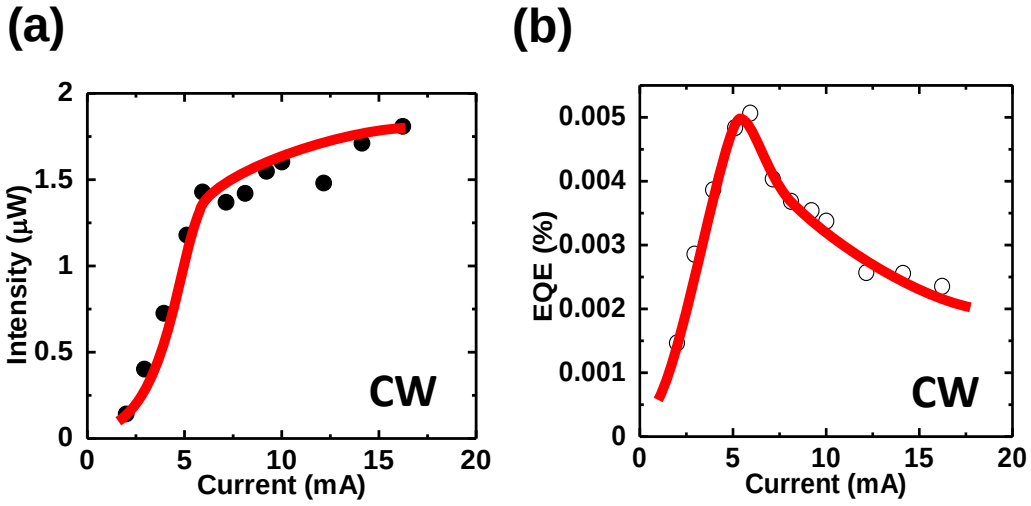

Figure 5.7: Current dependences of (a) EL intensity and (b) EQE of the r-AlGaN based UVC LED. Current was applied under a continuous wave (CW) condition.

at room temperature under continuous wave operation. Figure 5.5 shows current-voltage characteristics of the fabricated r-AlGaN LED. Figure 5.6 shows EL spectrum of the r-AlGaN based LED acquired under forward current injection of 5 mA. Although p-type conduction has not yet directly to be confirmed for r-GaN, clear rectifying behavior and emission at the wavelength of ∼270 nm, which is in the UVC and germicidal wavelength range, are demonstrated. Therefore, p-GaN layer on r-AlN works as a hole injection layer. The output power was estimated by placing a Si photodiode beneath the substrate. (Thus, the experimental accuracy may be inferior to that obtained with an integral sphere.) Figure 5.7 shows current dependences of EL intensity and EQE of the r-AlGaN based UVC LED. The estimated output powers for the r-UVC LED fabricated is 1.6 μW at a current of 10 mA, which correspond to EQEs of 0.0034 %, respectively. As a consequence, the maximum EQE is ∼0.005 %. The LEE is considered to be 2 % considering the reported LEE on transparent AlN substrate is 4 % [107] and the absorption of our AlN substrates (∼ 50 %). Hence, dividing the EQE by the LEE, we obtain the maximum value of a product of the IQE and CIE of 0.25%. Although further optimization is needed, this is the first demonstration of semipolar AlGaN-based UVC LEDs in the world.

5.4 Summary

In this chapter, r-plane UVC LEDs were demonstrated. Firstly, doping conditions were investigated based on r-AlGaN growth conditions established in Chap. 3. Sufficiently high conductivity of r-plane n-$Al_{0.7}Ga_{0.3}N$ was achieved. There was no difference between turn-on voltages of c- and r-plane Si-doped n-AlGaN, which means nearly the same net donor density and degree of Fermi level pinning between c- and r-plane Si-doped AlGaN. Then, r-plane LEDs emitting at 270 nm in the UVC region were successfully demonstrated.

Chapter 6

Conclusions and Future Works

6.1 Conclusions

In this thesis, MOVPE growth and characterization of semipolar r-plane AlGaN films and QWs were studied. As a result, the first semipolar UVC LED was successfully demonstrated in the world.

In Chapter 2, advantages of r-plane LEDs compared with c-plane LEDs were theoretically investigated in terms of IQEs, LEEs, and CIEs. IQEs are determined by the balance of radiative recombination and non-radiative recombination. Therefore, overlap of electrons and holes, and critical thickness were calculated. The former is related to radiative recombination process and the latter is related to non-radiative recombination process. Squared overlap integral of electrons and holes of 2-nm-thick r-plane QWs is higher than that of 1-nm-thick c-QWs. Critical thickness of r-plane AlGaN is larger than that of practical c-plane (i.e. c-plane with slight off angle). Maximum r-plane QW number without introducing misfit dislocation was calculated for 265 nm LEDs and 230 nm LEDs. In both cases, the maximum QW number is three or more than three when the well width is 2.5 nm or less than 2.5 nm. In terms of LEE, r-QWs were found to show superiority to c-QWs especially in the far-UVC region by the calculation of optical transition matrix elements. CIEs of LEDs on various planes were calculated by a commercial device simulator. CIE decreased as a growth plane was inclined from c-plane, but r-plane (43° from c-plane) LEDs have enough high CIEs. However, when a growth plane was inclined to $(11\bar{2}2)$ plane (58° from c-plane), CIEs drastically decreased. The reason for the drastic decrease in CIEs was found to be reduction of electric polarization. Considering the balance of IQE, LEE, and CIE, r-plane is the most favorable plane for UVC LEDs.

In Chapter 3, growth conditions of r-plane AlGaN films with smooth

surfaces were established. Growth condition of homoepitaxial r-AlN was established in the previous study [60] and high pressure growth of 500 Torr was found to be favorable for r-plane AlN. However, the MOVPE growth machine used in this study is different from the previous one and AlN cannot be fabricated at 500 Torr because of pre-reaction of TMA and NH_3. Therefore, the growth condition of homoepitaxial r-AlN was firstly optimized at 200 Torr and r-AlN with low pit density was successfully fabricated even at 200 Torr. Next, r-$Al_{0.7}Ga_{0.3}N$ films were fabricated under the same growth condition of r-AlN, resulted in high pit density. Increase in NH_3 flow rate was found to reduce pit density in the case of r-$Al_{0.7}Ga_{0.3}N$. These optimizations were performed at a growth pressure of 200 Torr, but high pressure growth results in poor source gas utilization efficiency. Thus low pressure growth was applied. r-AlGaN films with AlN molar fractions of 0.76, 0.83, 0.88 with low pit density were successfully fabricated by optimization of growth conditions even at low pressure of 38 Torr. Then, the mechanism of change in pit density was discussed. Pit density is determined by the balance between pit formation and pit elimination. Low NH_3 flow rate, high growth temperature, and low AlN molar fraction conditions are favorable in terms of pit formation. However, in terms of pit elimination, shorter migration length of adatoms is favorable, that is high NH_3 flow rate, high pressure, low growth temperature, and high AlN molar fraction. As a result, optimal growth conditions exist. Relaxation degrees of fabricated r-AlGaN films were also investigated. r-AlGaN films were easily relaxed along the $[1\bar{1}01]$ direction, which is expected in the theoretical calculation of relaxation process. However, they were hardly relaxed along the $[11\bar{2}0]$ direction compared with the $[1\bar{1}01]$ direction. This might be related to nearly no relaxation observed on c-AlGaN films. Dislocations originating from the stress relaxation are confined in the vicinity of the interface between AlGaN and AlN. Therefore, the effect of misfit dislocations on QWs fabricated on r-plane AlGaN films is small.

In Chapter 4, optical characteristics of fabricated c- and r-QWs were investigated by PL measurement. PL intensities of the fabricated AlGaN/AlN QWs decreased as wavelengths became shorter. The degrees of the decrease were different between the c- and the r-QWs and the r-QWs showed much higher PL intensities especially in the far-UVC region (e.g. $\sim$14 times higher at $\sim$225 nm). In fact, the IQE and LEE of r-QW emitting at $\sim$225 nm were 3.4 and 3–4 times higher than those of c-QW. Then, TRPL measurements were performed at RT. The analyses of TRPL decay curves revealed that the reason for the higher IQE of the r-QW was shorter radiative lifetime of the r-QW and possibly reduced non-radiative recombination centers in the r-QW. AlGaN/AlGaN QWs were also fabricated. AlN molar fraction

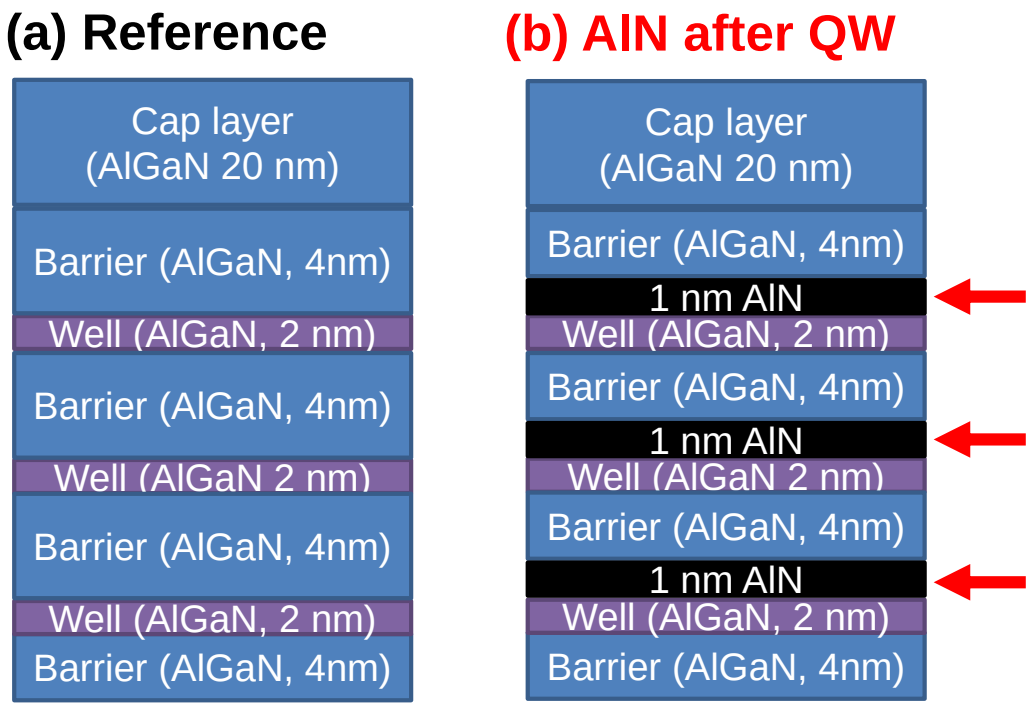

Figure 6.1: Structures of (a) reference QW and (b) QW capped with 1-nm-thick AlN.

of AlGaN on r-plane was found to be smaller than that on c-plane. This is because the wavelength of the r-QW was longer than that of the c-QW grown side by side and because no difference in thicknesses between c- and r-QWs was observed.

In Chapter 5, r-plane UVC LEDs were demonstrated. Firstly, doping conditions were investigated based on r-AlGaN growth conditions established in Chap. 3. Then, r-plane LEDs emitting at 270 nm in the UVC region were successfully demonstrated.

6.2 Future Works

6.2.1 IQE Improvement by Changing QW Structure

As shown in Fig. 5.7 (b), the maximum EQE of the demonstrated r-plane UVC LED is only ~0.005 %. Considering that the LEE is 2 %, the maximum IQE×CIE is 0.25 %. One of the reason for the low IQE × CIE might be low IQE as described in Sec. 4.4.4. Change in active layer structure enhances

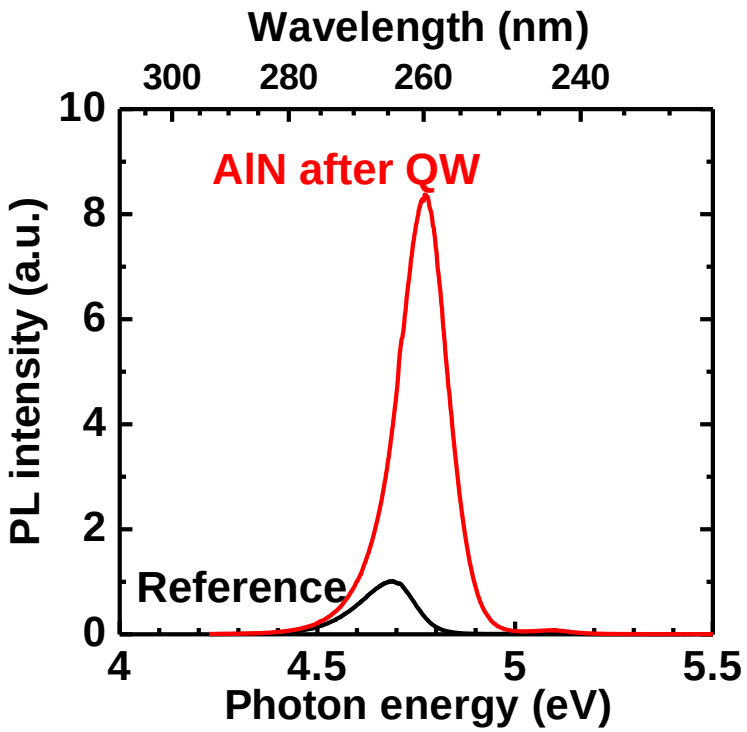

Figure 6.2: PL spectra of the reference QW (black line) and the QW capped with 1-nm-thick AlN (red line). The excitation density is 25 nJ/cm^2.

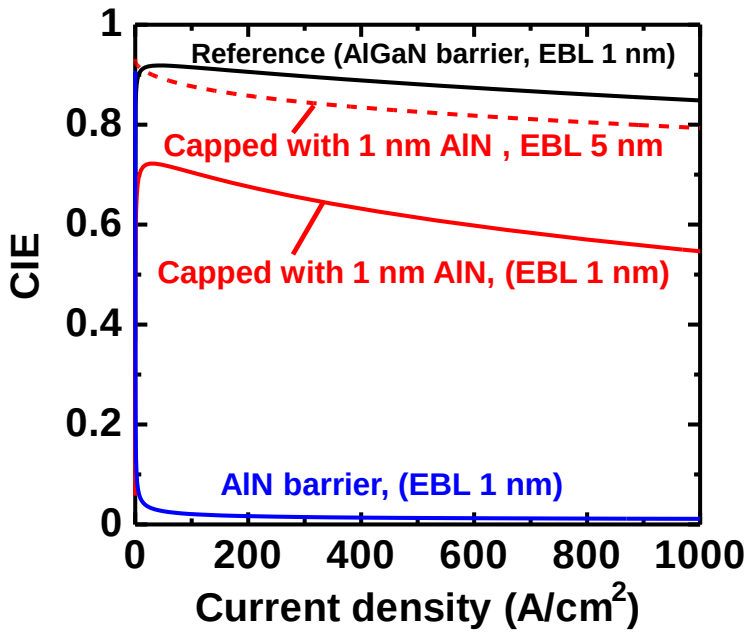

Figure 6.3: Current density dependences of CIEs of LEDs with the reference QW structure (EBL 1 nm), AlN barrier (EBL 1 nm), QW capped with 1-nm-thick AlN (EBL 1 nm), and QW capped with 1-nm-thick AlN (EBL 5 nm).

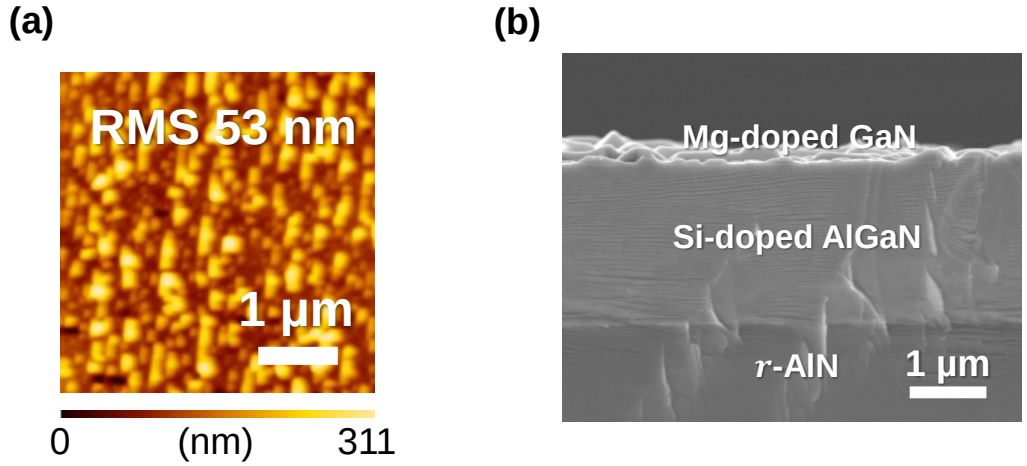

Figure 6.4: (a) AFM and (b) cross-sectional SEM images of the r-AlGaN based UVC LED which emit at ∼270 nm.

emission from QW. Figure 6.1 shows the active layer structures of reference QW and QW capped with 1-nm-thick AlN. Figure 6.2 shows PL spectra of the reference QW and the QW capped with 1-nm-thick AlN. Insertion of AlN after QW enhances the PL intensity by a factor of 8. The reason for the enhancement might be that evaporation of Ga atoms is suppressed, which leads to the reduction of cation vacancies.

The effect of change in QW structure on CIEs is also investigated by simulation. Figure 6.3 shows current density dependence of CIEs of LEDs with the reference QW structure (EBL 1 nm), AlN barrier (EBL 1 nm), QW capped with 1-nm-thick AlN (EBL 1 nm), and QW capped with 1-nm-thick AlN (EBL 5 nm). When the entire barrier structure is changed to AlN, CIE drastically decreases. However, when the barrier structure is partially changed to AlN, the CIE reduction is small. This CIE reduction can be compensated by the change in EBL structure from 1-nm-thick AlN to 5-nm-thick AlN. Therefore, the partial change in barrier structure can enhance not only IQE but also IQE×CIE.

6.2.2 Achieving Smooth Surface Roughness of r-plane p-GaN

Another reason for the low EQE of the fabricated r-plane UVC LED might be the poor surface roughness of the p-type r-GaN. Figure 6.4 shows AFM image and cross-sectional SEM image of the fabricated r-AlGaN based UVC LED. Rough surface is observed from the AFM image and this begins at p-GaN

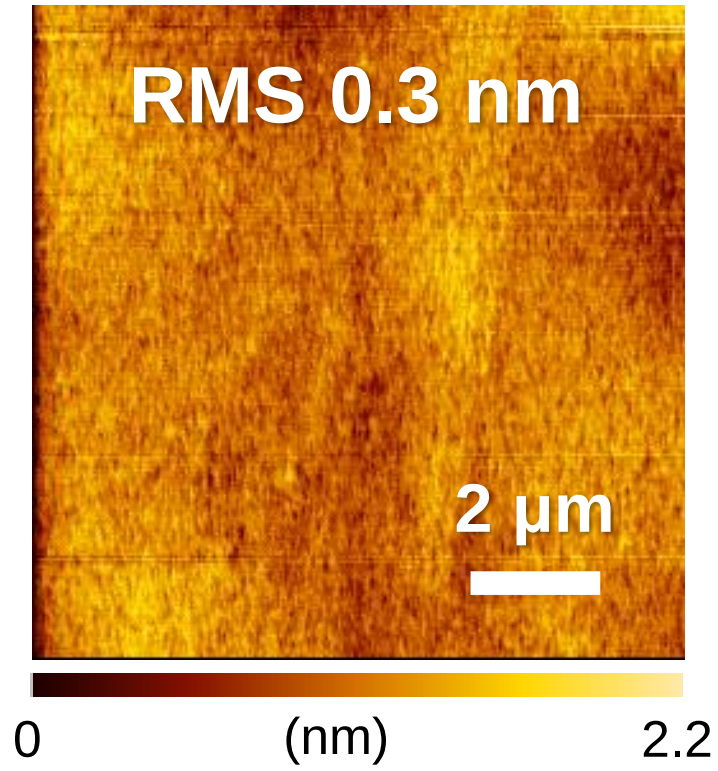

Figure 6.5: An AFM image of the optimized r-GaN film.

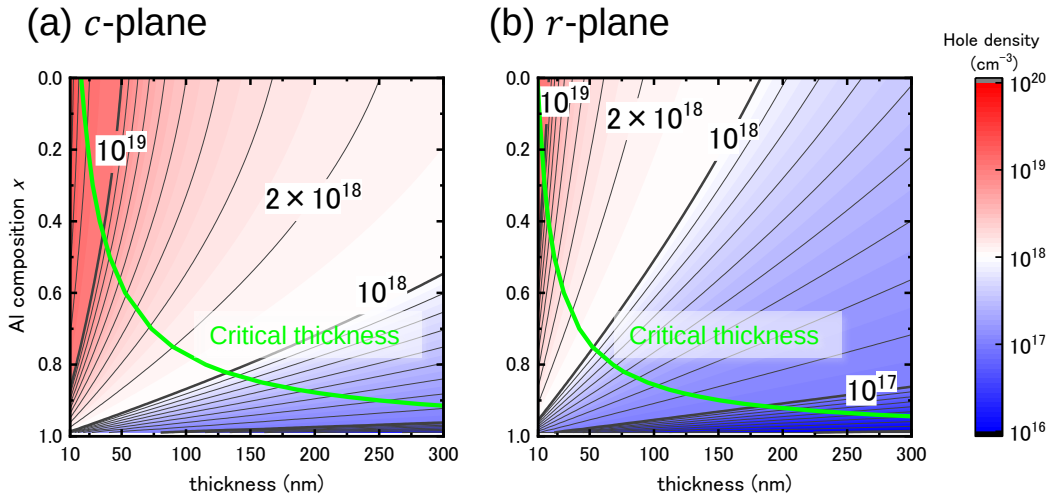

Figure 6.6: Hole density generated by polarization doping on (a) c-plane and (b) r-plane [72]. The graded-AlGaN is assumed to be coherently grown on the ideal AlN, and AlN molar fraction of the graded-AlGaN is linearly reduced from 1 to x along the growth directions.

layer according to the SEM image. This roughness might result from Mg-doping into r-GaN layer grown under the insufficiently optimized conditions or thicker thickness. Figure 6.5 shows an AFM image of the optimized r-GaN. The TMG flow rate is 28.8 µmol/min, NH_3 flow rate is 44.6 mmol/min (V/III is 1550). Monitored growth temperature is 1100 °C, growth pressure is 200 Torr, growth time is 60 min. The sample was grown at the 2inch center position. The RMS of surface roughness is as low as 0.3 nm, which is better than Fig. 3.12 and Fig. 6.4 (a). Increased growth temperature (1000 °C in Sec. 3.3.3) may result in low pit density even at lower NH_3 flow rate condition than that in Sec. 3.3.3 (134 mmol/min), as observed in Sec. 3.10 and in Sec. 3.4. Use of this growth condition might improve characteristics of semipolar r-plane UVC LEDs.

6.2.3 Adoption of p-type Graded AlGaN Layer

Since the ionization energy of Mg acceptor in AlN is too high [4, 73, 74], obtaining p-AlGaN with high AlN molar fraction is difficult [4,88,89]. This is one reason why current UV-LEDs usually use GaN as a p-type layer and/or a contact layer [24, 83, 84, 87, 95–118] [1], although GaN absorbs UV light emitted from AlGaN QWs, which results in reduction of LEE. Polarization

[1]The second reason is high work function of AlGaN [90].

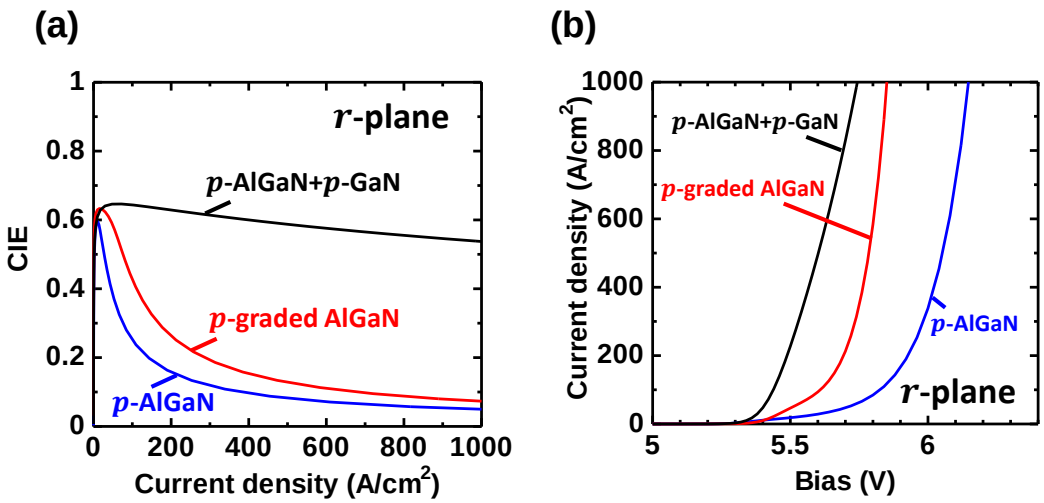

Figure 6.7: Calculation results of (a) CIE and (b) IV characteristics of r-plane AlGaN-based UVC LEDs which emit at ∼230 nm.

doping [145, 146] may overcome this trade-off. Electric field and electric charge are related by Poisson equation,

$$\frac{\mathrm{d}}{\mathrm{d}z'}(\varepsilon_{z'z'}E_{z'} + P_{\mathrm{s},z'} + P_{\mathrm{pz},z'}) = e(p + N_{\mathrm{D}}^{+} - n - N_{\mathrm{A}}^{-}), \tag{6.1}$$

where z' is the growth direction, $\varepsilon_{z'z'}$ is the z' component of permittivity, $E_{z'}$ is the z' component of electric field, $P_{\mathrm{s},z'}$ is the z' component of spontaneous polarization, $P_{\mathrm{pz},z'}$ is the z' component of piezoelectric polarization, e is the elementary charge, p is the hole density, N_{D}^{+} is the ionized donor density, n is the electron density, and N_{A}^{-} is the ionized acceptor density. The positional change in spontaneous and piezoelectric polarizations will be distributed between the electric charge (the right-hand side in Eq. (6.1)) and the positional change in $\varepsilon_{z'z'}E_{z'}$ (part of the left-hand side in Eq. (6.1)). According to self-consistent calculations by a commercial device simulator (SiLENSe), positional change in $\varepsilon_{z'z'}E_{z'}$ is small and electric charges are generated by positional changes in spontaneous and piezoelectric polarizations.

When AlN molar fraction is continuously reduced along [0001] axis, holes are generated. On semipolar planes, spontaneous and piezoelectric polarizations along the growth axis are smaller than those along the c-axis. However, r-plane has moderate electric polarizations and still high hole concentration can be achieved as shown in Fig. 6.6 [72]. Figure 6.7 shows calculation results of CIE and IV characteristics of r-plane AlGaN-based UVC LEDs emitting at ∼230 nm. Structures for simulations are identical to that in Fig. 2.9 (b)

except for the *p*-type layer. *p*-Type layers are set to 20-nm *p*-$Al_{0.88}Ga_{0.12}N$ + 100-nm *p*-GaN, 20-nm *p*-$Al_{0.88}Ga_{0.12}N$, or 20-nm *p*-graded AlGaN (AlN molar fraction: from 1 to 0.88), respectively. Although further optimization of structures including EBL is necessary, adoption of *p*-graded AlGaN will increase CIE compared with *p*-AlGaN [2], obtain better IV characteristics, and achieve both of better conductance of *p*-layer and high LEE.

[2]In the case of *c*-plane, CIE is decreased by the adoption of *p*-graded AlGaN compared with *p*-AlGaN. This reason is currently unknown because barrier heights of electron and hole between active layer and *p*-type are nearly the same. Effectiveness of the use of *p*-graded AlGaN might depend on the growth plane, and should be investigated in the future.

Appendix A

Material Parameters Used in This Study

Table A.1 shows material parameters used in the band calculation. Parameters of AlGaN are obtained by linear interpolartion of those of GaN and AlN except for some parameters. Bandgap at 0 K, Varshni parameters, spontaneous polarization of AlGaN are interpolated from those of AlN and GaN by quadratic function, using bowing parameters. Table A.2 shows bowing parameters used in the band calculation.

For the calculations by SiLENSe, material parameters in Tab. A.3 are also used. Effective masses of holes are calculated by the formula for small wavenumber (the upper side on TABLE I in [64]) using A parameters and Δ_1, Δ_2, and Δ_3 listed on Tab. A.1. This is because in the current version of SiLENSe (v.6.5) they are calculated by the formula for large wavenumber (the below side on TABLE I in [64]). Effective masses of holes of $Al_xGa_{1-x}N$ are calculated by

$$1/m^*_{\mathrm{h},i,\mathrm{Al}_x\mathrm{Ga}_{1-x}\mathrm{N}} = x/m^*_{\mathrm{h},i,\mathrm{AlN}} + (1-x)/m^*_{\mathrm{h},i,\mathrm{GaN}}, \tag{A.1}$$

where $i = 1, 2, 3$ and $i = 1$ means HH, $i = 2$ means LH in GaN (CH in AlN), and $i = 3$ means CH in GaN (LH in AlN). Ionization energy is defined as the energy difference between the top of heavy hole valence band and the vacuum level at 0 K in SiLENSe. Ionization energies of AlN and GaN (Υ_{AlN} and Υ_{GaN}) are determined so that $\Delta E_\mathrm{c} : \Delta E_\mathrm{v}$ of GaN and AlN equals to $7 : 3$, where ΔE_c and ΔE_v are the band offset of conduction band minimum and that of valence band maximum. The bowing parameter of ionization energy b_Υ is set to $0.3 b_{E_\mathrm{g}}$, where b_{E_g} is the bowing parameter of bandgap. This setting means that $\Delta E_\mathrm{c} : \Delta E_{\mathrm{v,HH}}$ of AlGaN is always $7 : 3$, where $\Delta E_{\mathrm{v,HH}}$ is the band offset of HH valence band maximum. Si ionization energy of AlGaN is known to increase drastically when AlN molar fraction x is changed from

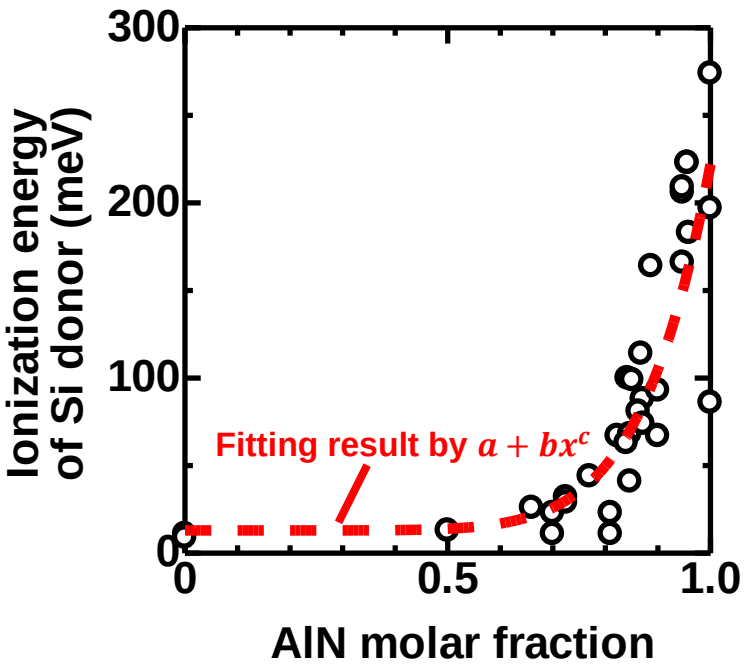

Figure A.1: Reported Si ionization energies of AlGaN [62,142–144] and fitting result by $a + bx^c$.

~0.8 to 1 [142–144]. Therefore, linear interpolartion and interpolation by quadratic function are not suitable for donor ionization energies of AlGaN. Fitting by $a + bx^c$ is adopted so that SiLENSe can calculate donor ionization energies of AlGaN easily. a is determined to be 13 meV so that donor ionization energy of GaN becomes 13 meV (default parameter of SiLENSe). Fitting results are b =209 meV, and c =7.79. As a result, donor ionization energy of AlN was set to 222 meV.

Table A.1: Material parameters used in the band calculations.

Parameters		AlN	GaN
Bandgap energy at 0 K (eV)	E_g	6.10 [21]	3.51 [21]
Varshni Parameters	α (meV/K)	2.63 [21]	0.914 [21]
	β (K)	2082 [21]	825 [21]
Valence-band splitting parameters (meV)	Δ_1	-211.5 [147]	12.3 [148]
	Δ_2	6.0 [147]	5.2 [148]
	Δ_3	6.5 [147]	5.9 [148]
Lattice constant at 300 K (nm)	a	0.3112 [125]	0.3189 [125]
	c	0.4982 [125]	0.5185 [125]
Elastic stiffness constants (GPa)	C_{11}	396 [125]	390 [125]
	C_{12}	137 [125]	145 [125]
	C_{13}	108 [125]	106 [125]
	C_{33}	373 [125]	398 [125]
	C_{44}	116 [125]	105 [125]
Electron effective masses (m_0)	$m_e^{\parallel}$	0.32 [21]	0.21 [21]
	$m_e^{\perp}$	0.30 [21]	0.20 [21]
Valence band effective mass parameters	A_1	-3.86 [21]	-7.21 [21]
($\hbar^2/(2m_0)$)	A_2	-0.25 [21]	-0.44 [21]
	A_3	3.58 [21]	6.68 [21]
	A_4	-1.32 [21]	-3.46 [21]
	A_5	-1.47 [21]	-3.40 [21]
	A_6	-1.64 [21]	-4.90 [21]
Deformation potentials (eV)	C_1	4.3 [147]	6.5 [148]
	C_2	11.5 [147]	11.2 [148]
	C_3	3.8 [147]	4.9 [148]
	C_4	-3.6 [147]	-5.0 [148]
	C_5	-2.8 [147]	-2.8 [148]
	C_6	-4.5 [147]	-3.1 [148]
	a_{cz}	-20.5 [125]	-8.6 [125]
	a_{ct}	-3.9 [125]	-6.8 [125]
Spontaneous polarization (C/m^2)	P^{sp}	-0.090 [125]	-0.034 [125]
Piezoelectric constants (C/m^2)	e_{15}	-0.48 [149]	-0.33 [150]
	e_{31}	-0.58 [149]	-0.33 [150]
	e_{33}	1.55 [149]	0.65 [150]
Relative permittivities	$\varepsilon_{\parallel}$	9.32 [151]	10.4 [152]
	$\varepsilon_{\perp}$	7.76 [151]	9.5 [152]

Table A.2: Bowing parameters for AlGaN used in this study.

Bowing parameters for AlGaN	
Spontaneous polarization (C/m^2)	-0.021 [125]
Bandgap (eV)	0.8 [21]
Varshni parameter α (meV/K)	2.15 [21]
Varshni parameter β (K)	1561 [21]

Table A.3: Material parameters used in the calculations by SiLENSe.

Parameters		AlN	GaN
Acceptor ionization energy (meV)	ΔE_{A}	630 [4]	170
Electron g-factor	g_{e}	2	2
Hole g-factor	g_{h}	2	4
Hole effective masses	$m^*_{\mathrm{h},1,\parallel\mathrm{a}}$	0.64	0.26
	$m^*_{\mathrm{h},1,\parallel\mathrm{c}}$	3.57	1.89
	$m^*_{\mathrm{h},2,\parallel\mathrm{a}}$	3.96	0.35
	$m^*_{\mathrm{h},2,\parallel\mathrm{c}}$	0.26	0.39
	$m^*_{\mathrm{h},3,\parallel\mathrm{a}}$	0.64	0.67
	$m^*_{\mathrm{h},3,\parallel\mathrm{c}}$	3.49	0.19
Ionization energy (eV)	Υ	6.306	5.323

References

[1] USA EPA UV Disinfection Guidance Manual. EPA 815-D-03-007 (2003)

[2] ISO 21348 (2007)

[3] B. J. Lin, *J. Vac. Sci. Technol.* **12**, 1317

[4] Y. Taniyasu, M. Kasu, and T. Makimoto, *Nature* **441**, 325 (2006).

[5] https://www.unicef.org/media/129381/file/State

[6] https://sdgs.un.org/2030agenda

[7] D. Welch, M. Buonanno, V. Grilj, I. Shuryak, C. Crickmore, A. W. Bigelow, G. Randers-Pehrson, G. W. Johnson, and D. J. Brenner, *Sci. Rep.* **8**, 2752 (2018).

[8] K. Narita, K. Asano, K. Naito, H. Ohashi, M. Sasaki, Y. Morimoto, T. Igarashi, and A. Nakane, *J. Hosp. Infec.* **105**, 459 (2020).

[9] W. Taylor, E. Camilleri, D. L. Craft, G. Korza, M. R. Granados, J. Peterson, R. Szczpaniak, S. K. Weller, R. Moeller, T. Douki, W. W. K. Mok, and P. Setlow, *Appl. Environ. Microbiol.* **86**, e03039 (2020).

[10] M. Buonanno, D. Welch, I. Shuryak, and D. J. Brenner, *Sci. Rep.* **10**, 10285 (2020).

[11] H. Kitagawa, T. Nomura, T. Nazmul, K. Omori, N. Shigemoto, T. Sakaguchi, and H. Ohge, *Am. J. Infect. Control* **49**, 299 (2021).

[12] M. Buonanno, B. Ponnaiya, D. Welch, M. Stanislauskas, G. Randers-Pehrson, L. Smilenov, F. D. Lowy, D. M. Owens, and D. J. Brenner, *Radiat. Res.* **187**, 493 (2017).

[13] N. Yamano, M. Kunisada, S. Kaidzu, K. Sugihara, A. Nishiaki-Sawada, H. Ohashi, A. Yoshioka, T. Igarashi, A. Ohira, M. Tanito, and C. Nishigori, *Photochem. Photobiol.* **96**, 853 (2020).

[14] T. Fukui, T. Niikura, T. Oda, Y. Kumabe, H. Ohashi, M. Sasaki, T. Igarashi, M. Kunisada, N. Yamano, K. Oe, T. Matsumoto, T. Matsushita, S. Hayashi, C. Nishigori, and R. Kuroda, *PLoS ONE* **15**, e0235948 (2020).

[15] T. Fukui, T. Niikura, T. Oda, Y. Kumabe, A. Nishiaki, R. Kaigome, H. Ohashi, M. Sasaki, T. Igarashi, K. Oe, M. R. Hamblin, and R. Kuroda, *Photochem. Photobiol.*, php.13620 (2022).

[16] https://clean.ushio.com/jp/products/care222_i_series/

[17] H. Amano, N. Sawaki, I. Akasaki, and Y. Toyoda, *Appl. Phys. Lett.* **48**, 353 (1986).

[18] S. Nakamura, *Jpn. J. Appl. Phys.* **30**, L1705 (1991).

[19] H. Amano, M. Kito, K. Hiramatsu, and I. Akasaki, *Jpn. J. Appl. Phys.* **28**, L2112 (1989).

[20] S. Nakamura, T. Mukai, and M. Senoh, *Jpn. J. Appl. Phys.* **31**, L139 (1992).

[21] I. Vurgaftman and J. R. Meyer, *Nitride Semiconductor Devices: Principles and Simulations*, Chap. 2. Wiley-VCH, New York, (2007)

[22] M. Kneissl, T.-Y. Seong, J. Han, and H. Amano, *Nat. Photonics* **13**, 233 (2019).

[23] T. Takano, T. Mino, J. Sakai, N. Noguchi, K. Tsubaki, and H. Hirayama, *Appl. Phys. Express* **10**, 031002 (2017).

[24] Y. Matsukura, T. Inazu, C. Pernot, N. Shibata, M. Kushimoto, M. Deki, Y. Honda, and H. Amano, *Appl. Phys. Express* **14**, 084004 (2021).

[25] Y. Narukawa, M. Ichikawa, D. Sanga, M. Sano, and T. Mukai, *J. Phys. D: Appl. Phys.* **43**, 354002 (2010).

[26] R. G. Banal, M. Funato, and Y. Kawakami, *Appl. Phys. Lett.* **99**, 011902 (2011).

[27] Y. Nagasawa and A. Hirano, *Appl. Sci.* **8**, 1264 (2018).

[28] K. Ueno, A. Kobayashi, J. Ohta, H. Fujioka, H. Amanai, S. Nagao, and H. Horie, *Phys. Status Solidi RRL* **3**, 58 (2009).

[29] K. Balakrishnan, V. Adivarahan, Q. Fareed, M. Lachab, B. Zhang, and A. Khan, *Jpn. J. Appl. Phys.* **49**, 040206 (2010).

[30] K. Balakrishnan, M. Lachab, H. C. Chen, D. Blom, V. Adivarahan, I. Ahmad, Q. Fareed, and M. A. Khan, *Phys. Status Solidi A* **208**, 2724 (2011).

[31] J. Stellmach, F. Mehnke, M. Frentrup, C. Reich, J. Schlegel, M. Pristovsek, T. Wernicke, and M. Kneissl, *J. Cryst. Growth* **367**, 42 (2013).

[32] A. Mogilatenko, H. Kirmse, J. Stellmach, M. Frentrup, F. Mehnke, T. Wernicke, M. Kneissl, and M. Weyers, *J. Cryst. Growth* **400**, 54 (2014).

[33] M. Feneberg, M. Winkler, J. Klamser, J. Stellmach, M. Frentrup, S. Ploch, F. Mehnke, T. Wernicke, M. Kneissl, and R. Goldhahn, *Appl. Phys. Lett.* **106**, 182102 (2015).

[34] D. V. Dinh, M. Conroy, V. Zubialevich, N. Petkov, J. Holmes, and P. Parbrook, *J. Cryst. Growth* **414**, 94 (2015).

[35] D. V. Dinh, S. Alam, and P. Parbrook, *J. Cryst. Growth* **435**, 12 (2016).

[36] D. V. Dinh, P. Pampili, and P. J. Parbrook, *J. Cryst. Growth* **451**, 181 (2016).

[37] Y. Wang, X. Zhang, H. Luan, H. Yang, S. Wang, Q. Dai, Z. Wu, and Y. Cui, *Mater. Sci. Semicond. Process.* **42**, 344 (2016).

[38] Q. Dai, X. Zhang, J. Zhao, H. Luan, Z. Liang, and Y. Cui, *Mater. Sci. Semicond. Process.* **58**, 30 (2017).

[39] Q. Dai, X. Zhang, Z. Wu, G. Yang, Z. Liang, J. Zhao, and Y. Cui, *Mater. Lett.* **209**, 472 (2017).

[40] M. Jo, I. Oshima, T. Matsumoto, N. Maeda, N. Kamata, and H. Hirayama, *Phys. Status Solidi C* **14**, 1600248 (2017).

[41] M. Jo and H. Hirayama, *Phys. Status Solidi B* **255**, 1700418 (2018).

[42] M. Jo, N. Morishita, N. Okada, Y. Itokazu, N. Kamata, K. Tadatomo, and H. Hirayama, *AIP Advances* **8**, 105312 (2018).

[43] M. Jo, Y. Itokazu, S. Kuwaba, and H. Hirayama, *J. Cryst. Growth* **507**, 307 (2019).

[44] M. Jo, Y. Itokazu, S. Kuwaba, and H. Hirayama, *Jpn. J. Appl. Phys.* **58**, SC1031 (2019).

[45] D. V. Dinh, N. Hu, Y. Honda, H. Amano, and M. Pristovsek, *Sci. Rep.* **9**, 15802 (2019).

[46] G. Yang, X. Zhang, Z. Wu, J. Zhao, A. Nasir, S. Chen, A. Fan, and Y. Cui, *Superlattices Microstruct.* **125**, 338 (2019).

[47] H. M. Foronda, S. Graupeter, F. Mehnke, J. Enslin, T. Wernicke, and M. Kneissl, *Jpn. J. Appl. Phys.* **58**, SC1026 (2019).

[48] H. M. Foronda, D. A. Hunter, M. Pietsch, L. Sulmoni, A. Muhin, S. Graupeter, N. Susilo, M. Schilling, J. Enslin, K. Irmscher, R. W. Martin, T. Wernicke, and M. Kneissl, *Appl. Phys. Lett.* **117**, 221101 (2020).

[49] D. V. Dinh, N. Hu, Y. Honda, H. Amano, and M. Pristovsek, *J. Mater. Chem. C* **8**, 8668 (2020).

[50] Q. Feng, Y. Ai, Z. Liu, Z. Yu, K. Yang, B. Dong, B. Guo, and Y. Zhang, *Superlattices Microstruct.* **141**, 106493 (2020).

[51] L. Spasevski, G. Kusch, P. Pampili, V. Z. Zubialevich, D. V. Dinh, J. Bruckbauer, P. R. Edwards, P. J. Parbrook, and R. W. Martin, *J. Phys. D: Appl. Phys.* **54**, 035302 (2021).

[52] M. Jo, Y. Itokazu, S. Kuwaba, and H. Hirayama, *20th International Workshop on Junction Technology*, 1 (2021).

[53] Q. Dai, X. Zhang, and Z. Wu, *Mater. Lett.* **324**, 132675 (2022).

[54] X. Luo, X. Zhang, B. Chen, Y. Shen, Y. Tian, A. Fan, S. Chen, Y. Qian, Z. Zhuang, and G. Hu, *Mater. Sci. Semicond. Process* **144**, 106612 (2022).

[55] X.-Q. Shen, K. Kojima, and H. Okumura, *Appl. Phys. Express* **13**, 035502 (2020).

[56] L. Chen, W. Lin, H. Chen, H. Xu, C. Guo, Z. Liu, J. Yan, J. Sun, H. Liu, J. Wu, W. Guo, J. Kang, and J. Ye, *Cryst. Growth Des.* **21**, 2911 (2021).

[57] K. Xing, X. Cheng, L. Wang, S. Chen, Y. Zhang, and H. Liang, *J. Cryst. Growth* **570**, 126207 (2021).

[58] S. Ichikawa, Y. Iwata, M. Funato, S. Nagata, and Y. Kawakami, *Appl. Phys. Lett.* **104**, 252102 (2014).

[59] S. Ichikawa, Ph.D. thesis, Kyoto University (2017)

[60] S. Ichikawa, M. Funato, and Y. Kawakami, *J. Cryst. Growth* **522**, 68 (2019).

[61] T. Wunderer, Z. Yang, M. Feneberg, M. Batres, M. Teepe, and N. Johnson, *Appl. Phys. Lett.* **111**, 111101 (2017).

[62] Y. Taniyasu, M. Kasu, and N. Kobayashi, *Appl. Phys. Lett.* **81**, 1255 (2002).

[63] Y. Taniyasu, M. Kasu, and T. Makimoto, *Appl. Phys. Lett.* **89**, 182112 (2006).

[64] S. L. Chuang and C. S. Chang, *Phys. Rev. B* **54**, 2491 (1996).

[65] S. L. Chuang and C. S. Chang, *Semicond. Sci. Technol.* **12**, 252 (1997).

[66] S. Ichikawa, M. Funato, and Y. Kawakami, *Semicond. Sci. Technol.* **36**, 085016 (2021).

[67] J. Matthews, *J. Cryst. Growth* **27**, 118 (1974).

[68] R. People and J. C. Bean, *Appl. Phys. Lett.* **47**, 322 (1985).

[69] J. Nishinaka, M. Funato, and Y. Kawakami, *J. Appl. Phys.* **112**, 033513 (2012).

[70] R. G. Banal, M. Funato, and Y. Kawakami, *Phys. Rev. B* **79**, 121308 (2009).

[71] https://str-soft.com/devices/silense/

[72] K. Kamiya, R. Akaike, M. Funato, and Y. Kawakami, *83th Japan Society of Applied Physics Fall Meeting*, 22p-C200-1, Tohoku Univ., (Sep. 2022),

[73] Á. Szabó, N. T. Son, E. Janzén, and A. Gali, *Appl. Phys. Lett.* **96**, 192110 (2010).

[74] J. L. Lyons, A. Janotti, and C. G. Van de Walle, *Phys. Rev. Lett.* **108**, 156403 (2012).

[75] M. H. Breckenridge, P. Bagheri, Q. Guo, B. Sarkar, D. Khachariya, S. Pavlidis, J. Tweedie, R. Kirste, S. Mita, P. Reddy, R. Collazo, and Z. Sitar, *Appl. Phys. Lett.* **118**, 112104 (2021).

[76] H. Ahmad, Z. Engel, C. M. Matthews, S. Lee, and W. A. Doolittle, *J. Appl. Phys.* **131**, 175701 (2022).

[77] L. Gordon, J. L. Lyons, A. Janotti, and C. G. Van de Walle, *Phys. Rev. B* **89**, 085204 (2014).

[78] B. E. Gaddy, Z. Bryan, I. Bryan, J. Xie, R. Dalmau, B. Moody, Y. Kumagai, T. Nagashima, Y. Kubota, T. Kinoshita, A. Koukitu, R. Kirste, Z. Sitar, R. Collazo, and D. L. Irving, *Appl. Phys. Lett.* **104**, 202106 (2014).

[79] R. Ishii, A. Yoshikawa, H. Kobayashi, M. Funato, and Y. Kawakami, *Jpn. J. Appl. Phys.* **60**, 080901 (2021).

[80] A. Rice, R. Collazo, J. Tweedie, R. Dalmau, S. Mita, J. Xie, and Z. Sitar, *J. Appl. Phys.* **108**, 043510 (2010).

[81] A. Dadgar, A. Krost, J. Christen, B. Bastek, F. Bertram, A. Krtschil, T. Hempel, J. Bläsing, U. Haboeck, and A. Hoffmann, *J. Cryst. Growth* **297**, 306 (2006).

[82] J. Jasinski, Z. Liliental-Weber, Q. S. Paduano, and D. W. Weyburne, *Appl. Phys. Lett.* **83**, 2811 (2003).

[83] W. Sun, M. Shatalov, J. Deng, X. Hu, J. Yang, A. Lunev, Y. Bilenko, M. Shur, and R. Gaska, *Appl. Phys. Lett.* **96**, 061102 (2010).

[84] A. Fujioka, K. Asada, H. Yamada, T. Ohtsuka, T. Ogawa, T. Kosugi, D. Kishikawa, and T. Mukai, *Semicond. Sci. Technol.* **29**, 084005 (2014).

[85] M. Jo, N. Maeda, and H. Hirayama, *Appl. Phys. Express* **9**, 012102 (2016).

[86] M. Kaneda, C. Pernot, Y. Nagasawa, A. Hirano, M. Ippommatsu, Y. Honda, H. Amano, and I. Akasaki, *Jpn. J. Appl. Phys.* **56**, 061002 (2017).

[87] S. Inoue, N. Tamari, and M. Taniguchi, *Appl. Phys. Lett.* **110**, 141106 (2017).

[88] M. L. Nakarmi, K. H. Kim, M. Khizar, Z. Y. Fan, J. Y. Lin, and H. X. Jiang, *Appl. Phys. Lett.* **86**, 092108 (2005).

[89] K. Nagamatsu, K. Takeda, M. Iwaya, S. Kamiyama, H. Amano, and I. Akasaki, *Phys. Status Solidi C* **6** (2009).

[90] C. G. Van de Walle and J. Neugebauer, *Nature* **423**, 626 (2003).

[91] M. Shatalov, W. Sun, A. Lunev, X. Hu, A. Dobrinsky, Y. Bilenko, J. Yang, M. Shur, R. Gaska, C. Moe, G. Garrett, and M. Wraback, *Appl. Phys. Express* **5**, 082101 (2012).

[92] M. A. Khan, T. Matsumoto, N. Maeda, N. Kamata, and H. Hirayama, *Jpn. J. Appl. Phys.* **58**, SAAF01 (2019).

[93] M. A. Khan, R. Takeda, Y. Yamada, N. Maeda, M. Jo, and H. Hirayama, *Opt. Lett.* **45**, 495 (2020).

[94] M. A. Khan, Y. Itokazu, N. Maeda, M. Jo, Y. Yamada, and H. Hirayama, *ACS Appl. Electron. Mater.* **2**, 1892 (2020).

[95] H. Hirayama, S. Fujikawa, N. Noguchi, J. Norimatsu, T. Takano, K. Tsubaki, and N. Kamata, *Phys. Status Solidi A* **206**, 1176 (2009).

[96] A. Fujioka, T. Misaki, T. Murayama, Y. Narukawa, and T. Mukai, *Appl. Phys. Express* **3**, 041001 (2010).

[97] C. Pernot, M. Kim, S. Fukahori, T. Inazu, T. Fujita, Y. Nagasawa, A. Hirano, M. Ippommatsu, M. Iwaya, S. Kamiyama, I. Akasaki, and H. Amano, *Appl. Phys. Express* **3**, 061004 (2010).

[98] S. Hwang, D. Morgan, A. Kesler, M. Lachab, B. Zhang, A. Heidari, H. Nazir, I. Ahmad, J. Dion, Q. Fareed, V. Adivarahan, M. Islam, and A. Khan, *Appl. Phys. Express* **4**, 032102 (2011).

[99] C. Pernot, S. Fukahori, T. Inazu, T. Fujita, M. Kim, Y. Nagasawa, A. Hirano, M. Ippommatsu, M. Iwaya, S. Kamiyama, I. Akasaki, and H. Amano, *Phys. Status Solidi A* **208**, 1594 (2011).

[100] M. Kim, T. Fujita, S. Fukahori, T. Inazu, C. Pernot, Y. Nagasawa, A. Hirano, M. Ippommatsu, M. Iwaya, T. Takeuchi, S. Kamiyama, M. Yamaguchi, Y. Honda, H. Amano, and I. Akasaki, *Appl. Phys. Express* **4**, 092102 (2011).

[101] T. Mino, H. Hirayama, T. Takano, N. Noguchi, and K. Tsubaki, *Phys. Status Solidi C* **9**, 749 (2012).

[102] T. Kinoshita, K. Hironaka, T. Obata, T. Nagashima, R. Dalmau, R. Schlesser, B. Moody, J. Xie, S.-i. Inoue, Y. Kumagai, A. Koukitu, and Z. Sitar, *Appl. Phys. Express* **5**, 122101 (2012).

[103] J. R. Grandusky, J. Chen, S. R. Gibb, M. C. Mendrick, C. G. Moe, L. Rodak, G. A. Garrett, M. Wraback, and L. J. Schowalter, *Appl. Phys. Express* **6**, 032101 (2013).

[104] P. Dong, J. Yan, J. Wang, Y. Zhang, C. Geng, T. Wei, P. Cong, Y. Zhang, J. Zeng, Y. Tian, L. Sun, Q. Yan, J. Li, S. Fan, and Z. Qin, *Appl. Phys. Lett.* **102**, 241113 (2013).

[105] F. Asif, H.-C. Chen, A. Coleman, I. Ahmad, B. Zhang, J. Dion, A. Heidari, V. Adivarahan, and A. Khan, *Phys. Status Solidi C* **11**, 798 (2014).

[106] K. Yamada, Y. Furusawa, S. Nagai, A. Hirano, M. Ippommatsu, K. Aosaki, N. Morishima, H. Amano, and I. Akasaki, *Appl. Phys. Express* **8**, 012101 (2015).

[107] S.-i. Inoue, T. Naoki, T. Kinoshita, T. Obata, and H. Yanagi, *Appl. Phys. Lett.* **106**, 131104 (2015).

[108] G.-D. Hao, M. Taniguchi, N. Tamari, and S.-i. Inoue, *J. Phys. D: Appl. Phys.* **49**, 235101 (2016).

[109] D. Lee, J. W. Lee, J. Jang, I.-S. Shin, L. Jin, J. H. Park, J. Kim, J. Lee, H.-S. Noh, Y.-I. Kim, Y. Park, G.-D. Lee, Y. Park, J. K. Kim, and E. Yoon, *Appl. Phys. Lett.* **110**, 191103 (2017).

[110] N. Susilo, S. Hagedorn, D. Jaeger, H. Miyake, U. Zeimer, C. Reich, B. Neuschulz, L. Sulmoni, M. Guttmann, F. Mehnke, C. Kuhn, T. Wernicke, M. Weyers, and M. Kneissl, *Appl. Phys. Lett.* **112**, 041110 (2018).

[111] K. Nagamatsu, X. Liu, K. Uesugi, and H. Miyake, *Jpn. J. Appl. Phys.* **58**, SCCC07 (2019).

[112] A. Yoshikawa, R. Hasegawa, T. Morishita, K. Nagase, S. Yamada, J. Grandusky, J. Mann, A. Miller, and L. J. Schowalter, *Appl. Phys. Express* **13**, 022001 (2020).

[113] N. Lobo-Ploch, F. Mehnke, L. Sulmoni, H. K. Cho, M. Guttmann, J. Glaab, K. Hilbrich, T. Wernicke, S. Einfeldt, and M. Kneissl, *Appl. Phys. Lett.* **117**, 111102 (2020).

[114] J. Glaab, J. Ruschel, N. Lobo Ploch, H. K. Cho, F. Mehnke, L. Sulmoni, M. Guttmann, T. Wernicke, M. Weyers, S. Einfeldt, and M. Kneissl, *J. Appl. Phys.* **131**, 014501 (2022).

[115] S. Walde, C.-Y. Huang, C.-L. Tsai, W.-H. Hsieh, Y.-K. Fu, S. Hagedorn, H.-W. Yen, T.-C. Lu, M. Weyers, and C.-Y. Huang, *Acta Mater.* **226**, 117625 (2022).

[116] Z. Qian, S. Zhu, X. Shan, P. Yin, Z. Yuan, P. Qiu, Z. Wang, X. Cui, and P. Tian, *J. Phys. D: Appl. Phys.* **55**, 195104 (2022).

[117] M. Jo, Y. Itokazu, and H. Hirayama, *Appl. Phys. Lett.* **120**, 211105 (2022).

[118] K. Uesugi, S. Kuboya, K. Shojiki, S. Xiao, T. Nakamura, M. Kubo, and H. Miyake, *Appl. Phys. Express* **15**, 055501 (2022).

[119] F. Mehnke, T. Wernicke, H. Pingel, C. Kuhn, C. Reich, V. Kueller, A. Knauer, M. Lapeyrade, M. Weyers, and M. Kneissl, *Appl. Phys. Lett.* **103**, 212109 (2013).

[120] J. Grandusky, J. Smart, M. Mendrick, L. Schowalter, K. Chen, and E. Schubert, *J. Cryst. Growth* **311**, 2864 (2009).

[121] C. He, Z. Qin, F. Xu, L. Zhang, J. Wang, M. Hou, S. Zhang, X. Wang, W. Ge, and B. Shen, *Appl. Phys. Express* **9**, 051001 (2016).

[122] C. He, Z. Qin, F. Xu, L. Zhang, J. Wang, M. Hou, S. Zhang, X. Wang, W. Ge, and B. Shen, *Sci Rep* **6**, 25124 (2016).

[123] J. Nishinaka, Ph.D. thesis, Kyoto University (2014)

[124] M. Frentrup, N. Hatui, T. Wernicke, J. Stellmach, A. Bhattacharya, and M. Kneissl, *J. Appl. Phys.* **114**, 213509 (2013).

[125] I. Vurgaftman and J. R. Meyer, *J. Appl. Phys.* **94**, 3675 (2003).

[126] A. E. Romanov, E. C. Young, F. Wu, A. Tyagi, C. S. Gallinat, S. Nakamura, S. P. DenBaars, and J. S. Speck, *J. Appl. Phys.* **109**, 103522 (2011).

[127] E. C. Young, F. Wu, A. E. Romanov, A. Tyagi, C. S. Gallinat, S. P. DenBaars, S. Nakamura, and J. S. Speck, *Appl. Phys. Express* **3**, 011004 (2010).

[128] T. Kohno, Y. Sudo, M. Yamauchi, K. Mitsui, H. Kudo, H. Okagawa, and Y. Yamada, *Jpn. J. Appl. Phys.* **51**, 072102 (2012).

[129] C. Frankerl, M. P. Hoffmann, F. Nippert, H. Wang, C. Brandl, N. Tillner, H.-J. Lugauer, R. Zeisel, A. Hoffmann, and M. J. Davies, *J. Appl. Phys.* **126**, 075703 (2019).

[130] R. Ishii, A. Yoshikawa, K. Nagase, M. Funato, and Y. Kawakami, *Appl. Phys. Express* **13**, 102005 (2020).

[131] C. Gourdon and P. Lavallard, *Phys. Status Solidi B* **153**, 641 (1989).

[132] S. Watanabe, N. Yamada, M. Nagashima, Y. Ueki, C. Sasaki, Y. Yamada, T. Taguchi, K. Tadatomo, H. Okagawa, and H. Kudo, *Appl. Phys. Lett.* **83**, 4906 (2003).

[133] Y. Iwata, R. G. Banal, S. Ichikawa, M. Funato, and Y. Kawakami, *J. Appl. Phys.* **117**, 075701 (2015).

[134] A. Kaneta, M. Funato, and Y. Kawakami, *Phys. Rev. B* **78**, 125317 (2008).

[135] H. Murotani and Y. Yamada, *Jpn. J. Appl. Phys.* **58**, 011003 (2019).

[136] S. Ichikawa, M. Funato, and Y. Kawakami, *Phys. Rev. Applied* **10**, 064027 (2018).

[137] M. Guttmann, F. Mehnke, B. Belde, F. Wolf, C. Reich, L. Sulmoni, T. Wernicke, and M. Kneissl, *Jpn. J. Appl. Phys.* **58**, SCCB20 (2019).

[138] D.-F. Wang, F. Shiwei, C. Lu, A. Motayed, M. Jah, S. N. Mohammad, K. A. Jones, and L. Salamanca-Riba, *J. Appl. Phys.* **89**, 6214 (2001).

[139] K. Kataoka, Ph.D. thesis, Kyoto University (2017)

[140] R. France, T. Xu, P. Chen, R. Chandrasekaran, and T. D. Moustakas, *Appl. Phys. Lett.* **90**, 062115 (2007).

[141] K. Mori, K. Takeda, T. Kusafuka, M. Iwaya, T. Takeuchi, S. Kamiyama, I. Akasaki, and H. Amano, *Jpn. J. Appl. Phys.* **55**, 05FL03 (2016).

[142] M. L. Nakarmi, K. H. Kim, K. Zhu, J. Y. Lin, and H. X. Jiang, *Appl. Phys. Lett.* **85**, 3769 (2004).

[143] R. Collazo, S. Mita, J. Xie, A. Rice, J. Tweedie, R. Dalmau, and Z. Sitar, *Phys. Status Solidi C* **8**, 2031 (2011).

[144] F. Mehnke, X. T. Trinh, H. Pingel, T. Wernicke, E. Janzén, N. T. Son, and M. Kneissl, *J. Appl. Phys.* **120**, 145702 (2016).

[145] D. Jena, S. Heikman, D. Green, D. Buttari, R. Coffie, H. Xing, S. Keller, S. DenBaars, J. S. Speck, U. K. Mishra, and I. Smorchkova, *Appl. Phys. Lett.* **81**, 4395 (2002).

[146] J. Simon, V. Protasenko, C. Lian, H. Xing, and D. Jena, *Science* **327**, 60 (2010).

[147] R. Ishii, A. Kaneta, M. Funato, and Y. Kawakami, *Phys. Rev. B* **87**, 235201 (2013).

[148] R. Ishii, A. Kaneta, M. Funato, Y. Kawakami, and A. A. Yamaguchi, *Phys. Rev. B* **81**, 155202 (2010).

[149] K. Tsubouchi and N. Mikoshiba, *IEEE Trans. Son. Ultrason.* **32**, 634 (1985).

[150] O. Ambacher, *J. Phys. D: Appl. Phys.* **31**, 2653 (1998).

[151] W. J. Moore, J. A. Freitas, R. T. Holm, O. Kovalenkov, and V. Dmitriev, *Appl. Phys. Lett.* **86**, 141912 (2005).

[152] A. S. Barker and M. Ilegems, *Phys. Rev. B* **7**, 743 (1973).

List of Publications

A. Journal Papers

1. R. Akaike, S. Ichikawa, M. Funato, and Y. Kawakami,
"$Al_xGa_{1-x}N$-based semipolar deep ultraviolet light-emitting diodes,"
Appl. Phys. Express **11**, 061001 (2018).

2. R. Akaike, S. Ichikawa, M. Funato, and Y. Kawakami,
"Lattice relaxation in semipolar $Al_xGa_{1-x}N$ grown on $(1\bar{1}02)$ AlN substrates,"
Appl. Phys. Express **13**, 061008 (2020).

3. R. Akaike, M. Funato, and Y. Kawakami,
"Improved internal quantum efficiencies of far-UVC AlGaN/AlN quantum wells by the use of semipolar r-plane,"
submitted

4. R. Akaike, M. Funato, and Y. Kawakami,
"Semipolar $(1\bar{1}02)$ r-plane AlGaN films with reduced pit density grown under low-pressure conditions,"
in preparation

B. International Conferences

1. R. Akaike, M. Funato, and Y. Kawakami,
"Efficient far-UVC emissions from semipolar r-plane AlGaN/AlN QWs,"
The 10$^{\text{th}}$ *Asia-Pacific Workshop on Widegap Semiconductors*, Taouyuan, Taiwan, OTC-07, (Nov. 2022), oral.

C. Domestic Conferences

1. R. Akaike, M. Funato, and Y. Kawakami,
"First demonstration and characterization of semipolar deep ultraviolet LEDs on r-AlN,"
39th Electronic Materials Symposium, P2-17, Online, (Oct. 2020), short presentation and poster.

2. R. Akaike, M. Funato, and Y. Kawakami,
"Efficient emissions from semipolar AlGaN quantum wells below 250 nm,"
83th Japan Society of Applied Physics Fall Meeting, 20p-B202-6, Tohoku Univ., (Sep. 2022), oral.

3. K. Kamiya, R. Akaike, M. Funato, and Y. Kawakami,
"Consideration of polarization-induced p-type conduction layer on semipolar graded AlGaN layers,"
83th Japan Society of Applied Physics Fall Meeting, 22p-C200-1, Tohoku Univ., (Sep. 2022), oral.

4. R. Akaike, M. Funato, and Y. Kawakami,
"Analysis with time resolved PL of semipolar r-plane AlGaN/AlN emitting at far-UVC region,"
14th Nanostructure Epitaxial Growth Meeting, Fr-P28, Ube-shi Cultural Hall, (Nov. 2022), short presentation and poster.

5. R. Akaike, M. Funato, and Y. Kawakami,
"MOVPE growth of semipolar r-plane AlGaN films with smooth surface under low-pressure conditions,"
4th ISYSE Meeting, Tu-6, Urbal Hotel Minami Kusatsu., (Nov. 2022), oral.

6. R. Akaike, M. Funato, and Y. Kawakami,
"Low-pressure MOVPE growth of semipolar r-plane AlGaN films with low pit density,"
70th Japan Society of Applied Physics Spring Meeting, 18p-B401-7, Sophia Univ., (Mar. 2023), oral.

D. Research Grants

1. Grant-in-Aid for JSPS Research Fellow (DC2)

2. WISE program, MEXT